REFLECT DELIVERABLE D1.1

Fluid Data for geothermal sites (type A)


Photo: Alper Baba, Izmir Institute of Technology

Summary:

In this interim report, the studies on geothermal fluids carried out in Turkey, France and Iceland geothermal fields are explained.

Authors:

Alper Baba, İzmir Institute of Technology (IZTECH), Geological Engineer
Mustafa M. Demir, İzmir Institute of Technology (IZTECH), Chemist
Serhat Tonkul, İzmir Institute of Technology (IZTECH), PhD student
Laurent André, French Geological Survey (BRGM), Geochemist
Bernard Sanjuan, French Geological Survey (BRGM), Senior expert in geochemistry
Deirdre Clark, Iceland GeoSurvey (ISOR), Geochemist
Finnbogi Óskarsson, Iceland GeoSurvey (ISOR), Geochemist

This project has received funding from the European Union's Horizon 2020 research and innovation programme under grant agreement nº 850626.

Title:	Fluid Data for geothermal sites (type A)
Lead beneficiary:	IZTECH
Other beneficiaries:	ISOR, BRGM
Due date:	30 July 2021
Nature:	Public
Diffusion:	All project partners, EC, general public
Status:	Final
Document code:	REFLECT_D1.1
DOI:	http://doi.org/10.48440/gfz.4.8.2021.003
License information:	CC-BY-4.0
Recommended citation:	Baba, A., Demir, M.M., Tonkul, S., André, L., Sanjuan, B., Clark, D., Óskarsson, F., *The H2020 REFLECT project: Deliverable 1.1 - Fluid Data for geothermal sites (type A),* GFZ German Research Centre for Geosciences, http://doi.org/10.48440/gfz.4.8.2021.003
ORCID:	Alper Baba: 0000-0001-5307-3156 Serhat Tonkul: 0000-0002-8572-1565 Mustafa Muammer Demir: 0000-0003-1309-3990 Laurent Andre: 0000-0002-8844-1585 Bernard Sanjuan: 0000-0001-7004-2001 Deirdre Clark: 0000-0002-1278-6229 Finnbogi Óskarsson: 0000-0003-3521-7448

Revision history	Author	Delivery date	Summary of changes and comments
Version 01	Deirdre Clark	30.06.2021	Submission of Chapter 4 (Iceland)
Version 02	Serhat Tonkul	26.07.2021	Corrections for report
Final version	Alper Baba	28.07.2021	Submission of WP1

Approval status			
	Name	Function	Date
Deliverable responsible	Alper Baba	Task leader Task 1.1	29.07.2021
WP leader			
Reviewer	Laurent André	Task member Task 1.1	28.07.2021
Reviewer	Deirdre Clark	Task member Task 1.1	28.07.2021
Project Coordinator	Katrin Kieling	Project manager	30.07.2021

This document reflects only the author's view and the European Commission is not responsible for any use that may be made of the information it contains.

TABLE OF CONTENTS

1 EXECUTIVE SUMMARY

Although geothermal resources are widespread throughout the world, they are generally found in geothermal environments where tectonism and volcanism are active such as Turkey and Iceland. In this project three location (Turkey, France and Iceland) of high-geothermal field have been studied.

The first part of this report shows the results for the Germencik Geothermal Field (GGF), which is located in the western part of Turkey. In this field, there are a total of 25 geothermal wells (11 production wells, 9 reinjection wells and, 5 observation wells) with depths varying between 1400 and 3000 m. The GGF has a binary cycle geothermal power plant. The most important problem in the GGF is sulfide-type scale in the surface equipment system. This study list the results from analysis of physical and chemical properties of the fluid. It also includes the mineral analysis from rock samples of some of the wells of the geothermal field. Those results are then further studied for the temperature of the GGF using geothermometer approaches. Finally, mineral precipitation is investigated with a focus on stinite scaling. It is shown that the recommended reinjection temperature to prevent stibnite scaling would be 95°C.

The second part of the report focusses on the Bouillante geothermal plant (French West Indies), which exploits about 650 tons/h of hot fluid (Tres. close to 260°C) from two deep deviated wells BO-5 and BO-6 (about 1000 m deep) and produces about 20% of steam. Since 2005, it is constituted of two production units (Fig. 34), representing a total capacity of 15 MWe. Its present annual production is close to 110 GWh (about 5-6% of the island's electricity needs). For the moment and since 2015, the water reinjection is partial, and the majority of the produced fluid is discharged in the sea, after mixing and cooling with seawater and without important environmental impact. The water sample directly collected from the BO-6 wellhead in January 2021, which has been analysed in the BRGM laboratories during this study, indicates that the chemical composition of the fluids discharged from the Bouillante wells is unchanged after more than 15 years of production of the power plant commissioned in 2005, when compared with other water samples previously collected and analysed. Consequently, for the works of geochemical modelling foreseen within the framework of the REFLECT project, relative to the scale deposits which could occur during the exploitation of the Bouillante reservoir, especially for amorphous silica precipitation, similar chemical compositions as those used in previous studies can be selected.

In the third part of the report, the geothermal fluids of high-temperature geothermal fields in Iceland are described. The country has been divided into volcanic zones based on the volcanic eruption style, the magmatic products, and the position relative to the mid-ocean ridge (MOR) and the Icelandic mantle plume. The Northern Volcanic Zone (NVZ) has been the main spreading zone in the north of Iceland for the past 6-7 Ma, characterized by oblique extension creating five *en echelon* spreading segments in the NVZ. Each segment has a fissure swarm and an associated central volcanic activity that focuses on volcanic and high-temperature geothermal activities. These volcanic centers are Kverkfjöll, Askja, Fremrinámar, Krafla, and Theistareykir (Pedersen et al., 2009), of which high-temperature fluids were sampled from geothermal fields of the latter two in the context of the REFLECT project. Results from measured chemical composition, and the stable water, carbon, and sulphur isotope analysis are presented in the report. The calculated chemical composition of the deep liquid from the two-phase production wells based on the methods described in Section 4.3.2 is also presented.

2 HIGH-TEMPERATURE GEOTHERMAL FLUIDS FROM TURKEY

Western Anatolia in Turkey is an active tectonic zone, which is known for its geothermal system. The geodynamics of Western Anatolia differs from other parts of Anatolia, illustrated by the extensional tectonics, crustal thinning, and the formation of large graben systems that have been formed in that part (**Fig.1**). Therefore, this active tectonic region, where normal faults are located, still contributes to the development of new geothermal systems. Especially Aydın (Germencik) region is limited by normal faults, and it is a typical horst-graben system. This gigantic horst-graben system, starting from the Aydın region to the Denizli region, is called Büyük Menderes Graben (BMG), and there are many geothermal power plants within this huge graben system (**Fig. 2**). It stretches 150 km in the east-west direction and can be described as a dome-like structure, broken by faulting. The BMG includes various schists and dolomitic marbles and consists of Menderes metamorphic rocks and sedimentary units overlie them. N-S cross-section of the BMG is given in **Fig. 3**.

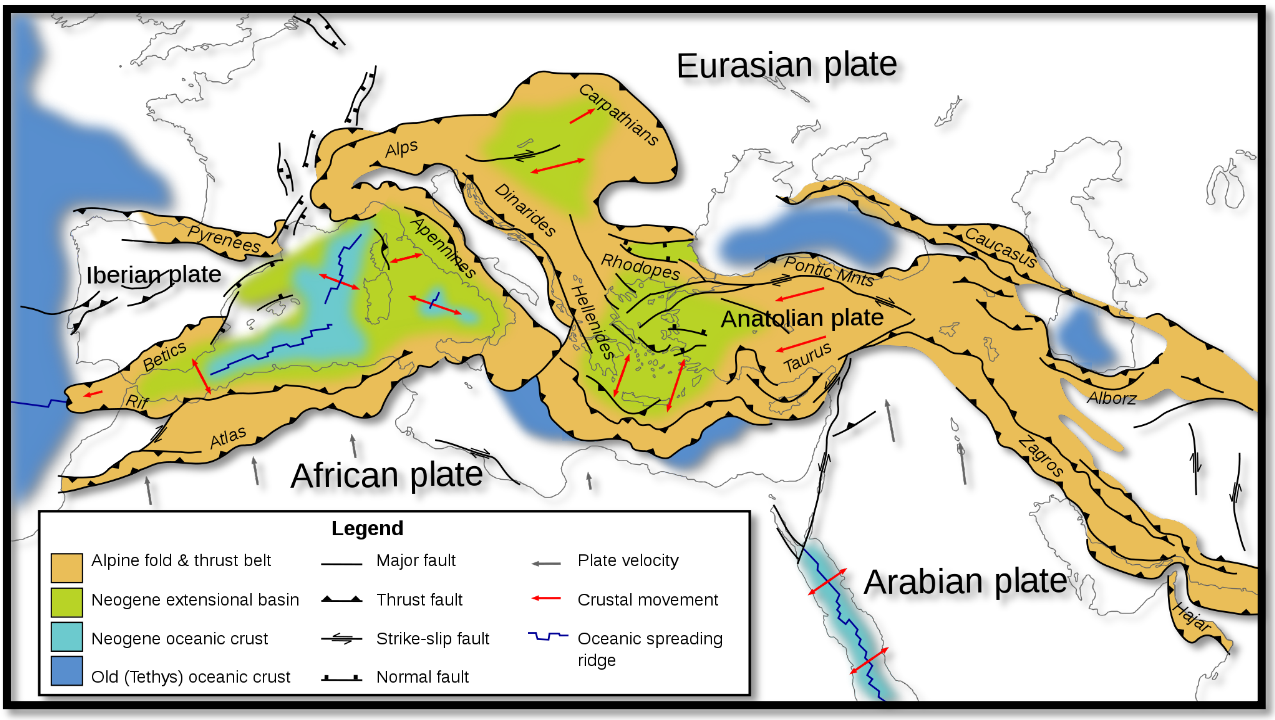

Figure 1: The tectonic boundary of the Anatolia plate (Wikipedia, User: Woudloper)

Within the BMG system, there are low, medium, and high enthalpy geothermal fields, and the reservoir temperatures of the fields differ. Along the BMG from west to east; the Germencik, Salavatlı, Pamukören, Kızıldere (Denizli) fields exhibit high temperature geothermal systems and reservoir temperatures reaching 245°C in Kızıldere (Şimşek, 2003).

The Germencik (Aydın) and Kızıldere (Denizli) fields are two of the hottest, largest, and most developed water-dominated hydrothermal reservoirs discovered in Turkey so far. Germencik geothermal fields have around 100 production and reinjection wells reaching a depth of 2800 m (Özgür, 2018) with temperatures that can reach up to 276°C (Türeyen et al., 2016). The power plant types are selected according to the reservoir temperature and are mostly binary-cycle geothermal power plants. The depths of the geothermal wells in the BMG vary between 1000 m and 3500 m and are deep geothermal systems.

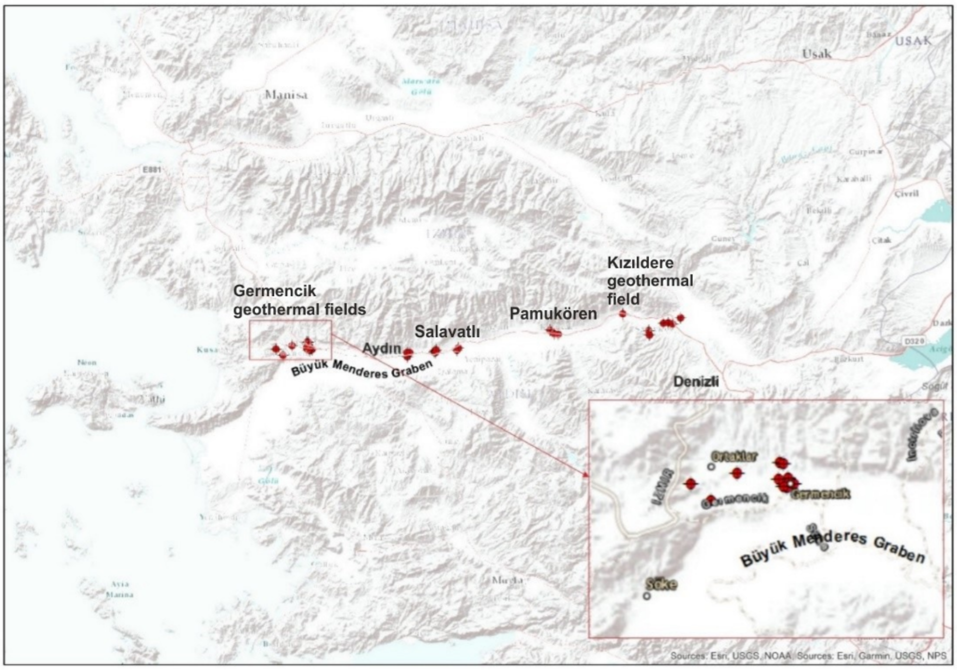

Sources: Esri, USGS, NOAA, Sources: Esri, Garmin, USGS, NPS

Figure 2: Geothermal power plants in the BMG System, Turkey

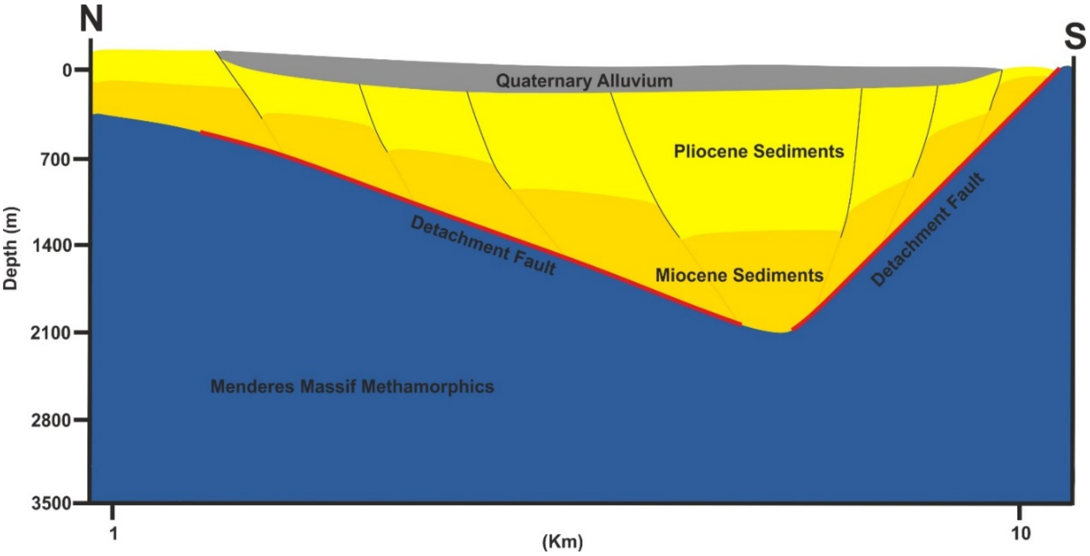

Figure 3: N-S cross-section of the BMG (modified after Yamanlar et al., 2020)

Another major geothermal field located in the western part of Turkey is Tuzla geothermal field (TGF). TGF is situated near the Aegean Sea and is in an active tectonic zone like the Germencik geothermal field (GGF; **Fig. 4**). It is 80 km from the south of Çanakkale and 5 km from the Aegean Sea, on the Biga Peninsula.

The most important difference between GGF and TGF is that GGF has older reservoir rocks than TGF. The geothermal brine in the TGF, which is dominated by NaCl, has a typical temperature of 173 °C. Different scale problems, which are the most common issue in the geothermal fields, are observed in these two fields. While the GGF has a sulfide-type scale in the surface equipment system, the TGF has a silica-based scale in the borehole systems. In this study, the scale problems in both areas will be discussed, and the factors affecting the scale formation and their reasons will be studied in detail.

In this report, firstly, the GGF will be tried to investigate for a one-year period.

Figure 4: The location map of the TGF and GGF

2.1 INTRODUCTION - GERMENCİK POWER PLANT

The GGF is located in the western part of the BMG, where it changes its direction turning from the E-W direction toward NW-SE orientation (Fig. 4). This direction change is a significant geological structural event. This situation has caused that geothermal resources have many faults and fractures, and as a result, lithological units have substantial permeability in this region.

The surface installations of the GGF can be seen in **Fig. 5**. In this field, there are a total of 25 geothermal wells (11 production wells, 9 reinjection wells and, 5 observation wells) with depths varying between 1400 and 3000 m. The GGF has a binary cycle geothermal power plant. Geothermal studies on the GGF have been ongoing since 1965. That is, hot water from the reservoir is not sent directly to the turbine. First, hot water coming from the reservoir enters the heat exchanger system, and then organic working fluid changes phase and enters the steam turbine (**Fig. 6**).

The most important problem in the GGF is sulfide-type scale in the surface equipment system.

Figure 5: Surface installations of the Germencik geothermal field (GGF)

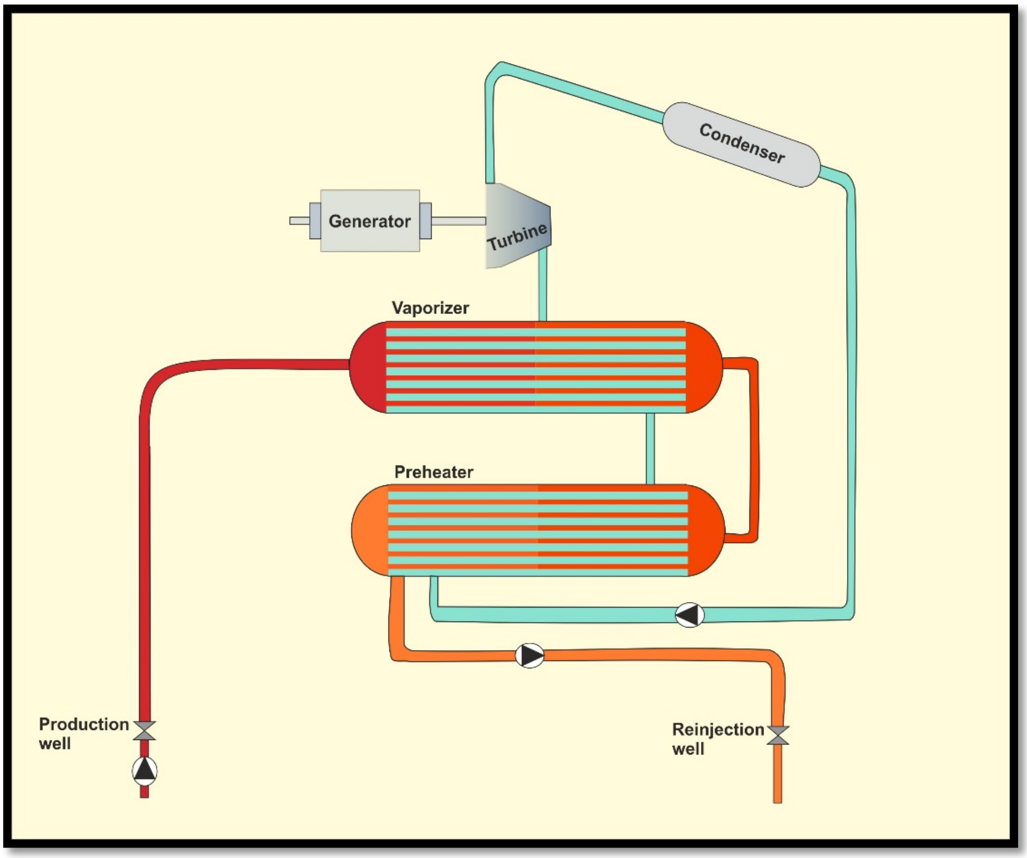

Figure 6: Binary cycle GGF layout

2.1.1 GEOLOGY OF THE GGF

The BMG is located in crystalline Menderes massif, which is the largest metamorphic massif in Turkey. This graben, which has been broken by normal faults during the alpine orogenesis, presents a dome-like structure. The Menderes Massif consists of metamorphic rocks that include schists and dolomitic marbles. Sediment deposits overlie them. Geological and geophysical studies showed stepwise graben development, which is an important characteristic of geothermal fields, occurred in the northern part of the graben (Faulds et al., 2010). The geological history of the Menderes Massif can be divided into paleotectonic evolution and neotectonic evolution. Magmatism, metamorphism, and deformations occurred in the paleotectonic evolution of the Menderes Massif. Rock units exposed in the vicinity of Büyük Menderes Graben can be classified into two groups: the basement and basin-fill units. Metamorphic rocks belonging to Menderes Massif constitute the pre-Neogene basement units, which is an extensional metamorphic core complex in the Western Anatolian extensional province (Bozkurt, 2001). The basin fill consists of four sedimentary packages formed on the metamorphic rocks of the Menderes Massif (Bozkurt, 2000; Sözbilir and Emre, 1990). The first sedimentary package is made up of blocky conglomerates and conglomerates containing block-sized components. With these features, the first sedimentary packages show the characteristics of an alluvial fan from west to east. The sediments belonging to the second sedimentary package are characterized by reddish-colored terrestrial conglomerate and sandstone. The third sedimentary package is composed of dominant conglomerate and sandstone alternation. The facies characteristics of this unit indicate that it is controlled by E-W trending faults. The sediments of the fourth sedimentary package are formed by the alluviums that fill the Büyük Menderes Graben today. These sediments are made up of fine-grained river sediments carried by the Büyük Menderes River. The sequence continues its formation today (Sözbilir, 2001). The most important characteristic of the BMG is asymmetry, which means a steeper northern side, and most of the hot springs are concentrated along the north side. Intersection regions between N–S Miocene grabens and the actual E–W grabens in the BMG have a suitable fractured medium for the formation of geothermal systems. Thanks to the geological formation and active tectonism, the BMG has a great advantage in terms of geothermal. To illustrate, although most of these geothermal systems are located in reservoirs with medium enthalpies, which have 120−180°C, the Germencik and Kızıldere geothermal fields are two of the hottest and largest, water-dominated hydrothermal reservoirs discovered in Turkey so far. The Kızıldere geothermal field has approximately 245°C reservoir temperature, whereas some parts of the Germencik field has temperatures up to 276°C (Türeyen et al., 2016). The reservoir temperature of the geothermal fluids in the BMG varies from region to region. The reservoir temperature in the western end of the BMG can reach 276°C, while it can reach 245°C at the eastern end. In the middle part of the BMG, the reservoir temperature of the geothermal fluid is around 169-188°C. This high temperature in the reservoir is due to the rapid rise of the upper crust, causing erosion and high heat flow. During the uplift period, metamorphic rocks were fractured due to the effect of detachment faults, causing the geothermal fluid to rise in the region. The reservoirs of the Germencik and Kızıldere geothermal fields are located in metamorphic rocks with different lithological units. The most important feature of these metamorphic rocks is that they have a deeply located gneiss layer overlying them. The conceptual model of the GGF is given in **Fig. 7**. While creating the conceptual model, borehole logs of all 25 wells in the field were used to obtain a more accurate model. The model was obtained using licensed Leapfrog Geothermal software.

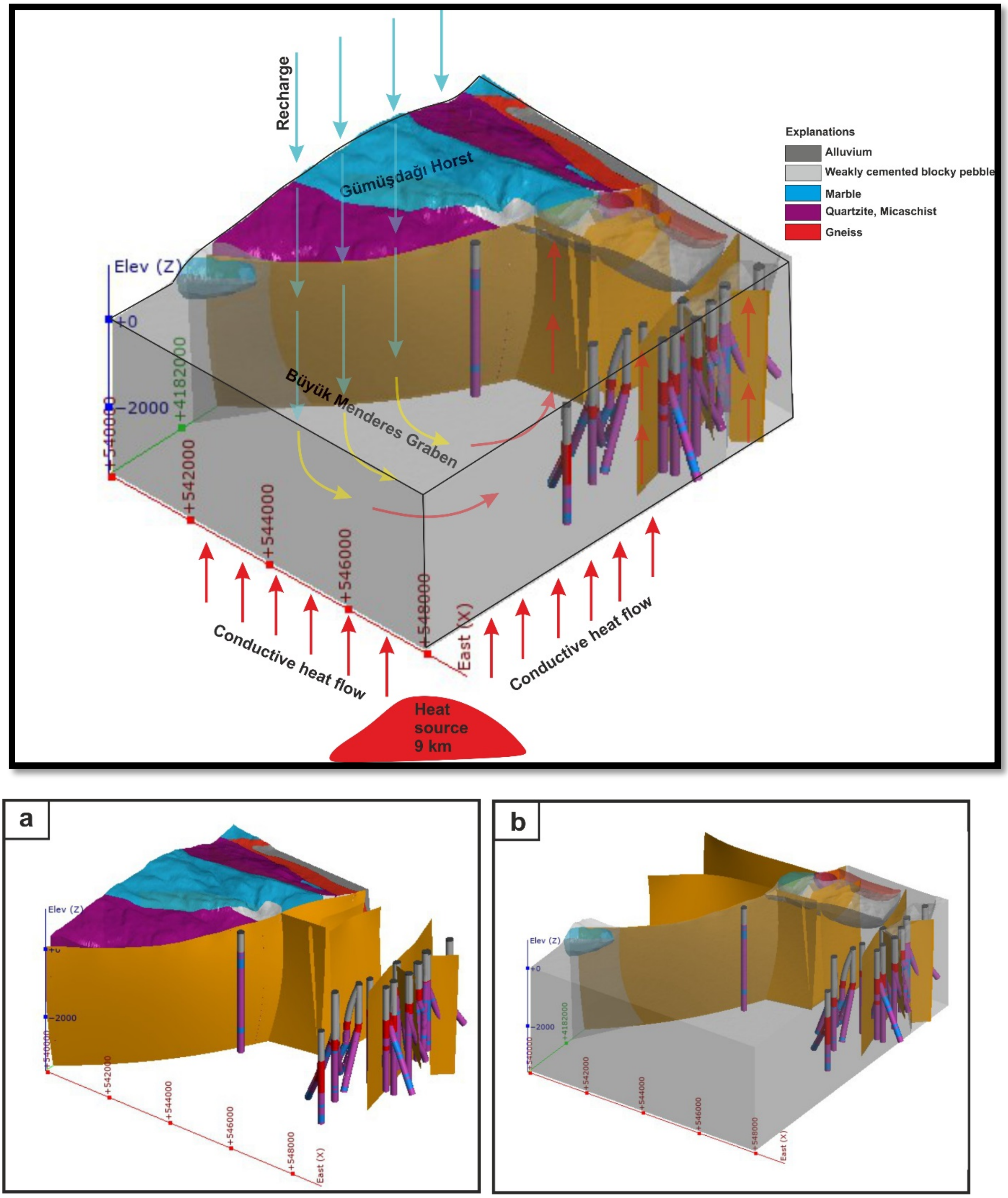

Figure 7: The conceptual model of the Germencik geothermal field (GGF)
a) West block, b) East block

The Germencik geothermal field has two main geothermal reservoirs. Germencik is an active geothermal area hosted by Menderes Massif. Geothermal brine is found in a deep metamorphic reservoir at a depth of between around 2000 m and 3000 m, and a deep marble reservoir has been detected at a depth of 1440 m. The first consists of mainly Neogene aged conglomerate and sandstone. The second includes Menderes Metamorphic rocks. Quartzite, quartzite-schist, calcschist, mica schist, graphite schist, gneisses are basement rocks of the geothermal system. The main fault systems in the study area are located in the north and west of the site. A detailed geology map of the GGF is given in **Fig. 8**. The geothermal reservoir rocks in the geothermal field are Neogene limestones (the first reservoir), Paleozoic marbles, and quartzite schist in the basement complex (the second reservoir). In addition to graben morphology formed under the extensional tectonic regimes of the region, the Menderes massif has gained its present position along the low-angle normal faults of the Oligo-Miocene period. At the same time, as a result of tectonics, a favourable environment has been formed for geothermal systems in the region.

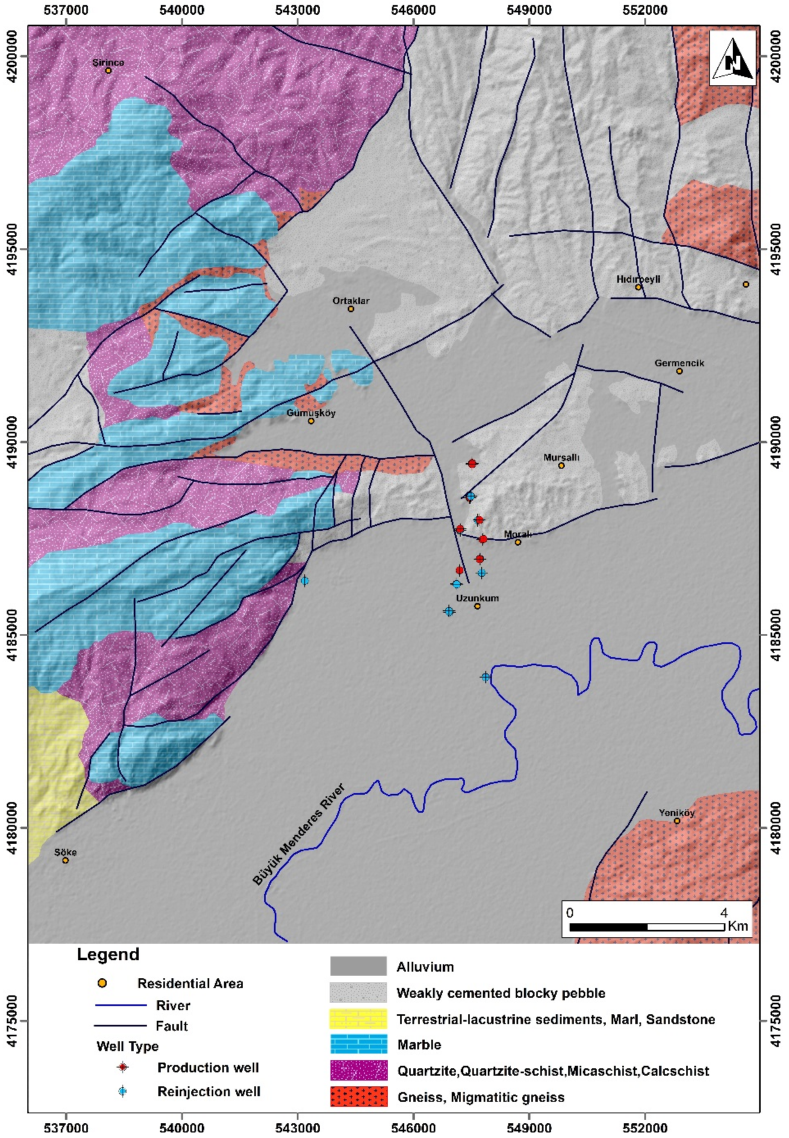

Figure 8: Geology map of the GGF and near surrounding

2.2 METHODS

2.2.1 Geothermal water sampling

During the REFLECT project geothermal water sampling studies were carried out at different dates in the GGF. Geothermal water samples were collected from the wells and surface equipment system. Information on water sampling on different dates is given in **Table 1**.

Table 1: Sampling dates in the GGF

Sampling Date	Location	Explanations	Aim
17/06/2020	Aydın (Germencik)	• 9 geothermal water samples from the production well • 2 geothermal water samples from the reinjection well + • Preheater in & • Preheater out	➢ to determine the physical properties of the geothermal waters ➢ to determine major and minor anions-cations of the geothermal wells ➢ to determine isotopes (^{18}O, deuterium, tritium)
24/02/2021	Aydın (Germencik)	• 11 geothermal water samples from the production well	➢ to determine ^{34}S of dissolved sulphate and sulfides and ^{13}C-CO_2

In the field study carried out on 17/06/2020, a total of 11 geothermal water sampling was carried out, including 9 production and 2 reinjection wells (**Fig. 9**). Water samples were collected from the wellheads (**Fig. 10**) and also from preheater in and preheater out (**Fig. 11**). 100 mL plastic bottles for heavy metal analysis, 250 mL plastic bottles for major-minor anions and cations, and 1 L plastic bottles for isotopes were used. After collecting samples for heavy metal analysis, they were acidified with 2% HNO_3. The aim is to prevent heavy metals from settling in the bottles. After collecting all the samples, the caps of the bottles were tightly closed, and contact of the samples with air was prevented. Physical and chemical parameters of the geothermal waters were analysed in the laboratories of the Izmir Institute of Technology. Major and minor analyses were performed on ICP-MS (Inductively Coupled Plasma Mass Spectrometry), and heavy metal analyses were performed on ICP-OES (Inductively Coupled Plasma Optical Emission Spectroscopy) device. The SiO_2 values of the geothermal waters were determined by the UV-spectrophotometric method with Hach-Lange DR5000. Isotope analysis of the geothermal waters was carried out in the State Hydraulic Works (DSİ) laboratories in Ankara, Turkey.

On 24/02/2021, samples were also collected for isotopes ^{34}S on sulphide and sulphate, and ^{18}O on sulphate and $^{13}C\text{-}CO_2$. Six geothermal water samples were collected for $^{13}C\text{-}CO_2$ analysis, and 5 geothermal water samples were collected for dissolved sulphate analysis. Steel cylinders were used for $^{13}C\text{-}CO_2$ analysis, and 5L canister bottles were used for dissolved sulphate analysis. These samples will be analysed by the project partner, Hydroisotop (HI).

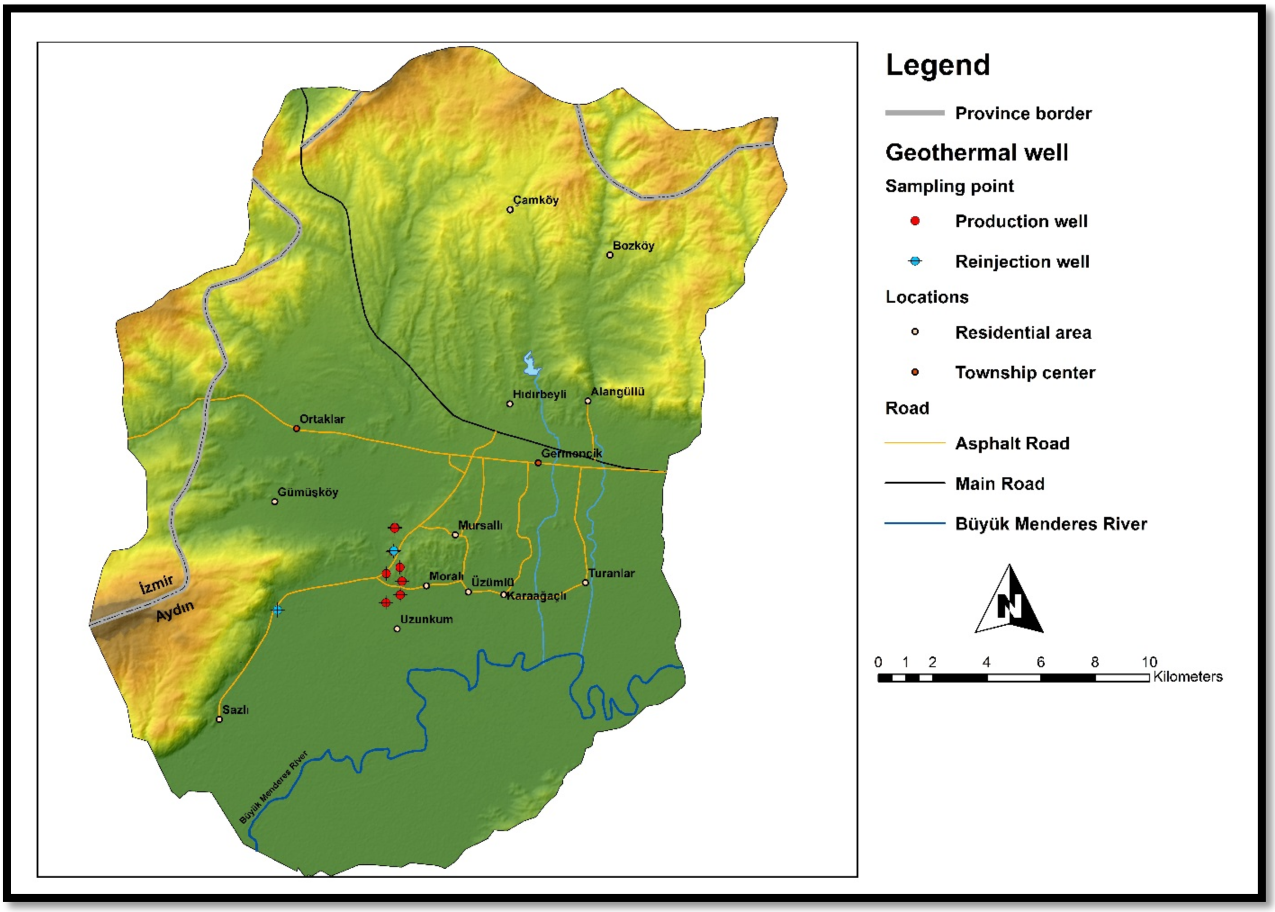

Figure 9: Sampling points in the GGF

Figure 10: Sampling point in the geothermal wells

Figure 11: Sampling point in the surface equipment system (preheater)

2.2.2 Rock and scale samples

Rock samples at different depths were collected from some of the geothermal wells, and the samples were analysed in the laboratories of the Izmir Institute of Technology. XRD, XRF, and SEM analyses of rock samples belonging to geothermal wells were performed. The aim here is to reveal the paths followed by geothermal waters while reaching the surface from the depths and the rock-water relationship. In other words, borehole core samples were taken in order to understand the rock types with which the waters are in contact. In addition, understanding the relationship between sulfide-type scale in the GGF and reservoir rocks by XRD, XRF, and SEM analysis is another goal.

In addition to the rock samples, scale samples were collected from the preheater system at the GGF, and XRD, XRF, and SEM analyses were performed.

X-ray crystallography (XRD), X-ray fluorescence spectroscopy (XRF), and scanning electron microscope (SEM) analyses of rock samples were carried out in the laboratory of İzmir Institute of Technology. XRF analyses of 4 rock core samples collected from geothermal wells (W_TR_002, W_TR_003, W_TR_007, and W_TR_009) were performed on the Spectro IQ II device. Spectro IQ II can deliver element concentrations from Sodium (Na-11) to Uranium (U-92) with high sensitivity at ppm-level. Also, by using Philips X'Pert Pro, X-ray diffraction (XRD) analyses of rock samples were performed. XRD gives information about the concentration of phases, the amount of non-crystalline phases, and the crystal size of the material. By using FEI QUANTA 250 FEG scanning electron microscope (SEM), rock structures were visualized in micro size.

Information on rock samples collected from the geothermal wells at different depths is presented in **Table 2**.

Table 2: Rock sample in the geothermal wells at different depths

Well ID	Sampling Method	Sample depth (m)	Rock type	XRF sample mass (g)	Sample state	Sample rotation
W_TR_002	Core sample	1145-1170	Gneiss	0.96	powder	no
		2140-2190	Marble	0.83	powder	no
		2325-2335	Mica schist	1.06	powder	no
		2670-2685	Marble	1.01	powder	no
		2855-2865	Marble	0.84	powder	no
W_TR_003	Core sample	1225	Schist	1.10	powder	no
		1665-1675	Schist	0.95	powder	no
		2235	Quartzite	1.13	powder	no
		2995	Schist	0.94	powder	no
		3005	Schist	1.05	powder	no
W_TR_007	Core sample	1000-1040	Quartzite	1.35	powder	no
		1245-1250	Quartzite	1.07	powder	no
		1265-1285	Quartzite, schist	1.01	powder	no
		1960-1965	Schist	0.93	powder	no
		2380-2385	Schist	1.00	powder	no
W_TR_009	Core sample	600-625	Gneiss	1.02	powder	no
		900-920	Micaschist	1.13	powder	no
		1000-1010	Marble	1.08	powder	no
		1910-1995	Quartzite	1.24	powder	no
		2100-2170	Quartzite	1.08	powder	no
		2200-2250	Schist	1.04	powder	no
		2450-2530	Quartzite	1.03	powder	no

2.3 RESULTS

2.3.1 Hydrochemistry of the geothermal waters

2.3.1.1 Physical properties of the geothermal waters

The pH values of the geothermal waters in the GGF are between 6.7 and 8.54. Electrical conductivity values vary between 5697 µS/cm and 7507 µS/cm. Total dissolved solids (TDS) was determined using a digital TDS meter. TDS of the geothermal fluids range from 3700 to 4200 ppm. The outflow temperatures of production wells are between 125°C and 148°C, and about 64°C in the reinjection wells. The highest outflow temperature is in the W_TR_009 well. The physical properties of the geothermal waters and the well depths are given in **Table 3**.

Table 3: Physical properties of the water samples

No	Well ID	pH	EC µS/cm	T (°C)	TDS (ppm)	Depth (m)	Well type
1	W_TR_001	7.1	5937	125.3	3700	3328	Production
2	W_TR_002	6.87	5961	134.36	3900	3165	Production
3	W_TR_003	8.24	6030	140.06	3700	3074	Production
4	W_TR_004	8.54	6101	140.57	4000	3135	Production
5	W_TR_005	7.82	5999	138.41	3900	3135	Production
6	W_TR_006	6.25	6070	132.13	4200	1449	Production
7	W_TR_007	8.47	6131	145.76	4100	2451	Production
8	W_TR_008	7.62	6147	64.83	3900	2907	Reinjection
9	W_TR_009	6.7	5697	148.09	3900	2568.34	Production
10	W_TR_010	6.85	6049	143.65	3800	2680	Production
11	W_TR_011	7.45	6131	64.51	4000	3525	Reinjection
12	Preheater in	7.35	6074	80	3900	-	Surface equipment
13	Preheater out	7.85	6090	65	4000	-	Surface equipment

2.3.1.2 Chemical properties of the geothermal waters

The chemical properties of geothermal waters are given in **Table 4**. Based on chemical analyses, the geothermal waters in the GGF present the Na-Cl-HCO_3 water type. Na-Cl-HCO_3 waters are located in marble, quartzite, and mica-schist units, which are reservoir rocks for the geothermal waters.

As can be seen in **Table 4**, sodium (Na^+) and chloride (Cl^-) concentrations are relatively higher than other chemical constituents. The Na^+ is the major cation in the geothermal waters of the GGF, with concentrations ranges from 1072 to 1355 mg/l.

The Na^+/K^+ ratio in the geothermal waters is a good indicator in terms of the paths followed by the waters, low Na^+/K^+ (< 15) ratio meaning high temperatures in the geothermal waters (Nicholson, 1993). The low Na^+/K^+ ratio means that geothermal waters rise rapidly as they rise from the depths to the surface and do not have enough time to cool. The ratio of Na^+/K^+ in the GGF is 20 and high. Therefore, the geothermal waters rise to the surface slowly, transfer heat to the surrounding rocks, and cool down. This situation indicates the presence of near-surface reactions and conductive cooling in geothermal waters. As salinity increases in the geothermal waters with respect to reservoir temperature and rock types, Ca^{2+} values also increase. Ca^{2+} and HCO_3^- values in geothermal waters are associated with marbles in Menderes metamorphic rocks. Silica (SiO_2) values are possibly due to the quartz mineral found in rocks such as quartzite and schist.

Table 4: Chemical properties of the water samples (mg/l)

No	Well ID	Ca^{2+}	Mg^{2+}	Na^{+}	K^{+}	Cl^{-}	SO_4^{2-}	HCO_3^{-}	SiO_2	Water Type
1	W_TR_001	7.40	2.64	1324.56	64.03	1312.33	37.41	1180.21	125	Na-Cl-HCO_3
2	W_TR_002	6.89	1.75	1319.22	62.64	1305.01	34.86	1230.54	145	Na-Cl-HCO_3
3	W_TR_003	14.41	1.58	1319.41	59.97	1328.42	38.12	1148.03	140	Na-Cl-HCO_3
4	W_TR_004	8.68	1.00	1355.79	63.59	1344.67	38.68	759.72	155	Na-Cl-HCO_3
5	W_TR_005	32.53	2.37	1301.49	65.99	1308.80	34.29	1206.28	150	Na-Cl-HCO_3
6	W_TR_006	48.29	4.15	1072.65	58.43	1183.42	12.85	1468.41	145	Na-Cl-HCO_3
7	W_TR_007	13.19	0.75	1352.62	64.77	1352.37	35.5	904.77	165	Na-Cl-HCO_3
8	W_TR_008	25.08	1.88	1352.98	65.92	1340.18	31.63	1313.15	165	Na-Cl-HCO_3
9	W_TR_009	12.17	0.79	1224.32	62.44	1225.77	34.25	1153.21	165	Na-Cl-HCO_3
10	W_TR_010	44.56	3.39	1281.19	66.22	1250.75	31.22	1447.48	140	Na-Cl-HCO_3
11	W_TR_011	24.53	1.74	1345.58	66.38	1337.69	32.47	1356.18	135	Na-Cl-HCO_3
12	Preheater in	19.71	1.20	1244.92	64.01	1357.74	33.89	1307.45	130	Na-Cl-HCO_3
13	Preheater out	21.39	1.33	1244.03	63.33	1354.89	34.76	1331.42	125	Na-Cl-HCO_3

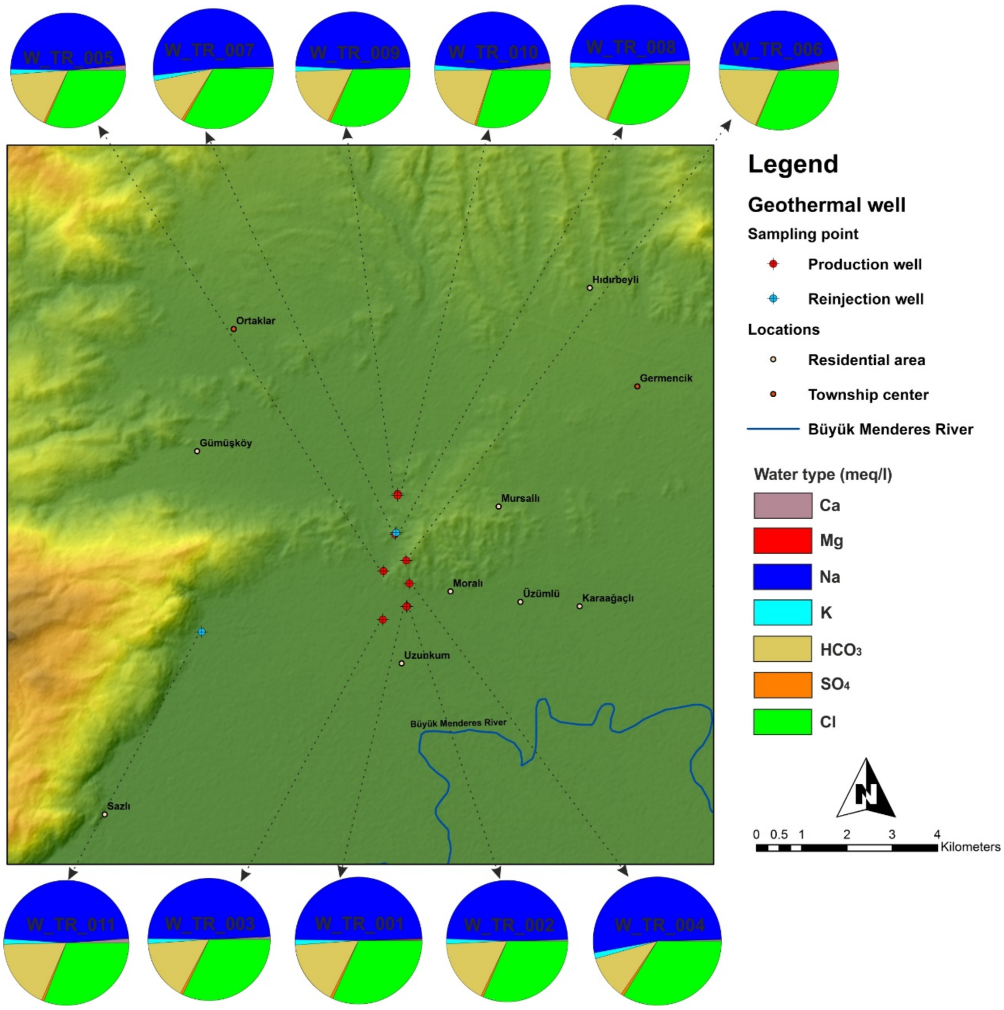

Figure 12: Distribution of the major anions and cations in the GGF

Anion and cation distributions in the GGF are given in **Fig. 12**. As can be seen from the Pie diagrams, Na^+ is the dominant cation, HCO_3^- and Cl^- are the dominant anions. Piper diagrams (**Fig 13** and **Fig. 14**) are triangular diagrams used to classify waters and express water facies. It is seen that geothermal waters show similar facies characteristics in piper diagrams. The GGF water samples are in the bicarbonate water group, and they are considered peripheral waters.

The semi-logarithmic Schoeller diagram (**Fig. 15** and **Fig. 16**) shows that geothermal water samples have a similar composition in the GGF. It is seen that the concentrations of Mg^{2+} and SO_4^{2-} in geothermal waters decrease, and the latter are enriched in Ca^{2+}, Na^+, K^+, Cl^-, and HCO_3^- (**Fig. 15** and **Fig. 16**).

From the piper and Schoeller diagrams of the water samples collected from the geothermal wells and surface equipment system, it is seen that there is no significant change in the water chemistry of the geothermal water from the production to the preheater system.

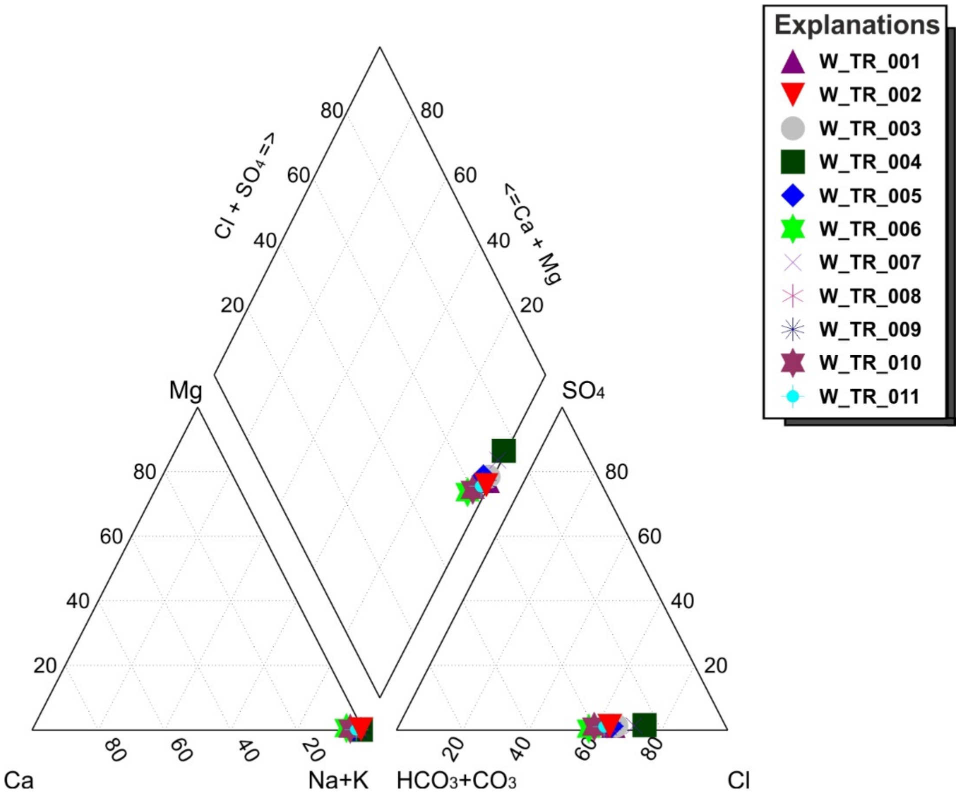

Figure 13: Piper diagram of the geothermal waters in the GGF

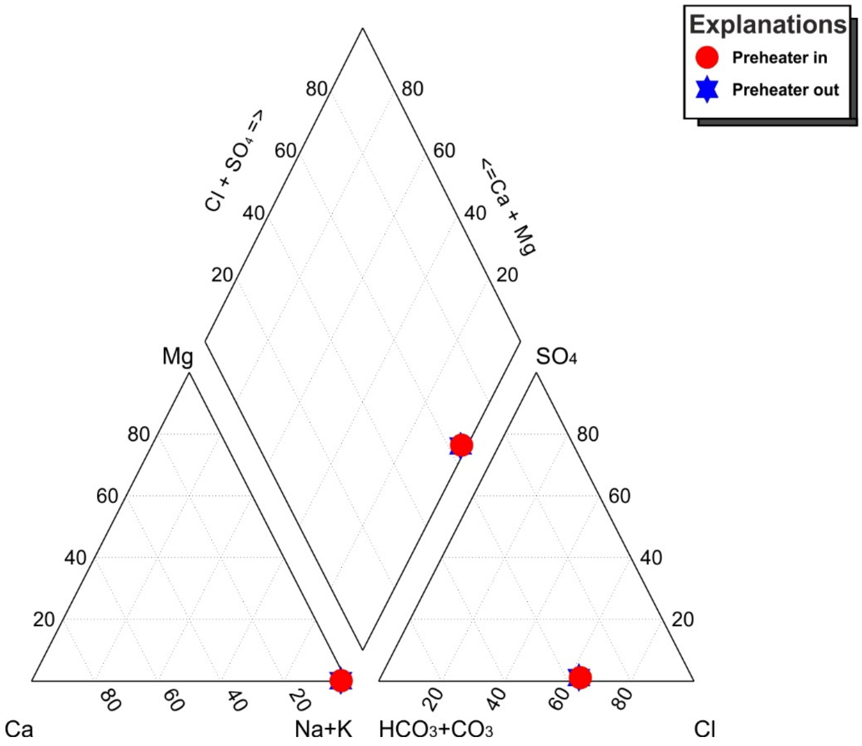

Figure 14: Piper diagram of the surface equipment (preheater) in the GGF

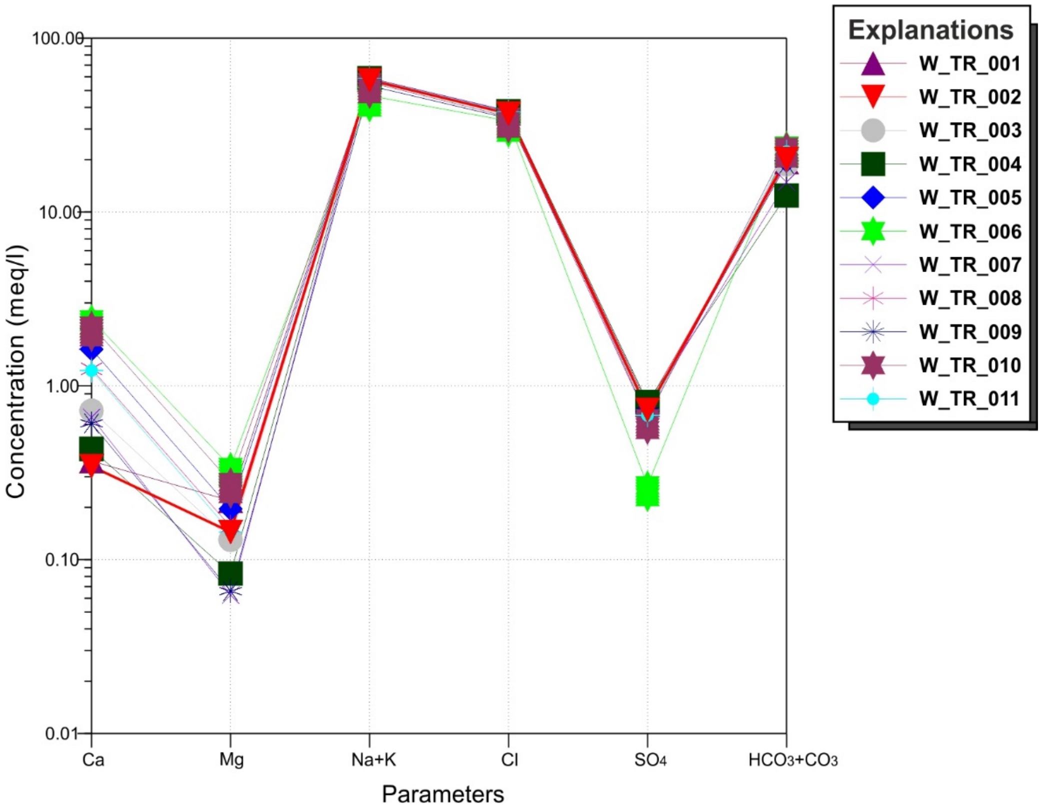

Figure 15: Schoeller diagram of the geothermal waters in the GGF

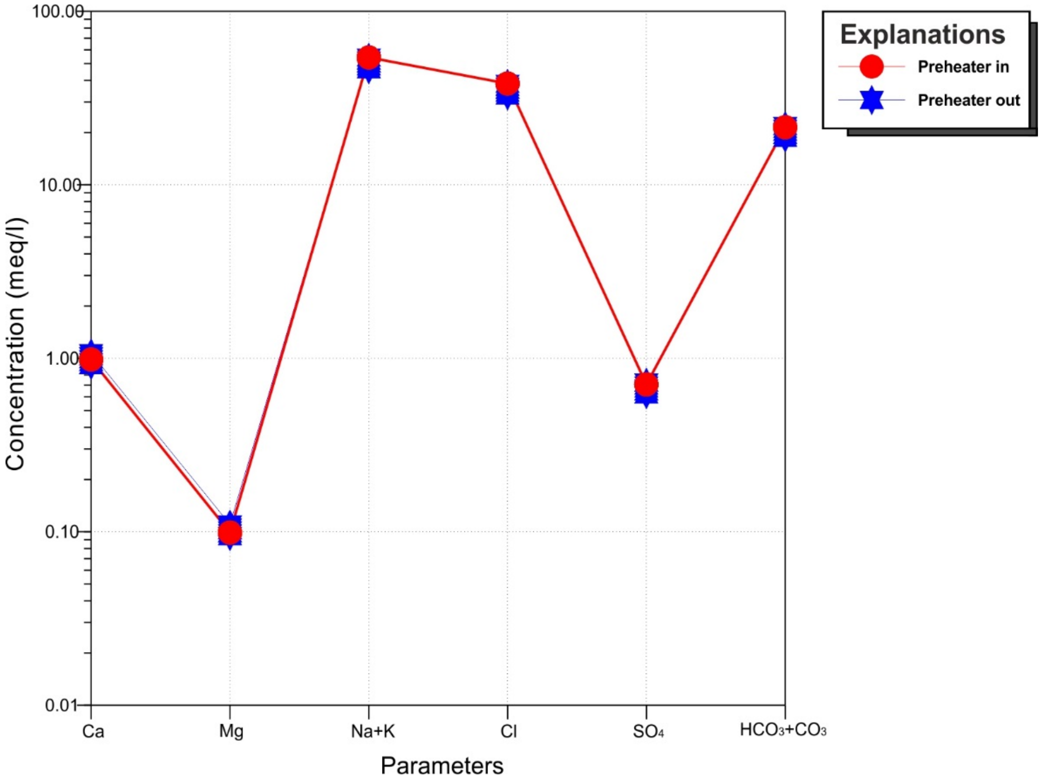

Figure 16: Schoeller diagram of the surface equipment (preheater) in the GGF

The chloride (Cl^-) concentrations range from 1183 to 1357 mg/l in the GGF, which is located 20 km from the Aegean Sea. Karakuş and Şimşek (2013), and Güner and Yıldırım (2005) explained that the Cl^- concentrations are associated with marine sediment effect during the Pleistocene in the GGF. The same authors stated that the effect of seawater intrusion on GGF is 7-8%. Aggarwal et al. (2000) stated that high Cl/B ratios might indicate seawater effect, while low Cl/B ratios are associated with magmatic volatiles. The Cl/B ratio for the GGF is given as 28.10. Baba and Sözbilir (2012) stated that geothermal waters could gain their chloride concentrations from hot water associated with faults.

In geothermal waters, Cl^- and B elements are important in understanding the water-rock interaction. Germencik geothermal waters are rich in chloride (Cl^-) and modest in boron (B) elements. Boron concentrations range from 36 to 50 mg/l in the GGF. Chloride and boron elements indicates that geothermal waters are recharged from the same deep reservoir (**Fig. 17**). The boron in the geothermal waters is probably not derived from the sedimentary rocks and possibly from metamorphic ones such as gneiss and schist (**Fig. 17**).

The origins of boron in thermal waters have been discussed by different researchers (Gemici and Tarcan, 2002; Özgür et al, 2004; Vengosh et al., 2002; Tokçaer, 2007). Filiz et al. (2000) explained that boron values in geothermal waters are associated with the mantle or marine sediments undergoing metamorphism. According to Karakuş and Şimşek (2013), leaching B^{3+} from the boron-bearing mineral phases in the metamorphics and as magmatic volatiles, $B(OH)_3$ gas intrusions are a known origin of boron in geothermal systems. Gemici and Tarcan (2002) stated that at low pH $B(OH)_3$ and at high pH (> 8) conditions $B(OH)_4$ can be the dominant species in the metamorphics. These results show similarity with those of Gemici and Tarcan (2002).

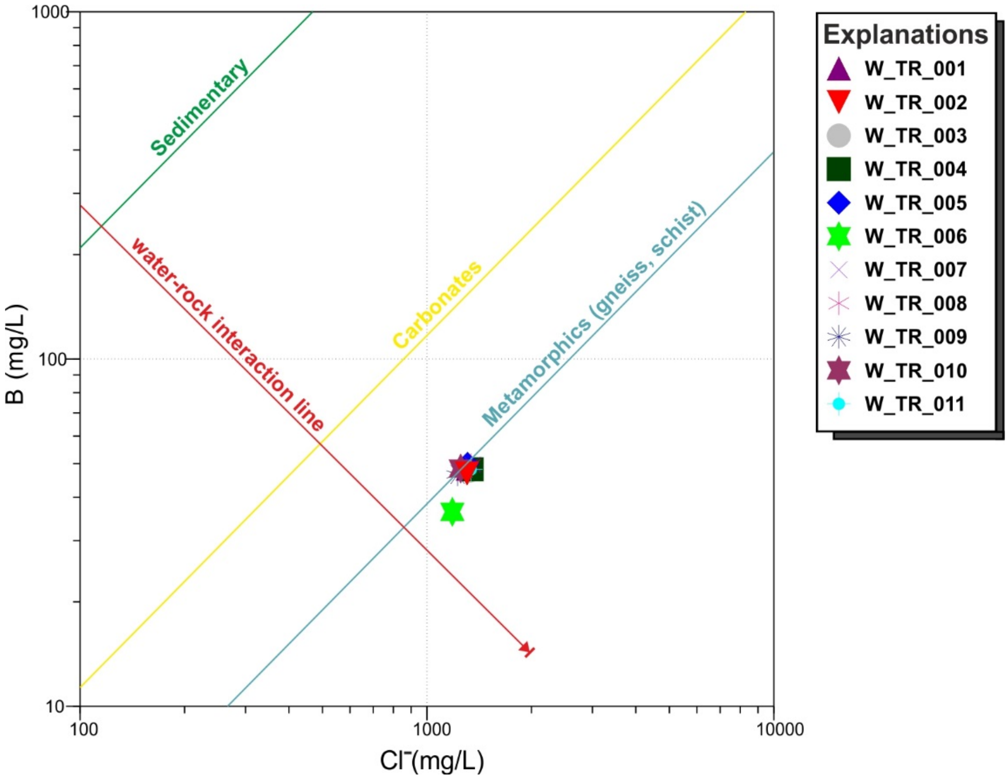

Figure 17: B and Cl- relationship in the GGF

2.3.1.3 Heavy metals and trace elements in the geothermal waters

As can be seen in **Fig. 18**, Aluminum (Al) and arsenic (As) values in the GGF are between 41-233 and 13-153 ppb, respectively. The lowest Al and As concentrations were measured in well W_TR_006. Boron (B) values in geothermal wells are close to each other and average 46 ppm. Boron concentration in geothermal waters is due to boron-containing minerals such as mica and feldspar of the Menderes Massif metamorphics containing pegmatitic tourmalines. Lithium (Li) concentrations in the geothermal waters are also close to each other, and an increase is seen in well W_TR_006. In the geothermal water of the GGF, Li^+ is associated with secondary processes. Therefore, it is used as a trace element. Lithium concentrations of the geothermal waters range from 4.96 to 7.04 ppm. Sb concentrations in the geothermal waters range from 0.94 to 1238 ppb. As seen in **Fig. 18**, the highest Sb concentrations were measured in wells W_TR_003, W_TR_005, and W_TR_008. In the surface equipment system, Sb concentrations increase at the entrance of the preheater. Sb concentrations in the geothermal waters are associated with the schist and gneiss units of the Menderes Metamorphic Massif.

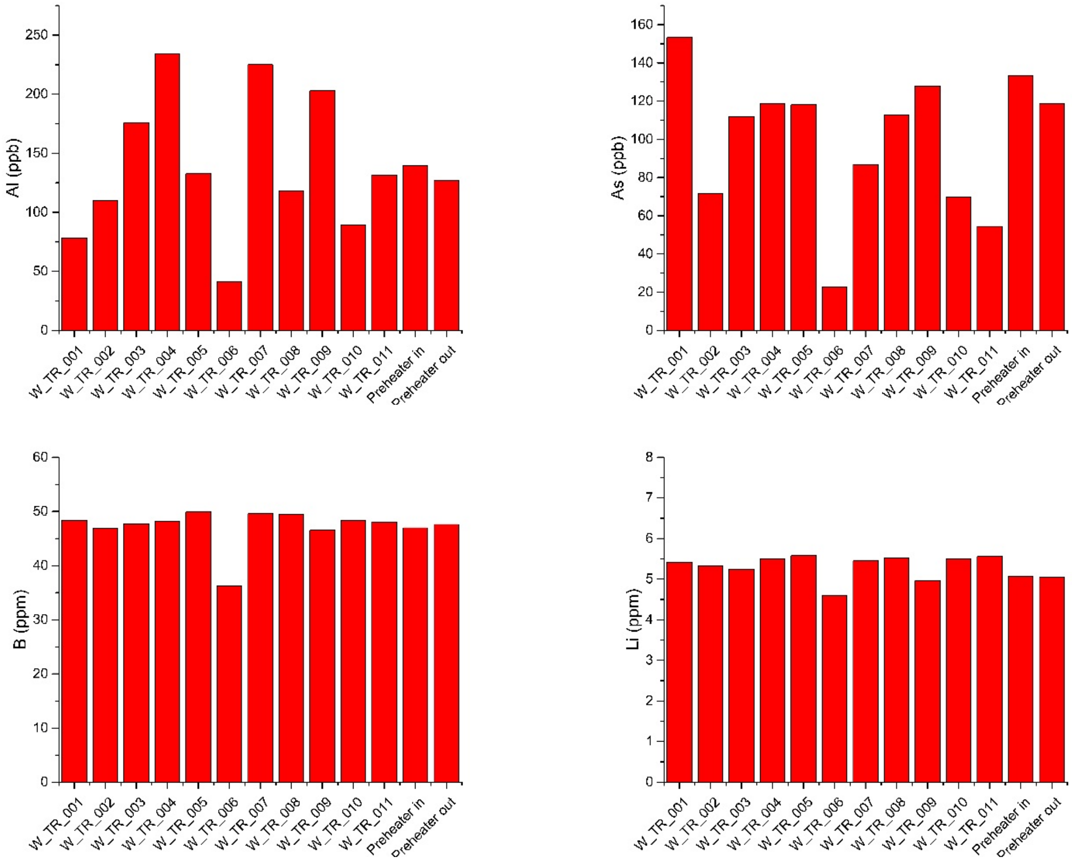

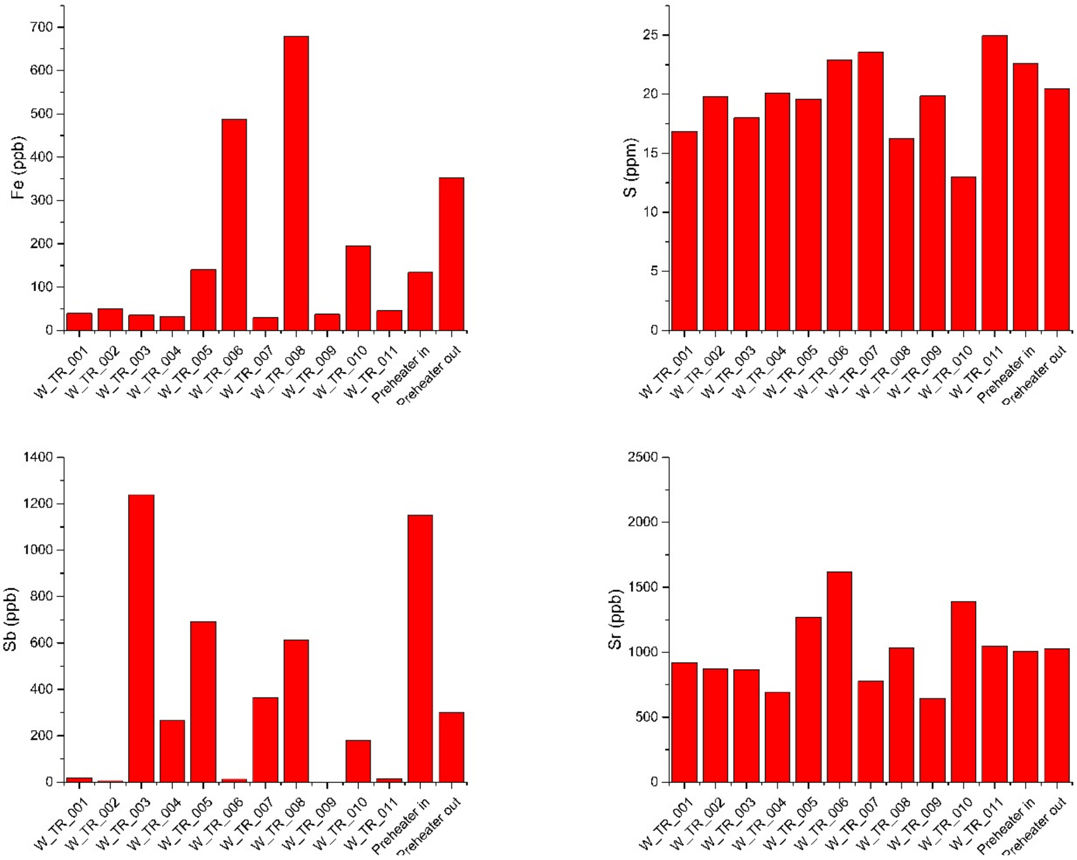

Figure 18: Heavy metal concentrations and trace elements in the geothermal waters for the GGF

2.3.1.4 Isotopes

An isotope study was carried out to understand the origin, recharge areas, and mechanism of geothermal waters in the GGF. Oxygen is the most abundant element in the earth's crust and is generally found in higher amounts in rock reservoirs (Clark and Fritz, 1997). Unlike ^{18}O, ^{2}H (δD) is generally found in waters rather than minerals and rocks. The opposite structure of these two isotopes is important for the isotopic evaluation of waters in high-temperature systems (Clark and Fritz, 1997).

The δ^{18}O isotope values vary between −1.69‰ and −2.05‰, and a δD isotope value variation between −38.07‰ and −40‰ in the thermal waters (**Fig. 19**). The stable isotope results show that geothermal waters have a meteoric origin in the GGF and suggest substantial δ^{18}O isotope enrichment in thermal waters in the Germencik region. This means that geothermal waters have a longer contact time with reservoir rocks at depths. As a result of the interaction between the rocks, which have high isotopes, and the geothermal waters, the geothermal waters were enriched by isotopes, and its composition changed towards positive $\delta^{18}O$ values (**Fig. 19**). Therefore, the high oxygen content may indicate that the geothermal reservoir temperature is high. The geothermal waters show a strong oxygen isotope shift in **Fig. 19** indicating exchange reactions between water and rock over 220°C. In other words, this supports high-temperature geothermal systems in this region and the high dissolution of Sb in the geothermal system. Another reason for the enrichment of the geothermal waters in $\delta^{18}O$ may be the carbonate units containing marble in the Menderes Metamorphic rocks.

Since δD is mostly found in oceans and natural waters, there are more negative values in the geothermal waters (**Fig. 19**).

The most widely used radioactive isotope in hydrogeochemical studies is tritium (^3H) (Dansgaard, 1964). Due to its radioactive nature, it is used in determining the age of groundwater. In addition, the residence time of the groundwater in the reservoir is estimated. The low ^3H (< 5 T.U) content of the geothermal waters in the GGF indicates that the geothermal waters are older than 60 years (**Fig. 20**). Also, the relationship diagram between tritium (^3H) and electric conductivity shows that geothermal fluid has a deep-water circulation (**Fig. 20**).

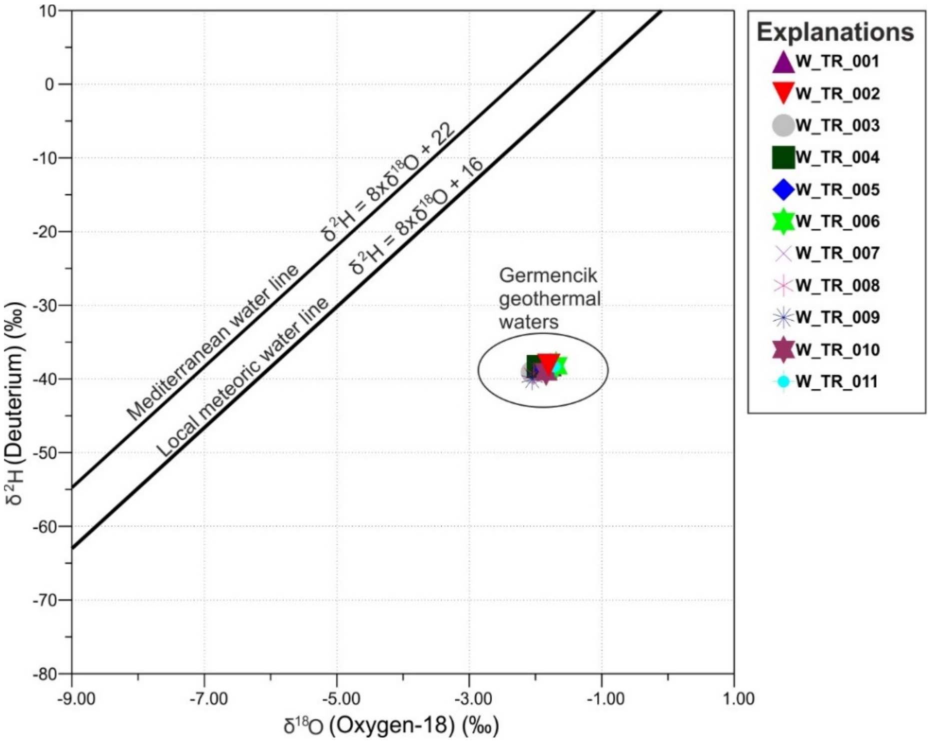

Figure 19: ^2H *vs* ^{18}O graph of the geothermal waters in the GGF

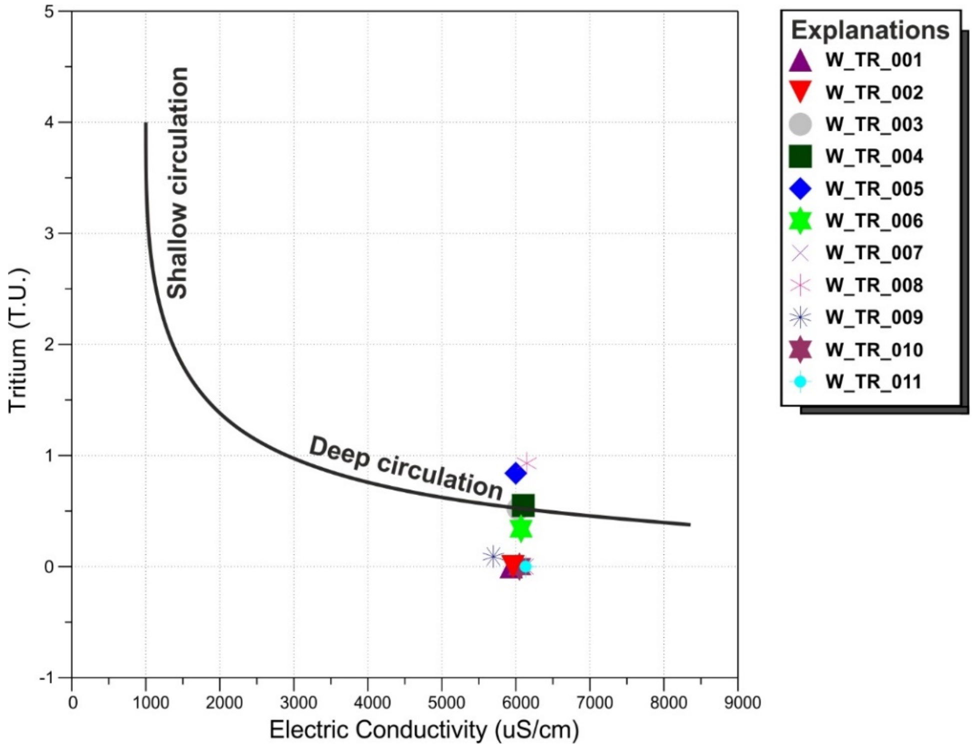

Figure 20: Tritium vs electric conductivity graph of the geothermal waters in the GGF

2.3.2 Evaluation of rock and scale samples

2.3.2.1 Rock samples

Rock samples in different depths were collected from 4 geothermal wells in the GGF. The mineralogy and elemental compositions of the rock samples were evaluated, and the mineral compositions of the reservoir rocks were revealed. W_TR_002 and W_TR_003 are located in the south of the study area, whereas W_TR_007 and W_TR_009 are located in the north of the study area. Two of the wells in which were collected rock samples are located in the south of the study area, while the other two are located in the north.

In the W_TR_002 well, alluvium units are between 0 and 25 m. In 25-905 m, sedimentary units are observed, while Menderes Metamorphic units are observed below 905 m. Rock samples were collected between 2325 and 2335 meters in the W_TR_002 well. As seen in the W_TR_002 well log, there are mica schist units at these depths. As a result of XRD analysis of the W_TR_002 well in a depth of between 2325 and 2335 m, feldspars (albite ($NaAlSi_3O_8$)) and (anorthite ($CaAl_2Si_2O_8$)), silica (quartz (SiO_2)), and iron minerals (pyrite (FeS_2) and magnetite (Fe_3O_4)) were detected. In addition, another mineral found in schists, containing antimony (Sb), which is one of the sulphide minerals, was detected between these depths. (**Fig. 21**).

In the well W_TR_003 with a depth of 3074 m, rock samples were collected at 2995 m. This depth corresponds to the transition zone between the mica-schist units and the marbles. As seen as a result of XRD analysis, carbonate minerals (calcite ($CaCO_3$) and dolomite ($CaMg(CO_3)_2$)) associated with marbles were found at this depth. Feldspar (albite ($NaAlSi_3O_8$)) and silica minerals (quartz (SiO_2)) contained by mica schists were also found at this depth. Diffraction signals at $2\theta = 15°$ and 32° were assigned to antimony (Sb) in the W_TR_003 well (**Fig 21**).

In the well W_TR_007 with a depth of 2451 m, there is alluvium between 0-35 m and sedimentary units between 35-857 m. Metamorphic units are observed at 857 m below. In the well W_TR_007, rock samples were taken between 1265-1285 m, and these depths correspond to calcschist units. In this well, unlike wells, W_TR_002 and W_TR_003, muscovite, one of the mica group minerals, was detected. Enrichment of geothermal waters in muscovite minerals ($KAl_3Si_3O_{10}(OH)_2$)) is attributed to the dissolving of potassium feldspars by geothermal waters. Diffraction signals at $2\theta = 28°$ indicate the presence of antimony (Sb) at this depth in the W_TR_007. Other than that, their mineral composition is similar to the W_TR_002 and W_TR_003 wells.

The W_TR_009 well with a depth of 2568 m has alluvium between 0-35 meters. 35 - 500 m sedimentary units and at 500 m below metamorphic units are observed in this well. Rock sampling was made between 900 and 920 m for this well. In the well log, mica schist units were observed between these depths. Minerals seen in the XRD pattern of the W_TR_009 well have similar characteristics to the other 3 wells. Muscovite ($KAl_3Si_3O_{10}(OH)_2$)), a mica group mineral, was detected in diffraction signals (2θ) at 9°, 32°, and 62°, respectively. Diffraction signals at 22° and 28° indicate feldspar minerals. Diffraction signals in 21°, 39°, 51°, and 68° indicate the presence of quartz minerals in the well W_TR_009.

The rock samples collected from different depths were subjected to elemental analysis using XRF. Chemical compositions of all the rock samples by XRF were evaluated with respect to the different depths in the downhole. **Fig. 22** shows that the elemental compositions of the collected rock samples are enriched in Si, Al, Ca, Fe, K, and Sb. In the wells with the rock samples collected from the north of the GGF, Si values increase, while Al values decrease. The increase/decrease of the elements is related to the reservoir rocks at the depth where the rock sample was collected. For example, Ca, Si, and Al values increased in rock samples collected from depths close to the schist marble contact. On the other hand, an increase was observed in Si, Al, Sb, and Fe values in rock samples collected from depths close to gneiss and schist units.

The findings obtained from the XRD and XRF results show that the Sb scale observed in the preheater system in the GGF is related to the gneiss and schist units in the reservoir rocks.

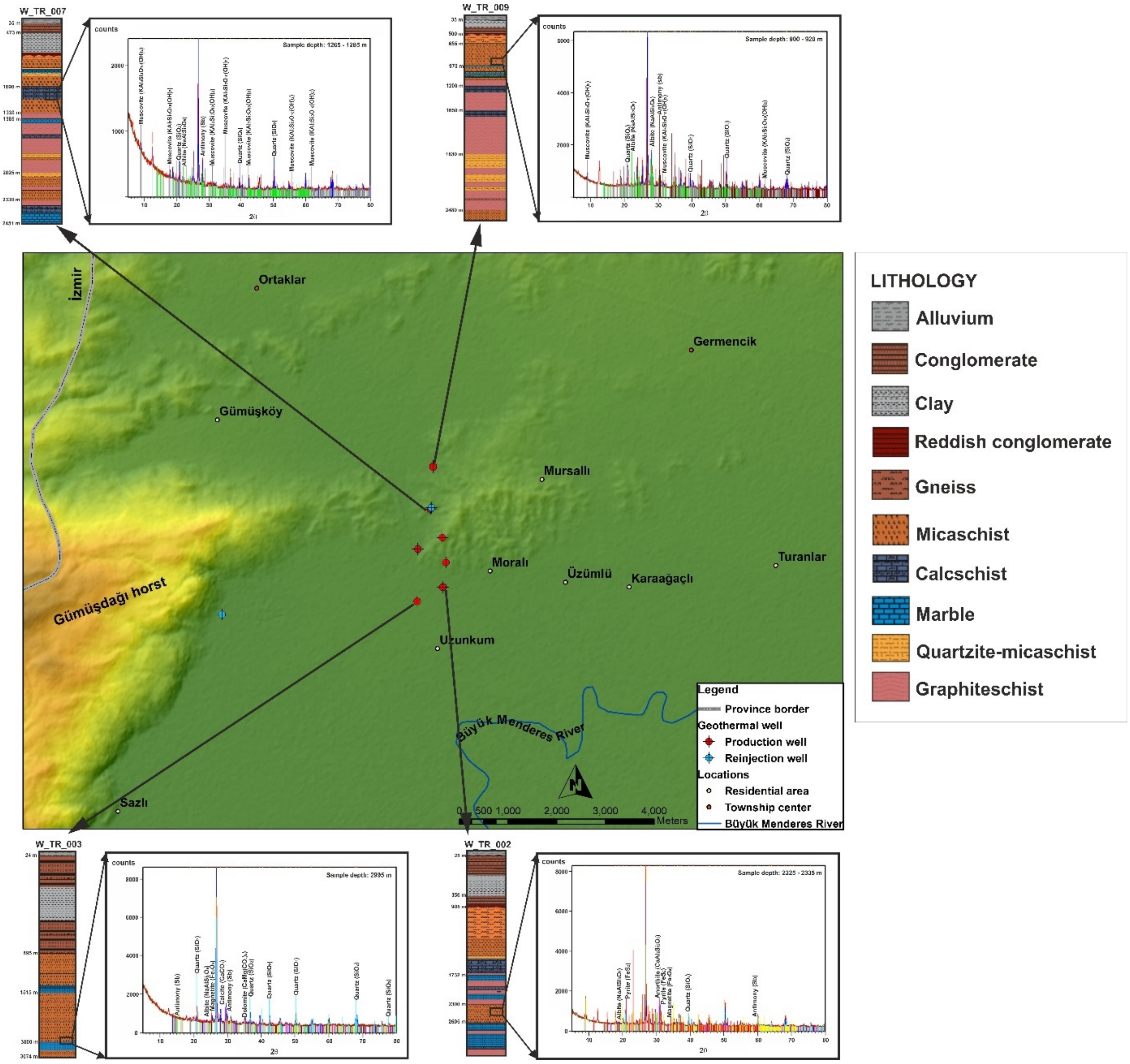

Figure 21: XRD results of the rock samples

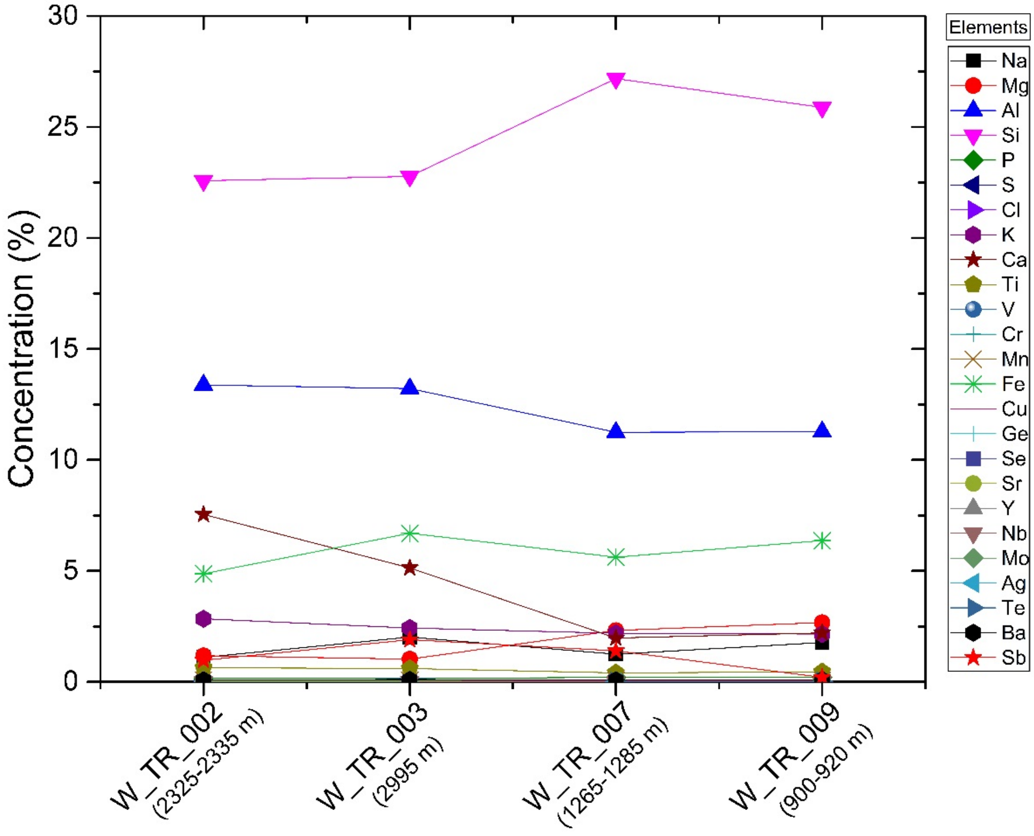

Figure 22: Elemental composition of rock samples in the well obtained by XRF as a function of depth of the collected samples. The rock samples were collected from the geothermal wells.

2.3.2.2 Scale sample in the preheater system

The Sb scale in the preheater system was subjected to elemental analysis using XRD, XRF and SEM. **Fig. 23** shows the photographic image of the Sb deposit in the preheater. The red color of the deposit, which is composed of a fine powder, is evident. The photographic image indicates the scale has reddish-orange amorphous stibnite. The thickness of the Sb deposit is between 1 and 4 mm (**Fig. 23**).

The diffractogram has a broad signal centered around 25° and a very broad reflection around 52°. XRD pattern shows amorphous particles, which means there is no crystalline reflection for stibnite (**Fig.24a**).

SEM analysis was also done to see the morphology of the scale. It shows heterogenous spherical colloids the size of which is 1.1 ± 0.5 µm (**Fig. 24b**). This type of morphology is quite similar to amorphous stibnite particles that have been reported previously many times in the literature (Çiftçi et al., 2020; Gill et al., 2013; Pan et al., 2009; Zakaznova-lakovleva et al., 2001).

The elemental composition of the scales shows that Sb and S are mostly observed at 56.57% and 21.87%, respectively (**Fig. 25**). These rates are compatible with stibnite stoichiometry in terms of the Sb/S ratio, which is 2.5. The Sb/S ratio varies depending on the sulphide concentration, and it is consistent with the ratios in the literature (Spycher and Reed, 1989; Zotov et al., 2003).

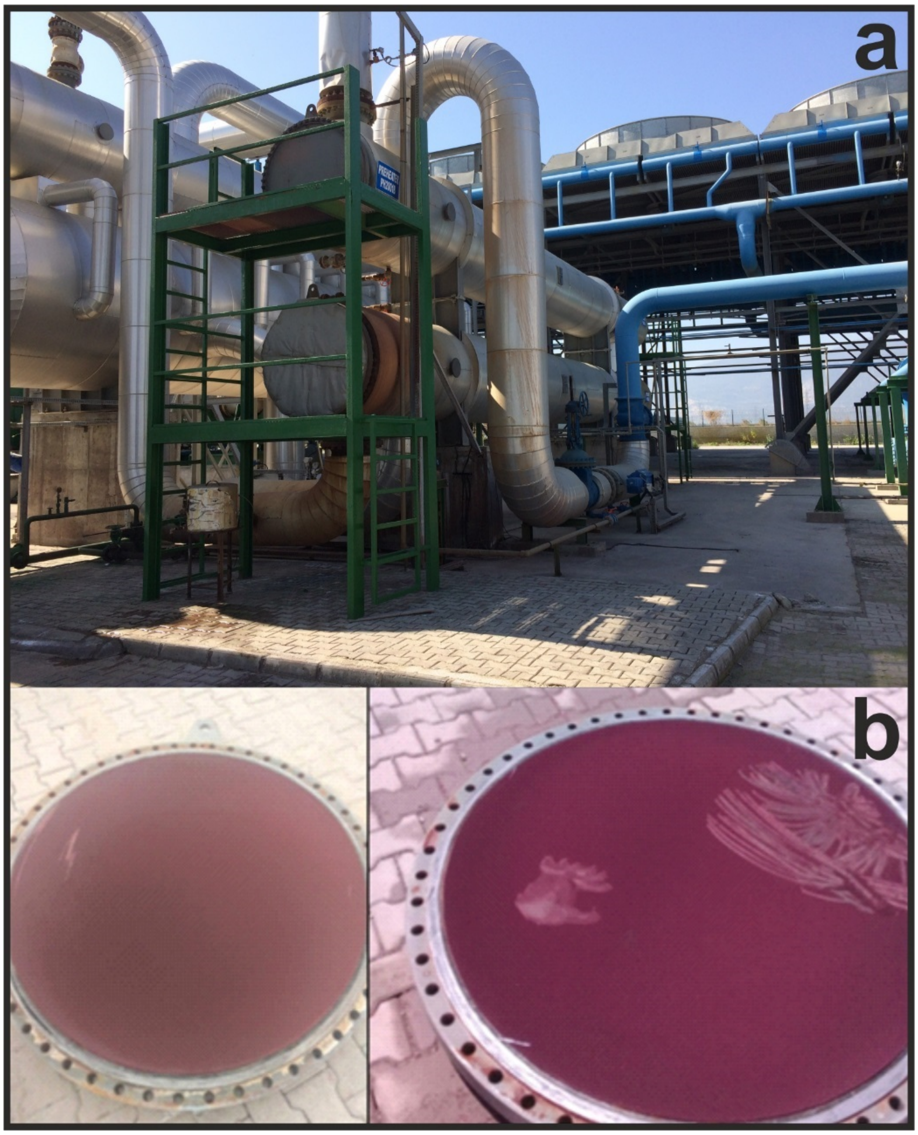

Figure 23 : Sb scale encountered at preheater in the ORC-binary system in the GGF

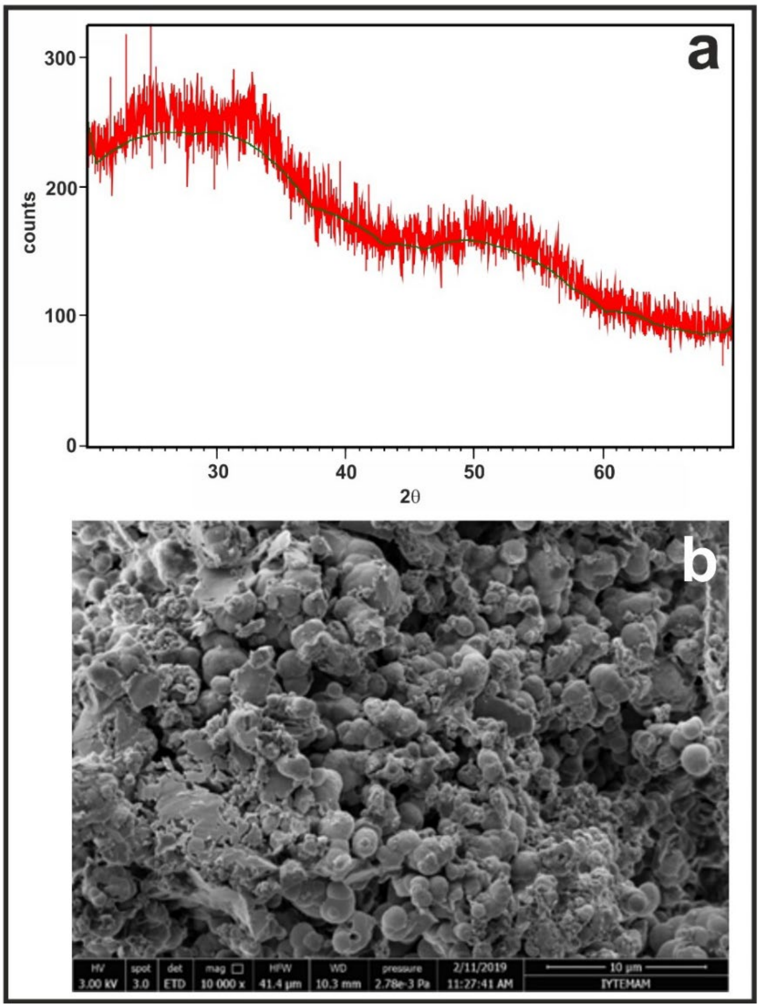

Figure 24: Evaluation of the Sb scale

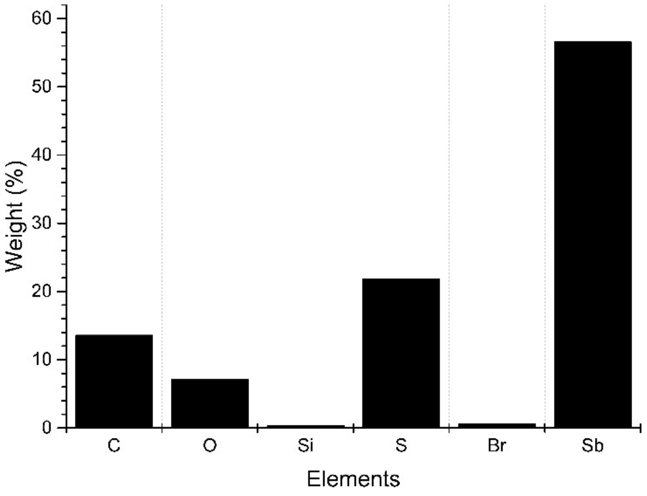

Figure 25: Elemental composition of the scale sample (as mass percentage)

2.3.3 Reservoir Temperatures of the GGF - Geothermometer Applications

The general purpose of geothermometers is to predict fluid temperature. As it is known, there are many different areas of use of hot water according to the temperature of the surface. The hot water in the deep reservoir cools considerably until it reaches the surface and mixes with cold groundwater in different proportions. It is clear that the temperature of the deep fluid will be much higher than the temperature at the surface. If the path of the geothermal waters is short and the flow rate is high, their temperature is close to the reservoir rock temperature. Therefore, estimating reservoir temperatures with geothermometer methods is an important part of geothermal studies. Some researchers have developed experimental geothermometers (Arnorsson, 2000; Arnorsson et al., 1983; Fournier, 1977; Fournier and Potter, 1979, 1982; Fournier and Truesdell, 1973; Fournier, 1992; Giggenbach, 1988; Fouillac and Michard, 1981; Kharaka et al., 1982; Kharaka and Mariner, 1989; Nieva and Nieva, 1987; Tonani, 1980; Truesdell, 1976).

Silica geothermometers

Silica geothermometers are widely used in determining reservoir temperature. These geothermometers give good results at temperatures between 150-225°C (Fournier, 1977). At higher temperatures, rapid silica precipitation can be observed in the hot fluid moving from the aquifer towards the surface. Therefore, the for reservoirs with temperature is above 225°C the silica geothermometer does not always reflect the real temperature in the geothermal water. Silica geothermometers are based on the temperature-dependent solubility of silica in water. Different geothermometer equations have been developed since the solubility of different silica forms such as quartz, cristobalite, chalcedony, and amorphous silica in water is different (**Appendix I**). For the calculated geothermometer calculations according to quartz geothermometers, silica solubility is controlled by chalcedony if the reservoir temperatures are between 120-180°C in volcanic environment (Arnorsson et al., 1983). If chalcedony geothermometers give a geothermal reservoir temperature between 100°C and 120°C, they can give the correct temperature value, but at temperatures below 100°C, the solubility of silica is controlled by amorphous silica. In this case, it is necessary to take into account the amorphous silica geothermometer values (Fournier, 1977).

Within the scope of the study, SiO_2 concentrations (as ppm) were obtained from the chemical analysis results evaluated in the GGF. SiO_2 concentrations are ranged from 125 to 165 ppm in the GGF. The reservoir rock temperatures calculated for the geothermal waters representing the geothermal aquifer with the silica geothermometer equations are presented in **Table 5**. As can be seen in **Table 5**, the reservoir temperatures calculated according to quartz-silica geothermometers vary between 130°C and 167°C.Consequently, quartz geothermometers likely reflect more accurate temperature values than other silica geothermometers (chalcedony). Equations 2 and 3 are more used for springs at sub-boiling temperatures, well discharges, and vigorously boiling springs (Fournier, 1977). Therefore, temperature values in equations 1 and 4 can be used for reservoir temperatures in the GGF.

Table 5: Reservoir temperatures (°C) calculated with silica geothermometers for the GGF

Location	**Well ID**	**Geothermometer Equations**										
		SiO_2 (ppm)	**1***	**2**	**3**	**4***	**5**	**6**	**7**	**8**	**9**	**10**
Germencik Geothermal Field (GGF)	**W_TR_001**	**125**	150	150	143	139	-	-	-	-	-	-
	W_TR_002	**145**	159	159	151	149	-	-	-	-	-	-
	W_TR_003	**140**	157	157	149	146	-	-	-	-	-	-
	W_TR_004	**155**	163	163	154	153	-	-	-	-	-	-
	W_TR_005	**150**	161	161	153	151	-	-	-	-	-	-
	W_TR_006	**145**	159	159	151	149	135	-	-	-	-	-
	W_TR_007	**165**	167	167	158	158	-	-	-	-	-	-
	W_TR_008	**165**	167	167	158	158	144	140	-	-	-	-
	W_TR_009	**165**	167	167	158	158	-	-	-	-	-	-
	W_TR_010	**140**	157	157	149	146	-	-	-	-	-	-
	W_TR_011	**135**	154	155	147	144	130	-	-	-	-	-

- : lower than or equal to the outflow temperature

* : reservoir temperatures calculated in the GGF (more accurate results)

Cation geothermometers

Cation geothermometers are geothermometers based on ion exchange. Ion exchange is a function of the reaction equilibrium constant (K), which depends on temperature. The ratio of ion-exchanged cation concentrations depends on the change of the equilibrium constant with temperature. Cation geothermometers give different reservoir temperatures, especially for hot water sources, due to processes such as the cold-water mixture and the water-rock interaction affecting the chemical composition of the fluid during the rise of hot water. The cation geothermometer relations proposed by various researchers are given in **Appendix II**.

Na/K geothermometers

Na/K geothermometers are based on cation exchange reactions between albite and K feldspars (Fournier, 1979). The cation exchange reaction is given Eq. 1.

$$NaAlSi_3O_8\ (\text{albite}) + K^+ \Leftrightarrow KAlSi_3O_8\ (\text{K-feldspar}) + Na^+ \quad (1)$$

The geothermal waters with high chloride content from high-temperature reservoirs (> 180°C) are suitable for this type of geothermometer. However, it can also be applied at low temperatures where geothermal water remains longer time in the reservoir. Since these geothermometers depend on the ratio of Na^+ and K^+, they are less affected by dilution and steam loss due to the cold-water mixture. Therefore, in systems with cold water mixtures, they give more accurate results than silica geothermometers (Fournier, 1979). The Na/K geothermometer results show that a reservoir temperature for geothermal fluid in the GGF ranges from 116 to 188°C (**Table 6**).

K-Mg geothermometer

The K-Mg geothermometer is applied in conditions where dissolved Na^+ and Ca^{2+} are not equilibrated between geothermal water and rock (Giggenbach, 1988). Unlike Na/K geothermometers, the K-Mg geothermometer is more affected by temperature and quickly re-equilibrated at lower temperatures. The relevant reaction is as follows;

$$0.8\text{K-mica} + 0.2\text{chloride} + 5.4\text{silica} + 2K^+ \Leftrightarrow 2.8\text{K-feldspar} + 1.6H_2O + Mg^{2+} \quad (2)$$

Temperature values calculated using these geothermometers are not included in the calculation as they give lower values than the outlet temperature.

Na-K-Mg geothermometer

The Na-K-Mg triangular diagram was proposed by Giggenbach (1988). This diagram consists of a combination of Na/K and K-Mg geothermometers. As can be seen from the Giggenbach diagram (**Fig. 26**), the geothermal waters in the GGF tend to approach the Na and K line. This is related to the Menderes Metamorphic Massif, including gneiss and schist units. These metamorphic rocks are enriched by feldspar minerals ($NaAlSi_3O_8$ and $KAlSi_3O_8$). According to the Giggenbach triangular diagram, it is seen that the geothermal waters in the GGF are in partial equilibrium with reservoir rocks (**Fig. 26**). Therefore, Na/K geothermometers can be applied to geothermal water samples of the GGF. The cation temperatures are shown in **Table 6** comply with the temperatures estimated by the Giggenbach diagram (**Fig. 26**). Giggenbach diagram suggests a deeper or longer circulation for the GGF.

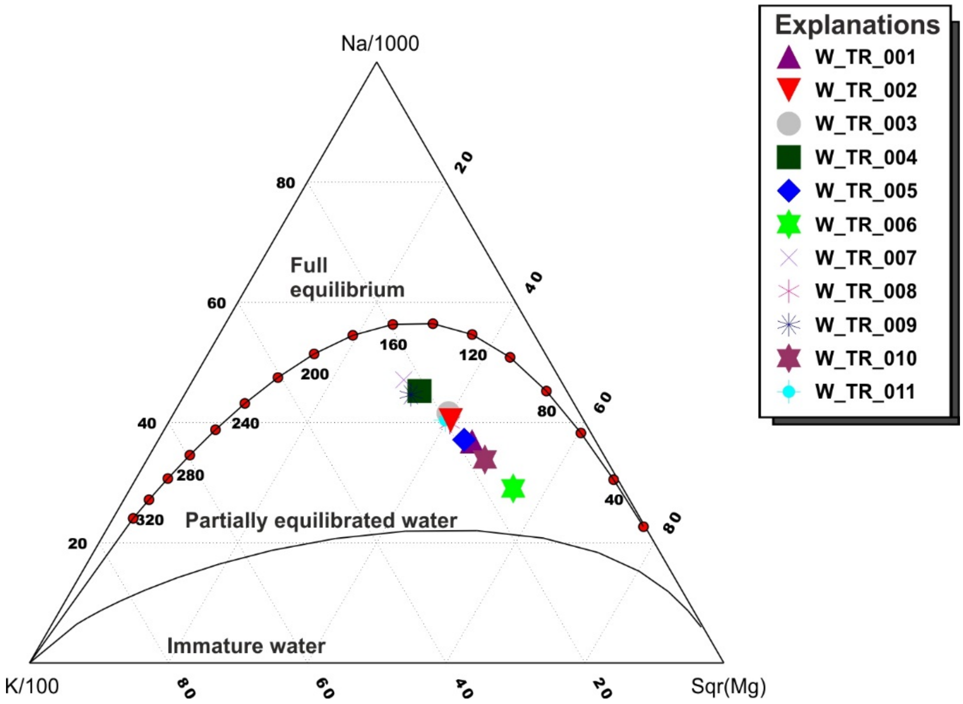

Figure 26: Distribution of water samples from the GGF in Na–K–Mg triangular diagram

Table 6: Reservoir temperatures (°C) calculated with cation geothermometers for the GGF

Location	Well ID	Geothermometer Equations										
		1	2	3	4	5	6	7	8	9	10	11
Germencik Geothermal Field (GGF)	W_TR_001	121	124	131	164	162	150	180	147	-	-	135
	W_TR_002	119	123	130	163	160	149	179	146	-	-	141
	W_TR_003	116	119	126	161	158	146	176	143	-	-	141
	W_TR_004	118	122	129	162	160	148	178	145	-	-	151
	W_TR_005	125	128	135	167	165	153	183	150	-	-	138
	W_TR_006	130	134	140	172	170	158	188	155	-	-	125
	W_TR_007	120	124	130	164	161	149	180	146	-	-	157
	W_TR_008	121	125	132	165	162	150	181	147	-	-	141
	W_TR_009	125	129	135	168	165	153	184	150	-	-	155
	W_TR_010	126	130	136	169	166	154	185	151	-	-	132
	W_TR_011	122	126	133	166	163	151	182	148	-	-	143

Other geothermometers could be also used: Na-K-Ca-Mg (Fournier and Potter, 1979) gives estimations of temperature ranging from 141 to 177°C for all the waters, Na-Li (Fouillac and Michard, 1979) gives estimations around 170°C.

Reservoir temperature modelling was made in the GGF using wells that have static temperature data. According to the numerical and block diagram obtained, the highest temperatures are in the north of the GGF (**Fig. 27a and Fig. 27b**). As seen in the numerical model, reservoir temperatures in the north of the geothermal field vary between 150°C and 200°C. These values comply with the reservoir temperatures obtained using geothermometer calculations.

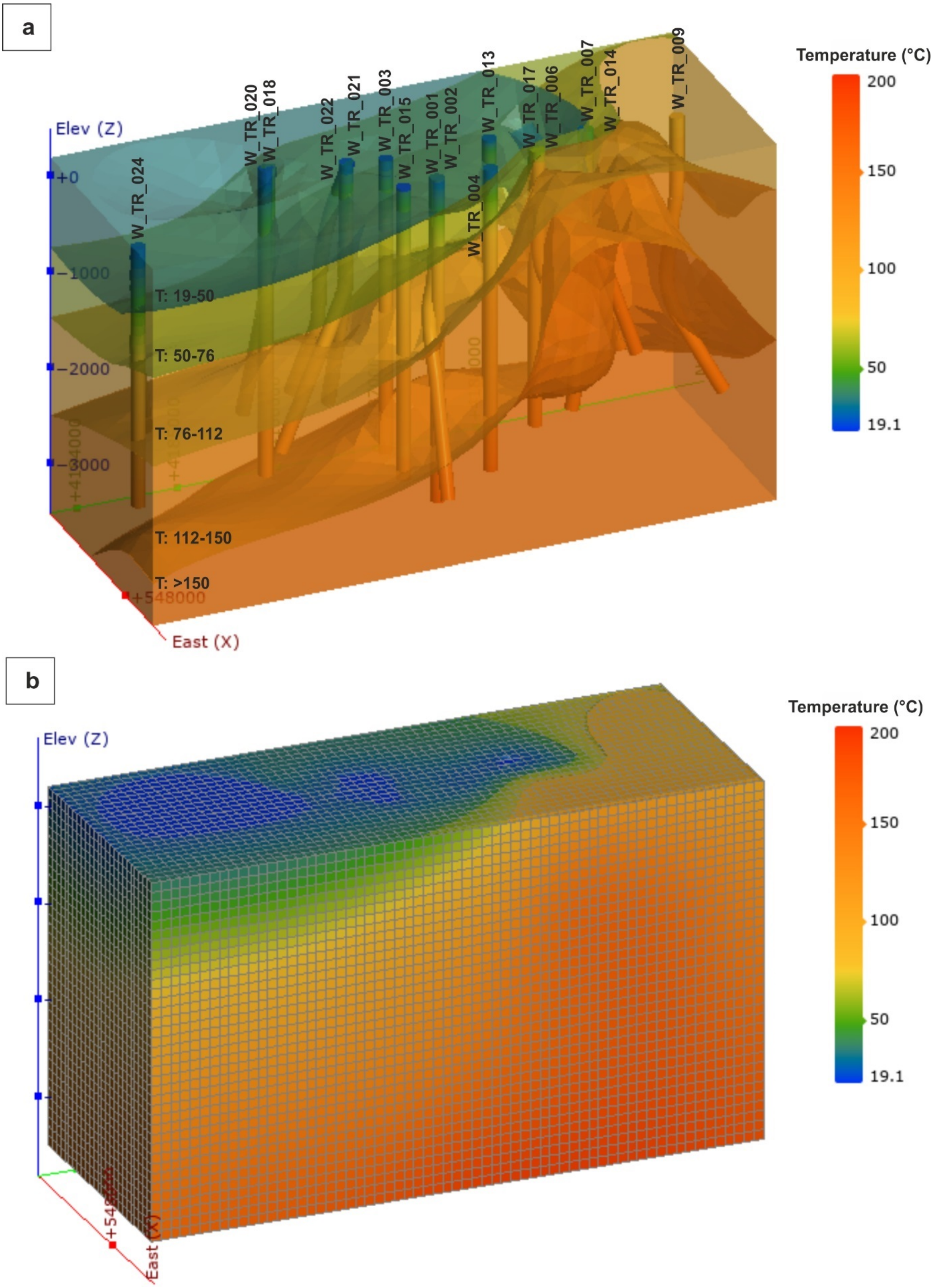

Figure 27 : Reservoir temperature modelling: a) Numeric model, b) Block model

2.3.4 Saturation indexes of the geothermal waters

Silica, calcite, and sulfide scaling are the most important problems of geothermal power plants, reducing power plant efficiency. The water-mineral equilibrium state of geothermal fluids changes with temperature and partly pressure for each mineral from the depth to the surface. The mineral equilibrium approach is based on the relation of calculating the saturation index for each temperature value and various minerals as a result of the chemical analysis of fluid. To interpret this chemical content gained by the geothermal fluids, the saturation states of geothermal fluids according to various minerals were evaluated using the PhreeqC and WATCH (Parkhurst and Appelo, 1999) software. Mineral equilibrium states in the geothermal fluid at 10 different temperature values were investigated in the PhreeqC and WATCH software. In PhreeqC, LLNL (The Lawrence Livermore National Laboratory) database was used, relying on the accuracy to be within ±0.5. The results are given in detail below.

2.3.4.1 Geothermal wells

For the GGF, saturation indexes were calculated at different temperatures from 20°C to 200°C using the chemical model PhreeqC for the geothermal fluids, where reservoir temperatures are less than 190°C. The geothermal fluids are supersaturated with quartz and chalcedony minerals in all wells below 140°C and 120°C, respectively (**Fig. 28**). Otherwise, geothermal fluids are under-saturated with amorphous silica above 40°C. However, as the temperature decreases (< 40°C), amorphous silica precipitation can be expected. The formation of silica forms in geothermal systems is strongly dependent on pH and temperature. Silica formation can also vary according to the amount of silica dissolved in the reservoir and the type of power plant (Brown, 2013; Demir et al., 2014; Utami, 2011, Zarrouk et al., 2014).

In terms of anhydrite ($CaSO_4$) mineral, the geothermal fluid is under-saturated at all temperatures. Therefore, there is no risk of anhydrite precipitation in geothermal wells. Geothermal fluids are supersaturated with respect to calcite at all temperatures. However, W_TR_001, W_TR_002, W_TR_009, and W_TR_010 are under-saturated below 100°C, 120°C, 120°C, 60°C, respectively. As the amount of CO_2 dissolved in the geothermal fluid increases, the amount of dissolved calcite increases. Therefore, as the geothermal fluid rises to the surface, the decrease in the amount of CO_2 will cause calcite precipitation with the decrease in pressure (Brown, 2013; Tarcan et al., 2016). It depends on controlling the degassing of CO_2.

From production depth to the flashing point, geothermal fluid flows as liquid phase. After flashing point, non-condensable gases (NCG's) are separated and multi-phase (NCG, steam, liquid) flow starts. After flashing, CO_2 is removed from the liquid phase and $CaCO_3$ precipitates. Therefore, the supersaturation depends on the pCO_2 conditions.

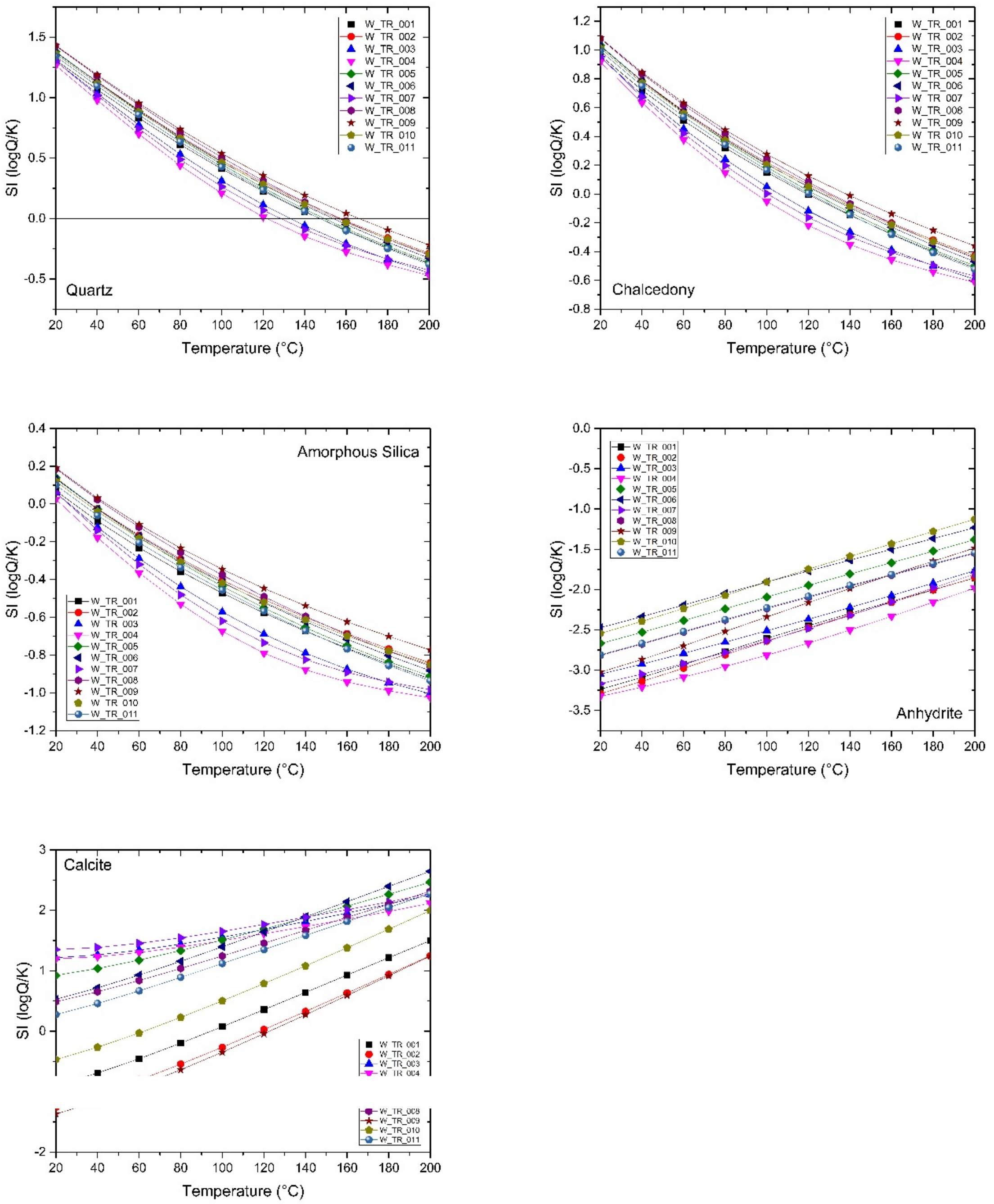

Figure 28: Mineral saturation-temperature diagrams for thermal waters in the GGF

2.3.4.2 Preheater system

For the preheater system in which stibnite scaling is observed, the saturation index model at the preheater in and the preheater out was implemented. The physical properties of the geothermal fluid vary from production to reinjection. In particular, the temperature of the geothermal fluid decreases from the production well until it reaches the power plant. The inlet temperature of the geothermal fluid in the preheater is 80°C, while the outlet temperature of the geothermal fluid in the preheater is 65°C. **Fig. 29** shows that the geothermal fluids are supersaturated with stibnite (Sb) minerals below 90°C in the preheater system. Wollastonite ($CaSiO_3$) and anhydrite ($CaSO_4$) are under saturated at all temperature values. Amorphous silica (SiO_2) and fluorite (CaF_2) in the preheater system are under saturated at all temperature values like wollastonite and anhydrite. Calcite ($CaCO_3$) solubility decreases with increasing temperature. Therefore, calcite scaling should not be expected in the low-temperature preheater system.

Considering the inlet and outlet temperatures of the preheater system, silica and calcite-based scaling should not be expected in the GGF.

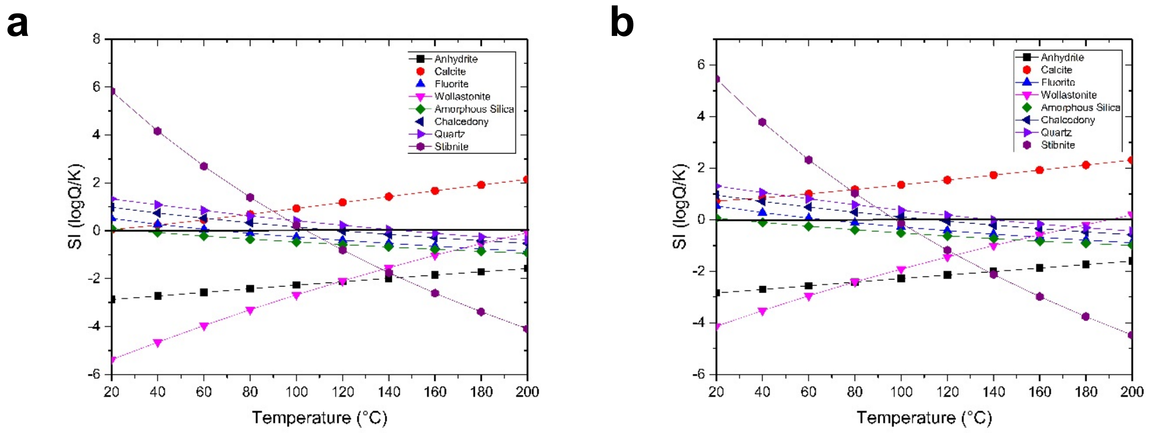

Figure 29: Mineral saturation-temperature diagrams for thermal waters in the GGF. a) Preheater in, b) Preheater out

2.3.5 Behaviour of stibnite in the geothermal waters

Knowledge of the speciation and thermodynamics of minerals in a geothermal fluid is crucial to the understanding and accurate modeling of the geothermal fluid. It is known that geothermal reservoir fluids often contain small concentrations of antimony. Antimony is found in sulphide deposits as stibnite, sulfosalts, and in some cases, natural Sb (Williams-Jones and Norman, 1997). In natural geothermal systems, antimony usually occurs in two oxidation states.

These are trisulphide, $Sb^{3+,}$ and pentasulphide, Sb^{5+} (White, 1967; Stauffer and Thompson, 1984).

Stibnite (Sb_2S_3), known as antimony trisulphide, is a sulphur mineral and is the main component of hydrothermal systems (Brown, 2011). In hydrothermal systems, stibnite precipitation is controlled by pH and temperature. For this reason, stibnite scaling is common in condensers, heat exchangers where the temperature and pH are low in binary cycle power plants. Although the concentration of antimony in the brine is low, antimony sulphide scaling is a major problem at low temperature and pH in binary cycle power plants. Typical antimony concentrations are less than 1 ppm in brine (Brown, 2011). However, studies have shown that antimony can be stored as stibnite in natural geothermal systems (Wilson et al., 2007).

In geothermal systems, stibnite dissolves in water in the form of hydroxide, and as the storage of stibnite increases, the hydrogen sulphide concentration increases. This situation can be expressed simply by the following equation;

$$Sb_2S_3 + 6H_2O = 2Sb(OH)_3 + 3H_2S \tag{3}$$

$$K = \frac{[Sb(OH)_3]^2[H_2S]^3}{[H_2O]^6[Sb_2S_3]} \tag{4}$$

Where K is the equilibrium constant

The fundamental criterion for chemical equilibrium in a thermodynamic system is that the total Gibbs free energy be at a minimum. At constant temperature and pressure, the Gibbs free energy change in a chemical reaction is given by:

$$\Delta G = \sum v_p\mu_p - \sum v_r\mu_r \tag{5}$$

Where both v_p and μ_r are chemical potentials for the product and reactant species, respectively, and v_p and v_r are the corresponding stoichiometric coefficients. The chemical potentials are given by,

$$\mu_p = \mu_p + RT \ln \alpha_p \tag{6}$$

$$\mu_r = \mu_r + RT \ln \alpha_r \tag{7}$$

where the superscript/indicates the standard state;

R is the gas constant; T is the absolute temperature; and. α_p and α_r are the activity of the product and reactant species, respectively. Substituting, we find that:

$$\Delta G = \Delta G + RT \sum \ln(a_i{}^{v_i}) = \Delta G + RT \ln \prod (a_i{}^{v_i}) \tag{8}$$

Where ΔG is the Standard Gibbs free energy of reaction, and the summation goes over all reactants and products; ν_i is positive for products and negative for reactants.

The ion activity product is defined by:

$$Q = \prod (a_i{}^{v_i}) = \frac{a_A{}^{v_A} a_B{}^{v_B} \ldots}{a_M{}^{v_M} a_N{}^{v_N} \ldots} \tag{9}$$

At equilibrium, ΔG = 0 and Q = K, where K is the equilibrium constant. For mineral-solute equilibrium, this constant is usually called the solubility product constant. Thus;

$$\Delta G = -RT \ln K + RT \ln Q = RT \ln \frac{Q}{K} \tag{10}$$

Where Q is the ion activity product for the mineral-water reaction, *K* is the equilibrium constant, R is the gas constant and T is the temperature.

We have undertaken a study of the simultaneous solubilities of stibnite in brine from 50 to 200°C in the presence of 18.19 ppm H_2S in the GGF to provide a thermodynamically consistent (Kaypakoğlu et al., 2015). In Germencik geothermal waters, the H_2S level in the gas phase is 0.21% (Haizlip et al., 2013). Stibnite concentrations ranged from 0.0009 to 1.23 ppm in brine. The molecular weight of H_2S is 34.1 g/mol. It has a density of 4.63 g/ml. The melting point is 550ºC. We assumed that the activity coefficient α, of H_2O is 1. The solubility of stibnite in a geothermal fluid is constant between 290°C and 320°C (Zakaznova-Iakovleva et al., 2001). Therefore, it took the temperature ranges between 50°C and 200°C in the geochemical model. Antimony (Sb) concentrations were evaluated to develop a predictive model for stibnite precipitation in the geothermal power plant. The aim of this was to obtain thermodynamic information on Sb speciation in different temperatures in order to be able to observe the behaviour of antimony in the hydrothermal system.

At 50°C and 90°C solubility of the stibnite is controlled by the thioantimonite, $HSb_2S_4^-$, $Sb_2S_4^-$. Hydroxothioantimonite species, $Sb(OH)_3$, $Sb(OH)_4^-$ become more dominant at 150°C and 200°C in the geothermal fluid. As the temperature and pH values decrease, the predominance of stibnite in the geothermal fluid increases. This means that stibnite precipitates at low temperatures and pH values. In the study area, the pH values of the geothermal fluid vary between 6.7 and 8.54. We know stibnite starts to precipitate below 90°C from saturation indexes modeling in the GGF. As can be seen in **Fig. 30**, at 90°C, thioantimonite species begin to dominate. Acidification occurs in the geothermal fluid due to the oxidation of hydrogen sulfide (H_2S) in this region. The red dashed ellipses were used to show the emergence of different stibnite species at low (50°C) and high temperatures (200°C). Acidification of the liquid causes a dramatic decrease in solubility and leads to stibnite precipitation. Therefore, in the dominant region of thioantimonite species (pink rectangle at 90°C), pH has a significant effect on stibnite solubility.

According to the model, in addition to the red amorphous stibnite (metastibnite) in the preheater system, different stibnite species may occur.

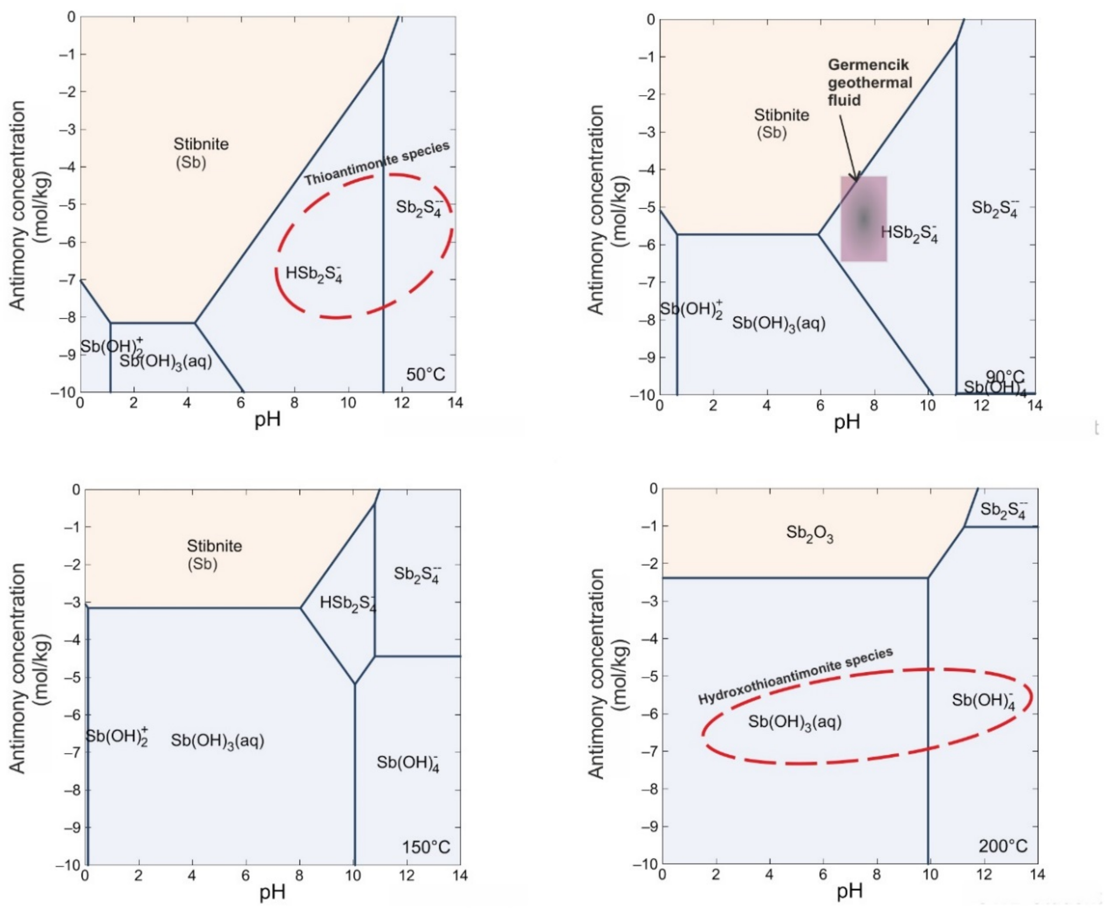

Figure 30: Stibnite species diagram in different temperature scales

2.4 DISCUSSION

2.4.1 Possible mineral precipitation tendencies in geothermal wells

It is interpreted that there is different mineral precipitation from production to reinjection at different temperatures in the GGF (**Fig. 31**). According to **Fig. 31**, calcite precipitation can be expected in the production wells. While the geothermal fluid flows from the reservoir through the entire system in the GGF, there is no risk in terms of amorphous silica precipitation between 95°C and 195°C. However, as the temperature decreases, amorphous silica precipitation can be expected. Therewithal, chalcedony, and quartz may precipitate below 135°C. No stibnite was detected in the production wells at the GGF.

2.4.2 Stibnite scaling in preheater system

From the speciation diagram of stibnite, it is seen that different stibnite forms can be formed together with metastibnite in the preheater system. According to the thermodynamic model, it is predicted that thioantimonite ($H_2Sb_2S_4$) species may be present in the system with the decrease in temperature and pH. Brown (2013) attributed the formation of thioantimonite stibnite species to the presence of H_2S in geothermal systems. The same author stated that increasing H_2S concentrations would lead to a decrease in pH, and with the rapid decrease in temperature, stibnite scaling will occur. The H_2S concentrations in the Germencik geothermal field are high compared to other geothermal fields in the BMG and are 0.21% (Haizlip et al., 2013). Also, Osborn et al. (2007) attributed the low pH of the geothermal waters in the GGF compared to other geothermal fields in the BMG to marbles.

In the GGF, stibnite formation starts at 90°C in the preheater system. The geothermal fluid enters the preheater system at 80°C and at this temperature, the geothermal fluid is supersaturated with respect to stibnite. (**Fig. 31**). **Fig. 31** shows that the calculated reinjection temperature is around 95°C to prevent stibnite scaling in the preheater system for the GGF.

The results obtained show that stibnite precipitates in low temperature and pH conditions, and these results are consistent with many studies in the literature. Wilson et al. (2007) stated that stibnite precipitation is the major problem at the Rotokawa and Ngawha power stations. It has been stated that pH and temperature change in Rotokawa and Ngawha plants is the main reason for stibnite precipitation in the preheater system. According to Wilson et al. (2007), the temperature lower than 100°C and pH < 8 provides optimum conditions for stibnite precipitation. In another study, Brown (2009) informed that temperatures lower than 90°C and pH < 9.7 are the best conditions for stibnite precipitation.

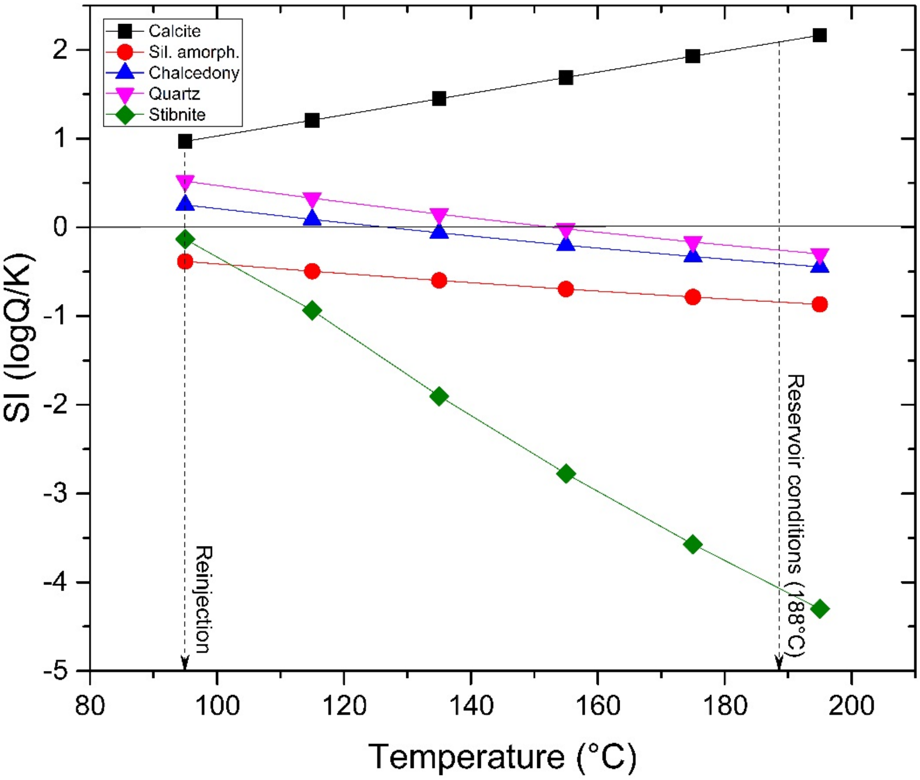

Figure 31: Critical mineral precipitation tendencies from production to reinjection in the GGF

2.5 CONCLUSION

In geothermal power plants, different types of scaling may occur in geothermal wells and surface equipment due to temperature, pH, and pressure changes in the geothermal fluid. The types of scaling vary according to the reservoir rocks and power plant type. Especially in the binary cycle power plants, the geothermal fluid entering the heat exchanger or preheater system directly after the production well causes the temperature of the fluid to drop rapidly. Heat exchanger and preheater systems of the binary cycle plant act as a sink, creating optimum conditions for stibnite scaling. Stibnite scaling causes efficiency and economic losses in the power plant by clogging the tubes of the heat exchanger. Therefore, determining the correct reinjection temperature is important in terms of scale formation.

Periodic mechanical cleaning is performed with high-pressure water jets, which is the most effective method to prevent stibnite scaling in the GGF. However, since this method requires the power plant to be completely shut down, it is very time-consuming and, at the same time, means loss of production. Although research and chemical companies are currently working on different chemical development studies for stibnite scaling, currently, the most suitable method appears to be to use inhibitors before preheater by dosing appropriately. Therefore, caustic (NaOH) dosing can be an alternative for this.

2.6 ONGOING STUDIES

Reflect partners from IZTECH are working on Tuzla and Germencik geothermal fields, which are located in the west of Turkey. Within the scope of the study, IZTECH partners will examine in detail the main problem of stibnite scaling in the Germencik geothermal field and silica scaling in the Tuzla geothermal field. In both fields, it is aimed to understand the processes of the hydrothermal fluid with the help of geochemical and conceptual models by determining the physical and chemical parameters of the fluid. So far, 11 water samples have been collected from the GGF, and a conceptual model has been created for the GGF, and other water analyses are ongoing. Samples were collected from 4 wells from Tuzla geothermal field, and conceptual model and water analysis evaluations are ongoing.

More detailed information about the ongoing studies is given in **Table 7**.

Table 7: Sampling dates, completed and ongoing studies for the Germencik and Tuzla fields.

Field Name	Sampling Date	Completed studies	Ongoing studies
Germencik Site Sampling Point: (9 production +2 reinjection)	17/06/2020	✓ Physical and chemical properties of the fluids ✓ Conceptual Model ✓ Isotopes analysis (^{18}O, ^{2}H and tritium) ✓ Saturation indexes modelling	
Germencik Site Sampling Point: (Preheater in, Preheater out 3 extra production wells)	24/02/2021		✓ Physical and chemical properties of the fluids in preheater and 3 extra wells ✓ Dissolved sulphate analysis for all wells ✓ ^{13}C-CO_2 analyses for all wells ✓ Reservoir temperature investigations ✓ Geochemical modelling for all wells

Tuzla site Sampling Point: (3 production + 1 reinjection)	22/09/2020	✓ Physical and chemical properties of the fluids	✓ Conceptual Model ✓ Isotopes analysis (^{18}O, ^{2}H and tritium) ✓ Saturation indexes modeling ✓ Geochemical modelling for all wells
Tuzla site Sampling Point: (3 production + 1 reinjection)	04/03/2021		✓ Dissolved sulphate analysis for all wells ✓ ^{13}C-CO_2 analyses for all wells ✓ Reservoir temperature investigations

2.7 REFERENCES

Aggarwal, J., Palmer, M., Bullen, T., Arnórsson, S., & Ragnarsdóttir, K. (2000). The boron isotope systematics of Icelandic geothermal waters: 1. Meteoric water charged systems. *Geochimica et Cosmochimica Acta, 64*(4), 579-585.

Arnórsson, S. (2000). Isotopic and chemical techniques in geothermal exploration, development and use. *International Atomic Energy Agency*, 109-111.

Arnorsson, S., Gunnlaugsson, E., & Svavarsson, H. (1983). The chemistry of geothermal waters in Iceland. III. Chemical geothermometry in geothermal investigations. *Geochimica et Cosmochimica Acta, 47*(3), 567-577.

Baba, A., Demir, M. M., Koç, G. A., & Tuğcu, C. (2015). Hydrogeological properties of hyper-saline geothermal brine and application of inhibiting siliceous scale via pH modification. *Geothermics, 53*, 406-412.

Baba, A., & Sözbilir, H. (2012). Source of arsenic-based on geological and hydrogeochemical properties of geothermal systems in Western Turkey. *Chemical Geology, 334*, 364-377.

Bertani, R. (2016). Geothermal power generation in the world 2010–2014 update report. *Geothermics, 60*, 31-43.

Bozkurt, E. (2000). Timing of extension on the Büyük Menderes Graben, western Turkey, and its tectonic implications. *Geological Society, London, Special Publications, 173*(1), 385-403.

Bozkurt, E. (2001). Neotectonics of Turkey–a synthesis. *Geodinamica acta, 14*(1-3), 3-30.

Brown, K. (2009). A report prepared for Geodynamics on antimony sulfide scaling. *Published by Geodynamics (http://www. ga. gov. au/image_cache/GA20053. pdf).*

Brown, K. (2011). *Antimony and arsenic sulfide scaling in geothermal binary plants.* Paper presented at the Proceedings International Workshop on Mineral Scaling.

Brown, K. (2013). *Mineral scaling in geothermal power production*: United Nations University Iceland.

Çelik, A., Topçu, G., Baba, A., Akdogan, Y., Şentürk, U., & Demir, M. M. (2017). Experimental modeling of silicate-based geothermal deposits. *Geothermics, 69*, 65-73.

Çiftçi, C., Karaburun, E., Tonkul, S., Baba, A., Demir, M. M., & Yeşilnacar, M. İ. (2020). Testing the Performance of Various Polymeric Antiscalants for Mitigation of Sb-Rich Precipitates Mimicking Stibnite-Based Geothermal Deposits. *Geofluids, 2020*.

Clark, I., & Fritz, P. (1997). Environmental Isotopes in Hydrology Lewis Publishers. *Boca Raton, New York*.

Dansgaard, W. (1964). Stable isotopes in precipitation. *Tellus, 16*(4), 436-468.

Demir, M. M., Baba, A., Atilla, V., & Inanlı, M. (2014). Types of the scaling in hyper saline geothermal system in northwest Turkey. *Geothermics, 50*, 1-9.

DiPippo, R. (2012). *Geothermal power plants: principles, applications, case studies and environmental impact*: Butterworth-Heinemann.

Emre, T., & Sözbilir, H. (1997). Field evidence for metamorphic core complex, detachment faulting and accommodation faults in the Gediz and Büyük Menderes grabens, western Anatolia. *Proceedings IESCA 1995, 1*, 73-94.

Faulds, J., Coolbaugh, M., Bouchot, V., Moek, I., & Oguz, K. (2010). *Characterizing structural controls of geothermal reservoirs in the Great Basin, USA, and Western Turkey: developing successful exploration strategies in extended terranes.* Paper presented at the World Geothermal Congress 2010.

Filiz, S., Tarcan, G., & Gemici, U. (2000). *Geochemistry of the Germencik geothermal fields, Turkey.* Paper presented at the Proceedings of the World Geothermal Congress.

Fournier, R. (1977). Chemical geothermometers and mixing models for geothermal systems. *Geothermics, 5*(1-4), 41-50.

Fournier, R., & Potter, I. (1982). Revised and expanded silica (quartz) geothermometer. *Bull., Geotherm. Resour. Counc.(Davis, Calif.);(United States), 11*(10).

Fournier, R., & Truesdell, A. (1973). An empirical Na☐K☐Ca geothermometer for natural waters. *Geochimica et Cosmochimica Acta, 37*(5), 1255-1275.

Fournier, R. O. (1992). Water geothermometers applied to geothermal energy. *Applications of geochemistry in geothermal reservoir development*, 37-69.

Fournier, R. O., & Potter Ii, R. (1979). Magnesium correction to the Na- K- Ca chemical geothermometer. *Geochimica et Cosmochimica Acta, 43*(9), 1543-1550.

Fouillac, C., and Michard, G. (1981): Sodium/Lithium ratio in water applied to geothermometry of geothermal reservoirs. *Geothermics*, 10, 55-70.

Gemici, Ü., & Tarcan, G. (2002). Distribution of boron in thermal waters of western Anatolia, Turkey, and examples of their environmental impacts. *Environmental Geology*, *43*(1-2), 87-98.

Giggenbach, W. F. (1988). Geothermal solute equilibria. derivation of Na-K-Mg-Ca geoindicators. *Geochimica et Cosmochimica Acta, 52*(12), 2749-2765.

Gill, J. S., Muller, L., & Rodman, D. (2013). Inhibition of antimony sulfide (stibnite) scale in geothermal fields. *GRC Transactions, 37*, 899-904.

Güner, N., & Yıldırım, N. (2005). *An example to the presence of paleo-seawater in geothermal fluids: Ömerbeyli–Germencik (Aydın) geothermal field. II.* Paper presented at the National Symposium on Applications of Isotopic Techniques in Hydrological Studies, İzmir, Turkey.

Haizlip, J. R., Haklidir, F. T., & Garg, S. K. (2013). *Comparison of reservoir conditions in high noncondensible gas geothermal systems.* Paper presented at the Proceedings.

Karakuş, H., & Şimşek, Ş. (2013). Tracing deep thermal water circulation systems in the E–W trending Büyük Menderes Graben, western Turkey. *Journal of Volcanology and Geothermal Research, 252*, 38-52.

Kaypakoglu, B., Aksoy, N., Serpen, U., & Sisman, M. (2015). *Stibnite scaling in a binary power plant in Turkey.* Paper presented at the Proceedings.

Kharaka, Y. K., Lico, M. S., & Law, L. M. (1982). Chemical geothermometers applied to formation waters, Gulf of Mexico and California basins. *AAPG Bulletin, 66*(5), 588-588.

Kharaka, Y. K., & Mariner, R. H. (1989). Chemical geothermometers and their application to formation waters from sedimentary basins *Thermal history of sedimentary basins* (pp. 99-117): Springer.

McKenzie, D. (1972). Active tectonics of the Mediterranean region. *Geophysical Journal International, 30*(2), 109-185.

Nieva, D., & Nieva, R. (1987). Developments in geothermal energy in Mexico—part twelve. A cationic geothermometer for prospecting of geothermal resources. *Heat recovery systems and CHP, 7*(3), 243-258.

Nicholson, K., 1993. Geothermal Fluids, Chemistry and Exploration Techniques Springer-. Verlag, Berlin, 263 p

Okay, A. (1989). Tectonic units and sutures in the Pontides, northern Turkey *Tectonic evolution of the Tethyan region* (pp. 109-116): Springer.

Osborn, W., Demirci, N., Gülgör, A., Erkan, B., & Yildirim, N. (2007). Carbonate scale inhibition in a high-gas geothermal well, Germencik, Turkey. *Geothermal Resources Council Transactions, 31.*

Özgür, N., Graf, W., Stichler, W., Wolf, M., (2004). Origin of the high sulfate contents in thermal waters of Kızıldere and environs, Western Anatolia, Turkey. International Symposium on Eastern Mediterranean Geology, Thessaloniki, Greece 1306–1309.

Pan, J., Xiong, S., Xi, B., Li, J., Li, J., Zhou, H., & Qian, Y. (2009). Tartatric Acid and L-Cysteine Synergistic-Assisted Synthesis of Antimony Trisulfide Hierarchical Structures in Aqueous Solution: Wiley Online Library.

Parkhurst, D. L., & Appelo, C. (1999). User's guide to PHREEQC (Version 2): A computer program for speciation, batch-reaction, one-dimensional transport, and inverse geochemical calculations. *Water-resources investigations report, 99*(4259), 312.

Seyitoğlu, G., & Scott, B. C. (1992). The age of the Büyük Menderes graben (west Turkey) and its tectonic implications. *Geological Magazine, 129*(2), 239-242.

Simsek, S. (2003). Hydrogeological and isotopic survey of geothermal fields in the Buyuk Menderes graben, Turkey. *Geothermics, 32*(4-6), 669-678.

Sözbilir, H. (2001). Nazilli ve dolayının (Büyük Menderes Grabeni) genç-tektoniği. *Büyük Menderes Depremleri Jeofizik Toplantısı*, 54-61.

Sözbilir, H., & Emre, T. (1990). *Neogene stratigraphy and structure of the northern rim of the Büyük Menderes graben.* Paper presented at the Proceedings of International Earth Science Colloquium on the Aegean Region.

Spycher, N. F., & Reed, M. H. (1989). As (III) and Sb (III) sulfide complexes: an evaluation of stoichiometry and stability from existing experimental data. *Geochimica et Cosmochimica Acta, 53*(9), 2185-2194.

Stauffer, R. E., & Thompson, J. M. (1984). Arsenic and antimony in geothermal waters of Yellowstone National Park, Wyoming, USA. *Geochimica et Cosmochimica Acta, 48*(12), 2547-2561.

Tarcan, G., Özen, T., Gemici, Ü., Çolak, M., & Karamanderesi, İ. H. (2016). Geochemical assessment of mineral scaling in Kızıldere geothermal field, Turkey. *Environmental Earth Sciences, 75*(19), 1-19.

Tezcan, A. (1979). Geothermal studies, their present status and contribution to heat flow contouring in Turkey *Terrestrial heat flow in Europe* (pp. 283-292): Springer.

Tokçaer, M. (2007). *Geochemical cycle of boron and isotope fractionation in geothermal fluids of Western Anatolia* (Doctoral dissertation, Dissertation, Dokuz Eylül University).

Tonani, F. (1980). Some remarks on the application of geochemical techniques in geothermal exploration *Advances in European Geothermal Research* (pp. 428-443): Springer.

Truesdell, A. (1976). *Summary of section III-geochemical techniques in exploration.* Paper presented at the Proc. 2nd UN Symp. on the Development and Use of Geothermal Resources.

Tureyen, O., Gulgor, A., Erkan, B., & Satman, A. (2016). *Recent expansions of power plants in Figuris concession in the Germencik geothermal field, Turkey.* Paper presented at the Proceedings.

Utami, P. (2011). *Hydrothermal alteration and the evolution of the Lahendong geothermal system, North Sulawesi, Indonesia.* ResearchSpace@ Auckland.

Vengosh, A., Helvacı, C., & Karamanderesi, I. H. (2002). Geochemical constraints for the origin of thermal waters from western Turkey. *Applied Geochemistry*, *17*(3), 163-183.

White, D. E. (1967). Mercury and base-metal deposits with associated thermal and mineral waters. *Geochemistry of hydrothermal ore deposits*, 575-631.

Wikipedia, https://en.wikipedia.org/wiki/Geology_of_the_Alps#/media/File:Tectonic_map_Mediterranean_EN.svg

Williams-Jones, A. E., & Norman, C. (1997). Controls of mineral parageneses in the system Fe-Sb-SO. *Economic Geology, 92*(3), 308-324.

Wilson, N., Webster-Brown, J., & Brown, K. (2007). Controls on stibnite precipitation at two New Zealand geothermal power stations. *Geothermics, 36*(4), 330-347.

Yamanlar, S., Korkmaz, E. D., & Serpen, U. (2020). Assessment of geothermal power potential in Buyuk Menderes Basin, Turkey. *Geothermics, 88*, 101912.

Yildirim, N., & Yildirim, A. (2015). *High total inorganic carbon concentration dependent carbonate scaling and mitigation system in moderate to high enthalpy geothermal fields in Turkey.* Paper presented at the Proceedings of the World Geothermal Congress.

Zakaznova-Iakovleva, V., Migdisov, A. A., Zakaznova-Iakovlevaa, V., Migdisov, A. A., Suleimenov, O., Williams-Jones, A., & Alekhin, Y. V. (2001). An experimental study of stibnite solubility in gaseous hydrogen sulphide from 200 to 320 C. *Geochimica et Cosmochimica Acta, 65*(2), 289-298.

Zarrouk, S. J., Woodhurst, B. C., & Morris, C. (2014). Silica scaling in geothermal heat exchangers and its impact on pressure drop and performance: Wairakei binary plant, New Zealand. *Geothermics, 51*, 445-459.

Zotov, A., Shikina, N., & Akinfiev, N. (2003). Thermodynamic properties of the Sb (III) hydroxide complex Sb (OH) 3 (aq) at hydrothermal conditions. *Geochimica et Cosmochimica Acta, 67*(10), 1821-1836.

3 DEEP FLUIDS FROM THE BOUILLANTE HIGH-TEMPERATURE GEOTHERMAL FIELD (FRENCH WEST INDIES)

Even though the first exploration works have been carried out in the 1970s in the French West Indies territories, the Bouillante geothermal power plant in Guadeloupe is the lone example of this type of power plant in the Caribbean area since 1986 (Fig. 32).

The Bouillante geothermal plant, which exploits about 650 tons/h of hot fluid ($T_{res.}$ close to 260°C) from two deep deviated wells BO-5 and BO-6 (about 1000 m deep; Fig. 33) and produces about 20% of steam, since 2005, is constituted of two production units (Fig. 34), representing a total capacity of 15 MWe. Its present annual production is close to 110 GWh (about 5-6% of the island's electricity needs). For the moment and since 2015, the water reinjection is partial, and the majority of the produced fluid is discharged in the sea, after mixing and cooling with seawater and without important environmental impact.

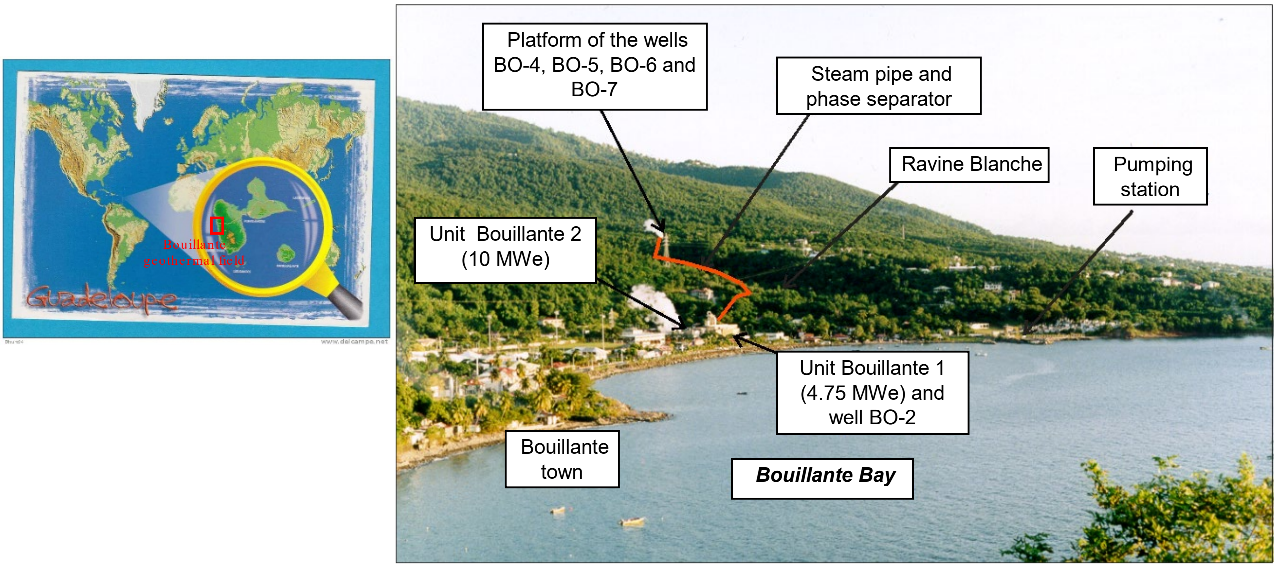

Figure 32: Global view of the Bouillante geothermal power plant in Guadeloupe.

The history of this power plant is summarized in Figure 35. Exploited between 1995 and 2016 by the Géothermie Bouillante (GB) Company, a subsidiary of BRGM and EDF (literally Electricity of France), the Ormat Company has become the majority owner and operator of this power plant since 2016 (GB-Ormat). In 2009, a 50 year-concession, covering a large part of the Bouillante commune territory and integrating these areas, was granted by this company.

Numerous studies of geothermal exploration, reservoir modelling and field monitoring were carried out by BRGM between 1995 and 2016 within the framework of co-funded projects with ADEME (French Agency for Ecological Transition), European Union, and Guadeloupe Regional council.

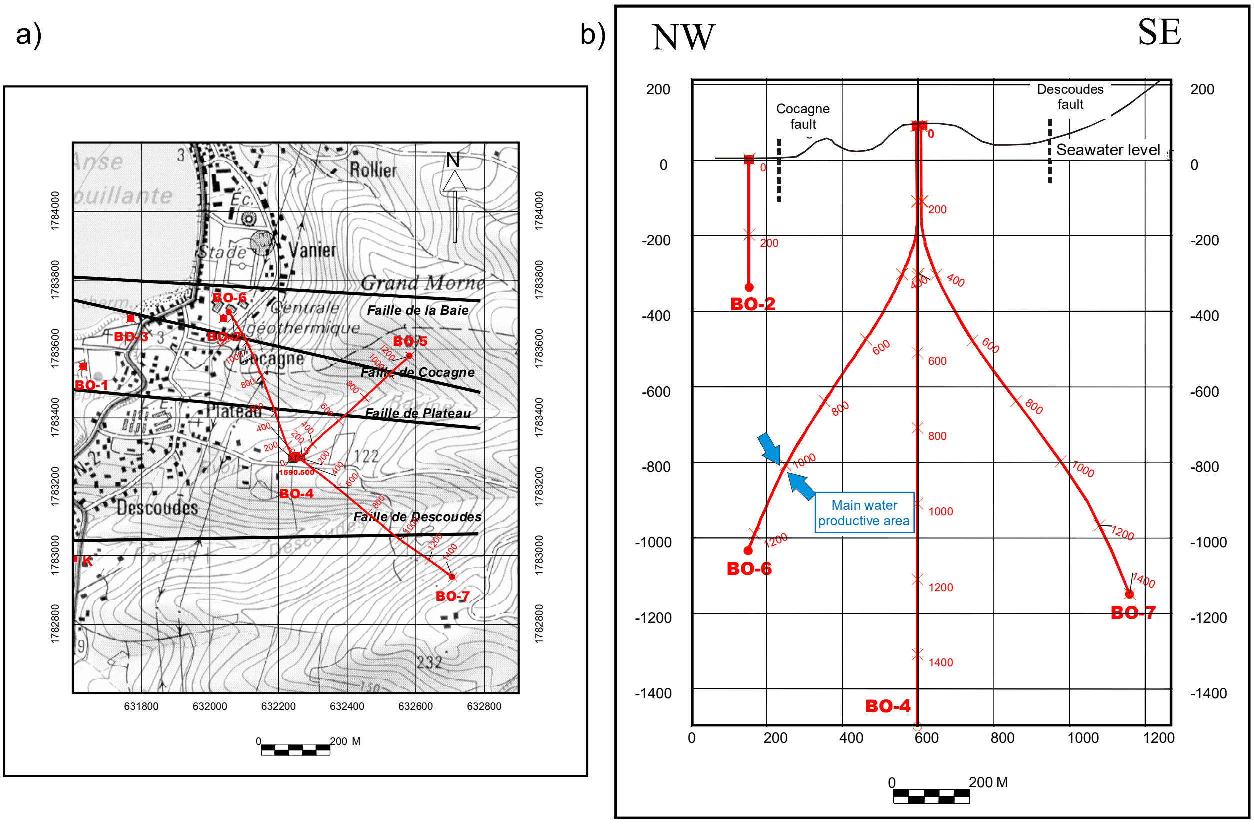

Figure 33: a) Location map of the Bouillante geothermal wells and main faults. Projection at surface of the deviated wells BO-5, BO-6 and BO-7. b) Vertical NW-SE cross-section showing the vertical wells BO-2 and BO-4 and the deviated wells BO-6 and BO-7. BO-5 is in a perpendicular plan (figures from CFG).

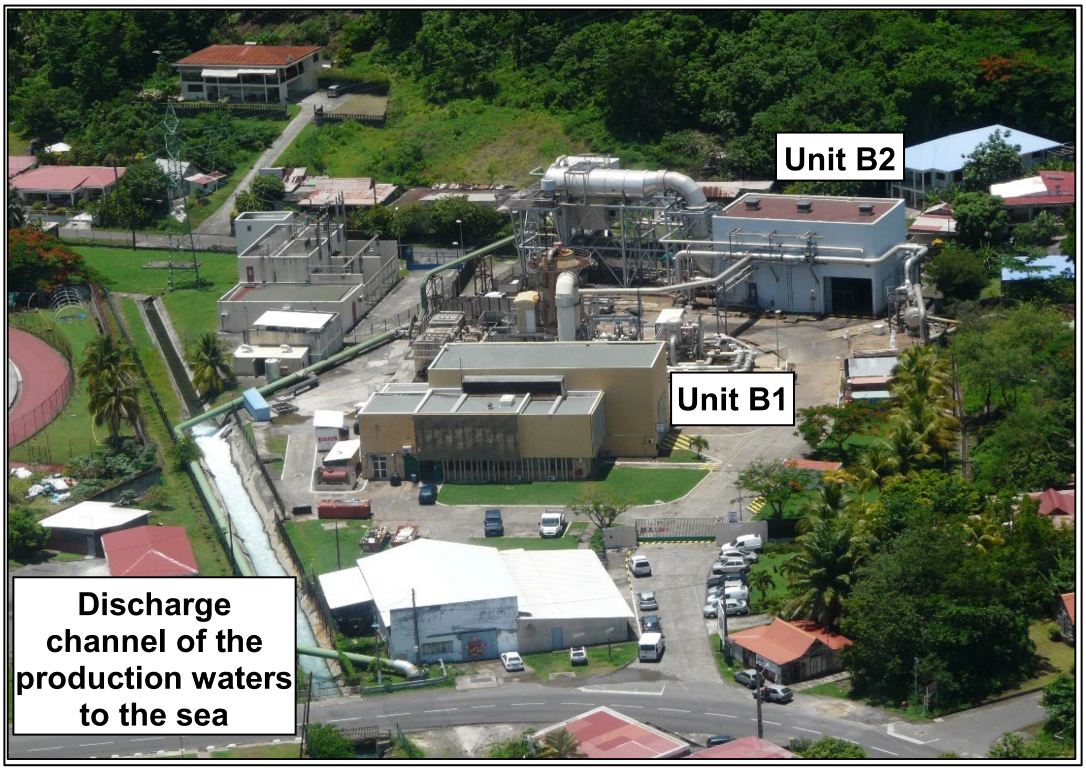

Figure 34: The two production units of the Bouillante geothermal power plant.

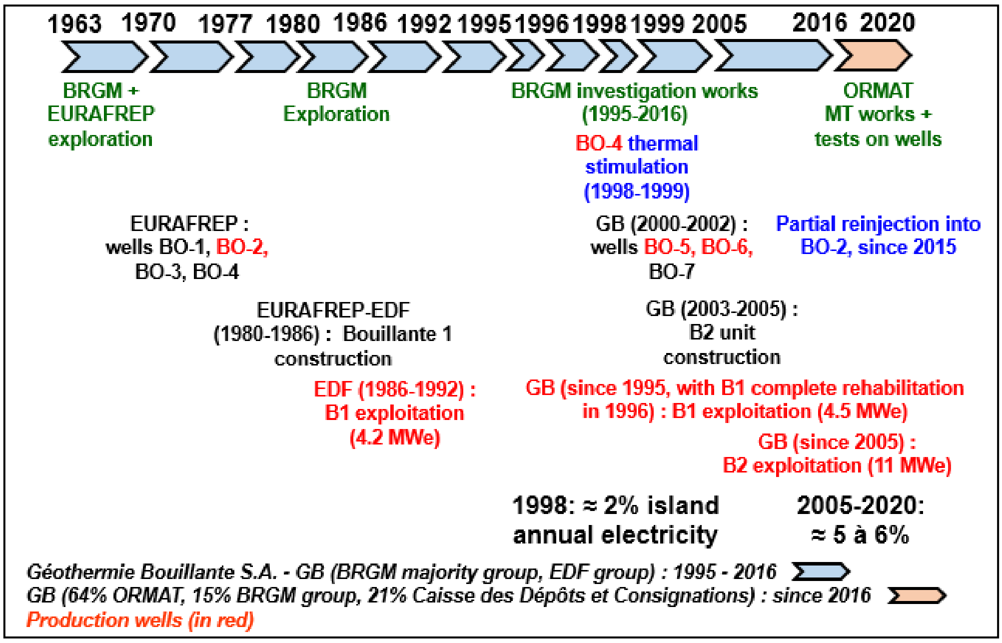

Figure 35: History of the Bouillante geothermal power plant.

About 20 scientific international papers, 60 technical reports, 60 participations to congresses and 5 PhD theses were carried out between 1996 and 2016 within the framework of these research projects. Among these works, the geochemical monitoring of the fluids discharged from the Bouillante geothermal wells and from the thermal manifestations located near the power plant was conducted by BRGM.

The major objectives of this chapter are to summarise the main geochemical characteristics of the deep fluids discharged from the Bouillante geothermal wells acquired during this monitoring and compare them with the analytical results of a water sample collected from the BO-6 wellhead in January 2021 in order to observe the evolution of the chemical composition of the deep geothermal water during its exploitation and take it into account for the works of geochemical modelling foreseen in the REFLECT project.

3.1 BOUILLANTE GEOTHERMAL FIELD

The success story of the current Bouillante geothermal field development is due to several factors. Its geographical position close to the sea, its geological location between two major tectonic accidents (Fig. 36), the presence of surface hydrothermal manifestations and the relatively low depth of the geothermal reservoirs have probably favoured its discovery and its development.

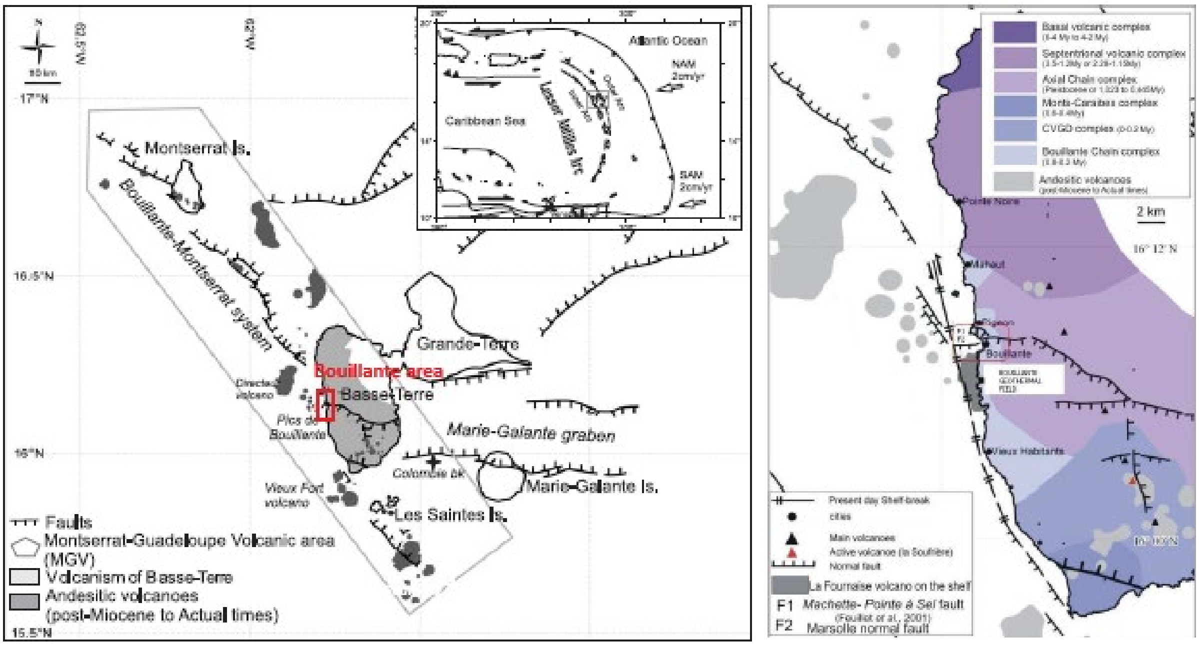

Figure 36: Maps of regional and local tectonic settings of the Bouillante field, and associated volcanism (Thinon et al., 2010, and Feuillet et al., 2001, 2002). Left: Regional structural sketch of the Montserrat-Bouillante-Les Saintes and Marie-Galante tectonic systems. Right: Location of the Bouillante geothermal field (western Basse-Terre) at the intersection of the NNW-SSE Montserrat-Bouillante-Les Saintes strike-slip system and the Marie-Galante graben system.

However, the research projects aiming at stimulating, supporting and developing the exploitation of the geothermal field have also been a key parameter of this success and crucial for its future development. The thermal stimulation of a former well with high amounts of cold seawater (Correia et al., 2000). The geological, geochemical, geophysical, and hydrogeological works for geothermal exploration and the tests of innovative methods carried out between 1996 and 2005 (Traineau et al., 1997; Sanjuan, 2001; Sanjuan et al., 2004; 2005; Truffert et al., 2004; Fabriol et al., 2005), have contributed to increasing from 2 to 6% the percentage of Guadeloupe's annual electricity production in 2005 (Fig. 35).

The drilling of three new wells (BO-5, BO-6 and BO-7; Fig. 33 and Fig. 37) and the creation of a 3D-geological model have allowed a better knowledge of the Bouillante geothermal reservoir in terms of geology (Fig. 38), mineralogy (Fig. 39a), temperature (Fig. 39b), and volume (Fig. 39c).

These studies have also highlighted new promising areas for geothermal production, such as the north of the Bouillante Bay (Pointe à Lézard, Bouillante 3) and the Anse Thomas area, at the south of Bouillante Bay (Fig. 40). Within the current state of knowledge, the geothermal developments could potentially represent about 40 to 50 MWe installed, covering more than 20% of the electricity consumption of this island.

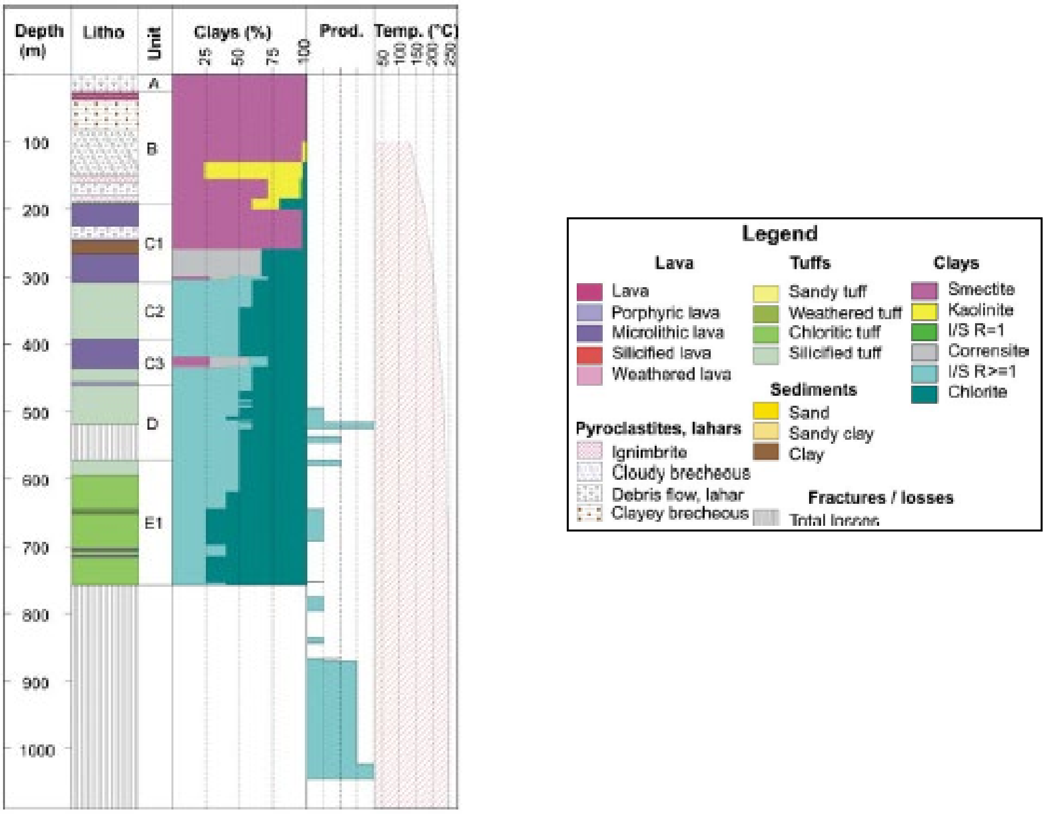

Figure 37: Example of the main data obtained from well BO-5 (from Lachassagne *et al.*, 2009, and Sanjuan et al., 2004). The productivity (Prod.) scale is relative, based on mud losses observed during drilling. I/S R=1: R1-ordered interstratified illite/smectite, with 50 to 70% Illite. I/S R>1:R2 or R3-ordered interstratified illite/smectite, with 80% or more of illite.

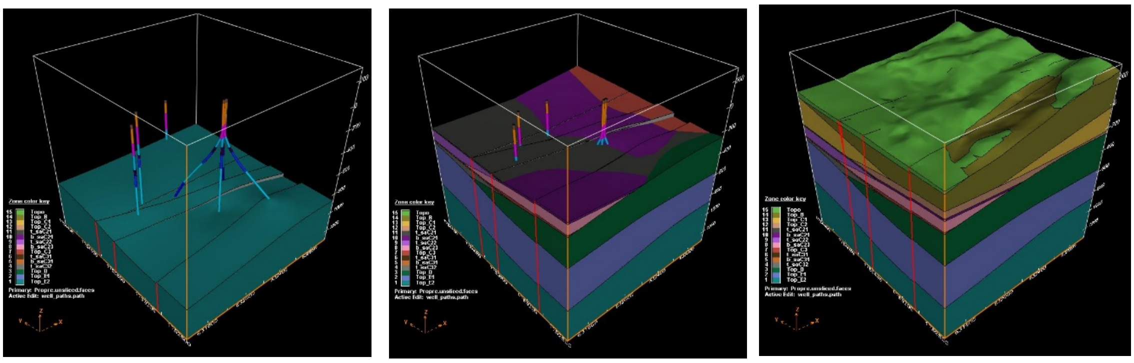

Figure 38: Superposed views of the different lithological units in the 3D-geological model of the currently exploited Bouillante geothermal reservoir, using the EarthVision® software (Dynamic Graphics) (from Sanjuan et al., 2004).

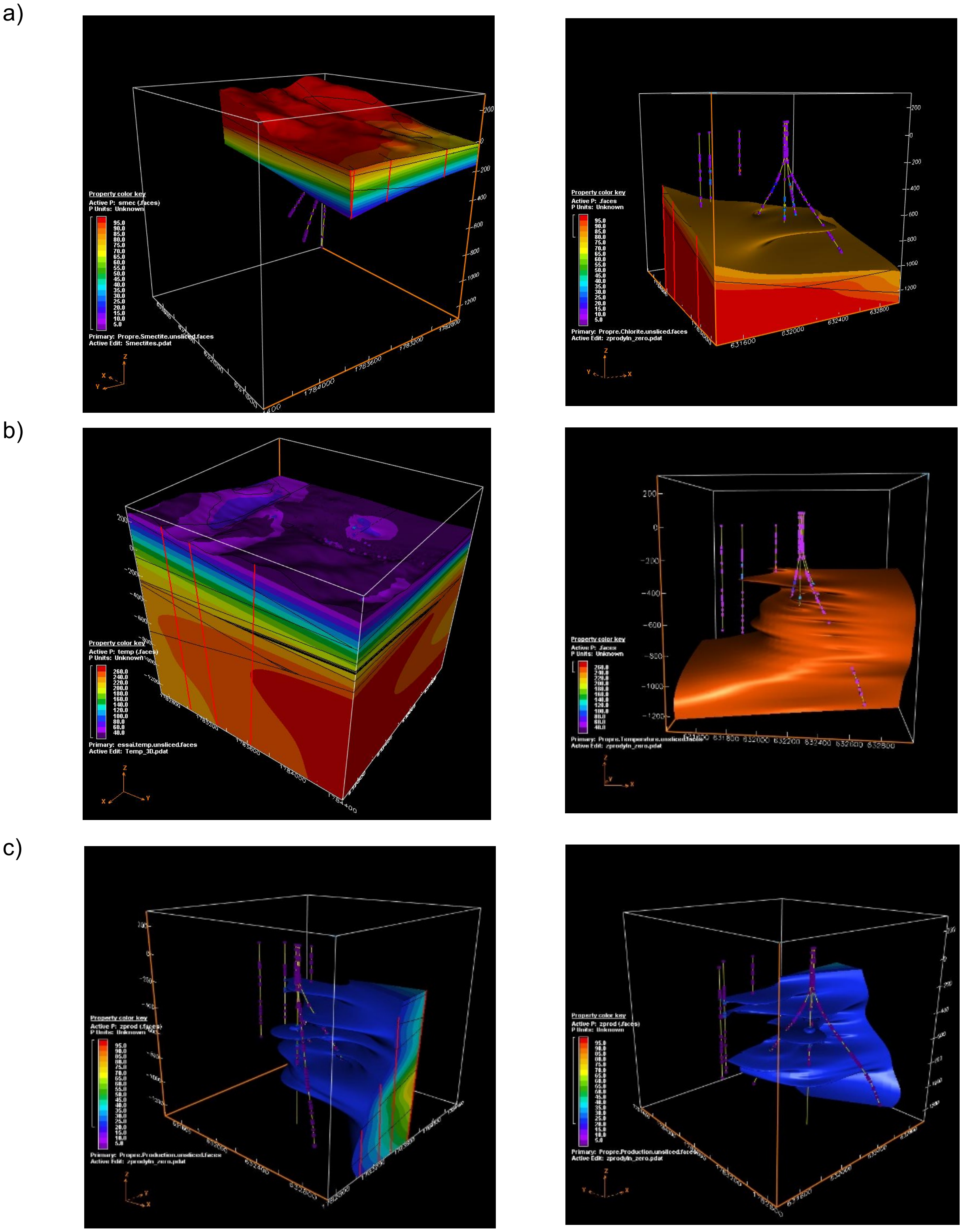

Figure 39: 3D-geological model of the currently exploited Bouillante geothermal reservoir, using the EarthVision® software (Dynamic Graphics): a) Mineralogical distribution of the clays: smectite amounts in the left picture and chlorite amounts in the right picture. b) Temperature repartition. c) Reservoir water volume (from Sanjuan et al., 2004).

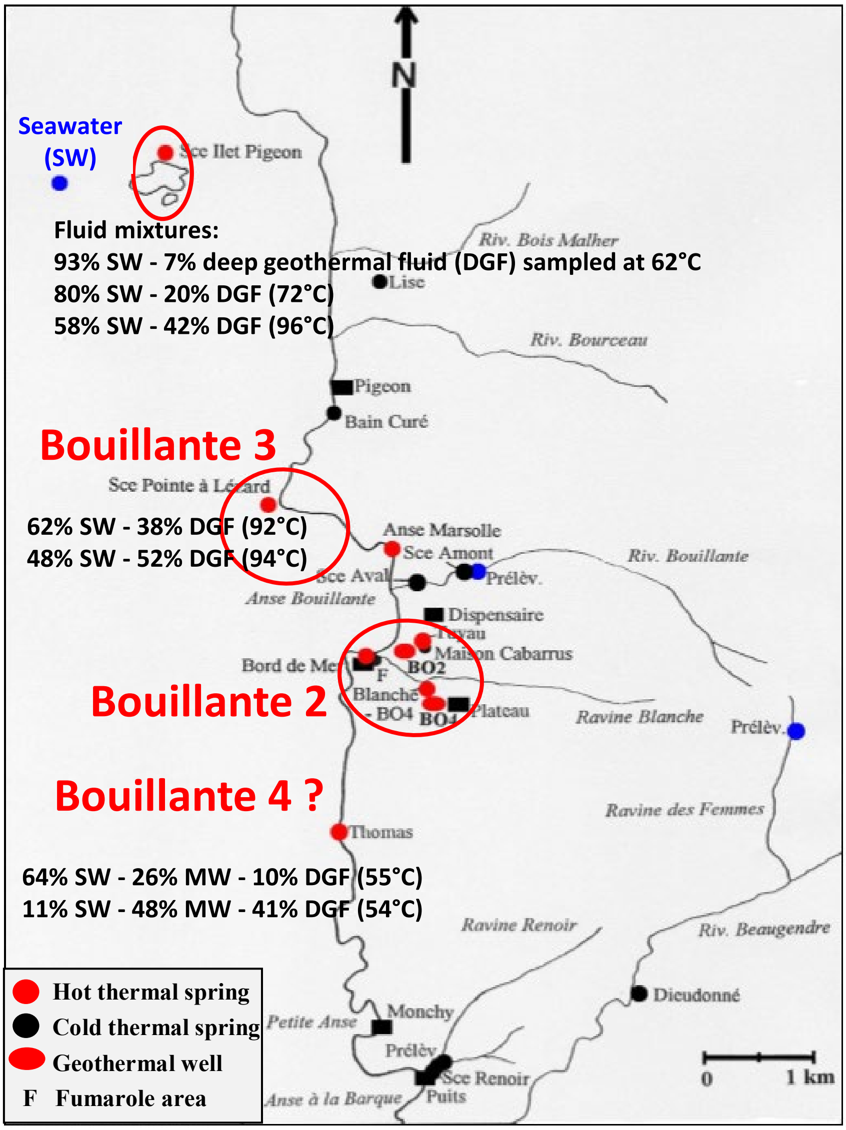

Figure 40: Main zones of deep geothermal water outflows in the Bouillante area and estimations of the proportions of seawater and deep geothermal water using chemical data (adapted from Sanjuan, 2001).

The further research works carried out by BRGM (development of exploration methods adapted to these territories, of reservoir modelling and monitoring) have contributed to better knowing this field and understanding how it works (Lachassagne et al., 2009; Sanjuan et al., 2010; 2013; Bouchot et al., 2010; Millot et al., 2010; Calcagno et al., 2011; Verati et al., 2014; Gailler et al., 2014; Sanjuan and Brach, 2015; Traineau et al., 2015; Hamm et al., 2016). They have also confirmed the interest of the new promising areas.

Bouchot et al. (2010) have proposed a conceptual model of the Bouillante geothermal system based on multidisciplinary borehole and surface exploration data (Fig. 41). Calcagno et al. (2011) have performed a 3D-geological model of this system (Fig. 42). The latter could have started 300’000 years ago, as suggested by several adularia samples collected from the Marsolle hydrothermal breccia (Verati et al., 2014) and by the relatively recent volcanism of the Bouillante chain (0.5 - 0.8 My). A synthetic map of the current global knowledge of the Bouillante geothermal system is reported in Figure 43 (Traineau et al., 2015).

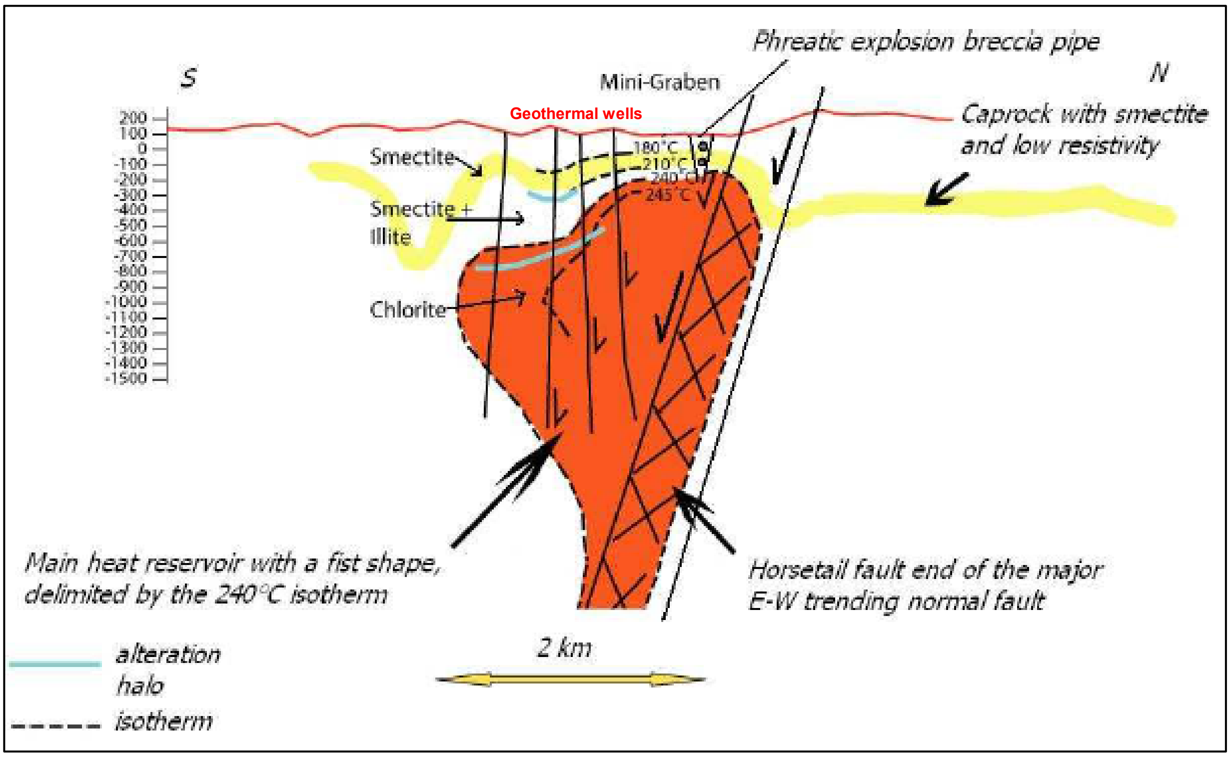

Figure 41: Conceptual model along a N-S section of the Bouillante geothermal system (from Bouchot et al., 2010).

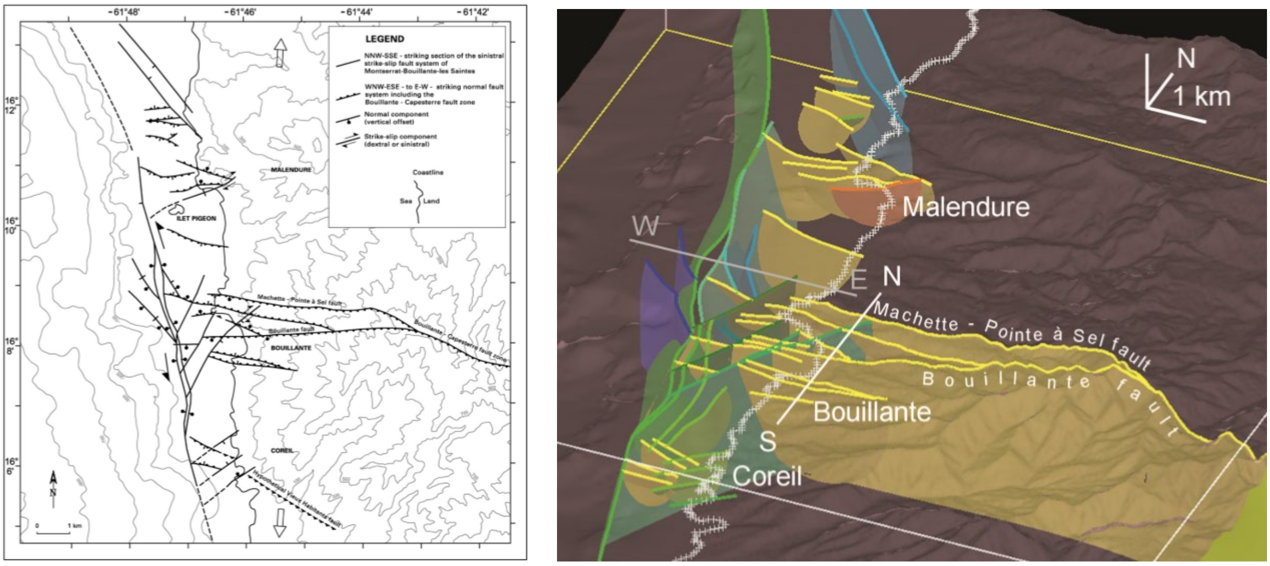

Figure 42: 3D-geological and structural model of the Bouillante geothermal system using Geomodeller (Calcagno et al., 2011) and data from Thinon et al. (2010).

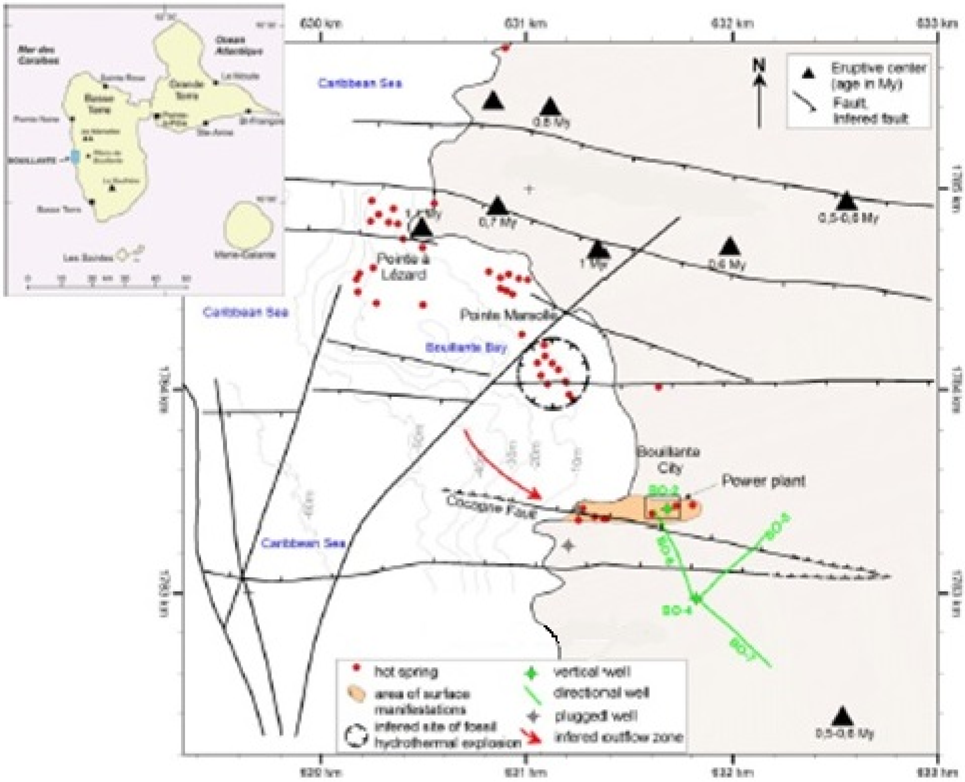

Figure 43: Synthetic map of the Bouillante geothermal area with the location of the wells, main hydrothermal manifestations and faults, and volcanism ages (from Traineau et al., 2015, and adapted from Bouchot et al., 2010).

3.2 MAIN FLUID GEOCHEMICAL CHARACTERISTICS

3.2.1 Previous results

The geochemical monitoring of the deep fluids discharged from the Bouillante production wells carried out by BRGM between 1995 and 2013, for which the analytical data have been integrated in the REFLECT database (within the framework of WP3), has shown that:

- the geochemical composition of all these fluids (waters and incondensable gases) is similar (Sanjuan et al., 2004; 2008; 2010; 2013; Fig. 44);

- the deep water, NaCl-type, with a TDS of about 20 g/l and a pH value close to 5.3, discharged from the Bouillante geothermal reservoir, is constituted of 58% seawater and 42% freshwater, as suggested by the Cl-Br, Cl-δD and Cl-$\delta^{18}O$ diagrams (Sanjuan, 2001). The reconstructed chemical and isotopic compositions of the reservoir fluid given by Sanjuan et al. (2010) are reported in Table 8 (water) and in Table 9 (incondensable gases);

- this fluid has acquired its chemical and isotopic composition after interaction with volcanic rocks at 250-260°C, as suggested by the main chemical and isotope geothermometers and geochemical modelling (Sanjuan, 2001; Sanjuan et al., 1999; 2001);

- a relatively high water/rock ratio is suggested by the absence of $^{18}O_{H2O}$ isotope enrichment from rock dissolution (Sanjuan et al., 1999; 2001);

- no significant variation of geochemical composition was observed during the geochemical monitoring of the exploitation of these fluids between 1995 and 2013 (Fig. 44).

Table 8: Reconstructed chemical and isotopic compositions of the Bouillante reservoir water (from Sanjuan et al., 2010).

Species	Value	Species	Value
pH	5.3 ± 0.3	**Sr (mg/l)**	16.0 ± 2.0
TDS (g/l)	20.0 ± 1.0	**Ba (mg/l)**	6.5 ± 1.0
Cl (g/l)	12.0 ± 0.6	**Mn (mg/l)**	4.8 ± 1.0
Na (g/l)	5.1 ± 0.3	**Li (mg/l)**	4.5 ± 0.5
Ca (g/l)	1.8 ± 0.1	**Rb (mg/l)**	2.2 ± 0.3
K (mg/l)	750 ± 40	**Cs (µg/l)**	260 ± 30
HCO_3 (mg/l)	50 ± 20	**Al (µg/l)**	60 ± 10
Mg (mg/l)	1.6 ± 0.2	**Fe (mg/l)**	3.2 ± 1.0
SO_4 (mg/l)	16 ± 1	**Cu (mg/l)**	15.0 ± 1.0
SiO_2 (mg/l)	500 ± 30	**Ni (mg/l)**	2.0 ± 0.5
H_2S (mg/l)	34 ± 3	**Zn (µg/l)**	650 ± 100
Br (mg/l)	42 ± 5	**As (µg/l)**	350 ± 50
B (mg/l)	12.5 ± 1.3	**As(III) (µg/l)**	280 ± 40
F (mg/l)	0.9 ± 0.1	**As(V) (µg/l)**	70 ± 15
NH_4 (mg/l)	1.7 ± 0.2	**Cr (µg/l)**	15 ± 2
NO_3 (mg/l)	< 0.5	**Co (µg/l)**	13 ± 1
NO_2 (mg/l)	< 0.01	**Pb (µg/l)**	4.0 ± 1.0
PO_4 (mg/l)	< 0.1	**Be (µg/l)**	< 0.1
δD (‰)	-1.2 ± 0.8	**$\delta^{18}O$ (‰)**	-1.1 ± 0.2
$\delta^{34}S$ (SO_4) (‰	19.1 ± 0.4	**$\delta^{18}O$ (SO_4) (‰)**	5.6 ± 0.2
$\delta^{13}C$ (‰)	-3.9 ± 0.2	**$\delta^{11}B$ (‰)**	16.3 ± 0.2
$\delta^{7}Li$ (‰)	4.4 ± 0.3	**$^{87}Sr/^{86}Sr$**	0.70496 ± 0.0001

Table 9: Reconstructed chemical and isotopic compositions of the Bouillante reservoir incondensable gases. CO2 is the predominant gas. GSR is the weight gas/steam ratio (from Sanjuan et al., 2010).

Gas	%	Gas	%
CO_2	93	**He**	0.0035
O_2	0	**H_2S**	2.8
N_2	3.5	**CH_4**	0.4
Ar	0.04	**C_2H_6**	0.006
H_2	0.3	**C_3H_8**	0.0008
GSR	0.4	**$\delta^{13}C$**	-2.6‰

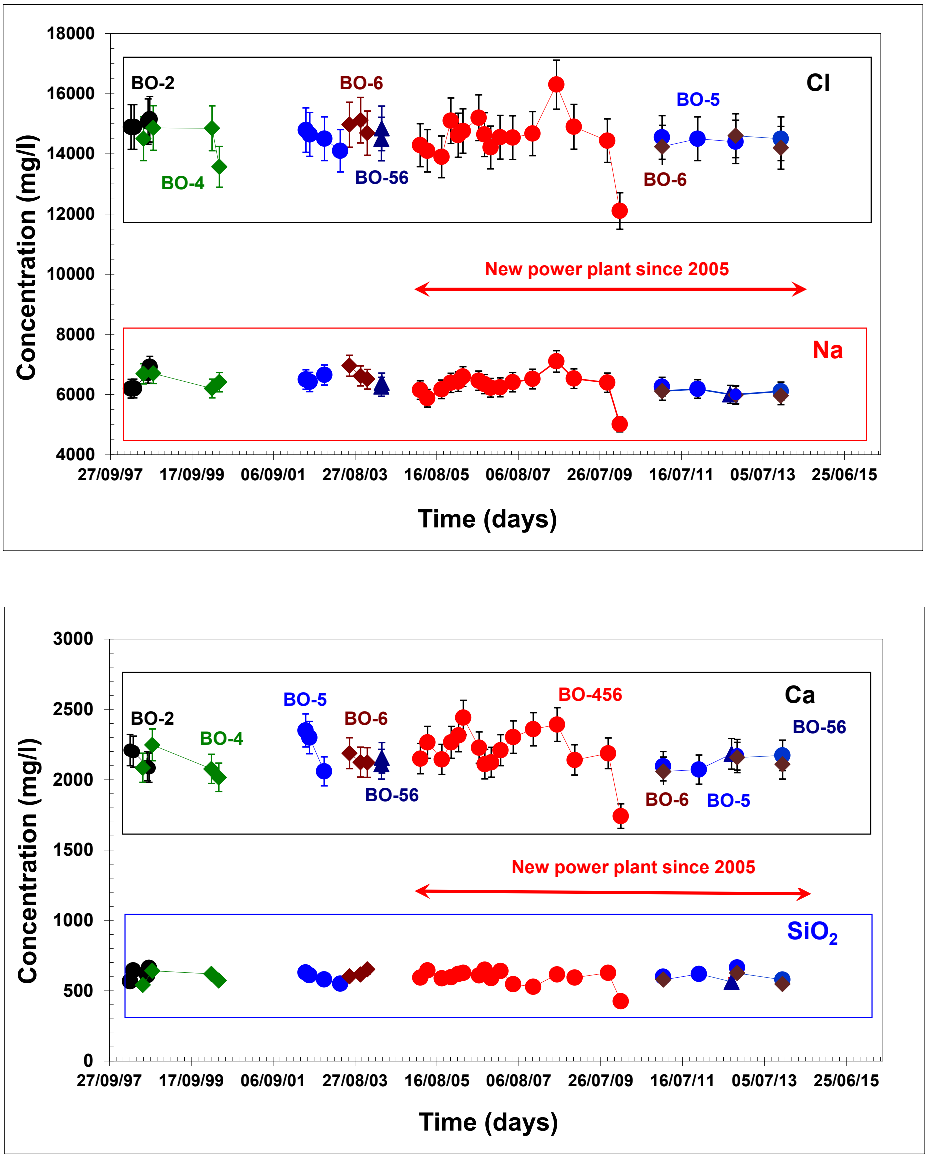

Figure 44: Chloride, sodium, calcium and silica concentrations analysed in the waters collected from the Bouillante geothermal wells, after phase separation at 160°C (about 20% steam and 80% water; from Sanjuan et al., 2013).

Moreover, Sanjuan et al. (2001) and Millot et al. (2010) have shown that the waters of all the submarine thermal springs in the Bouillante geothermal area are constituted of a mixing between this type of fluid and seawater at different proportions (Figs. 39 and 45), suggesting the existence of a big common deep geothermal reservoir in the Bouillante geothermal area. The latter could be still deeper according to the Li isotopic signature of the deep waters and the Li isotopic fractionation between water and rocks at 260°C (Millot et al., 2010).

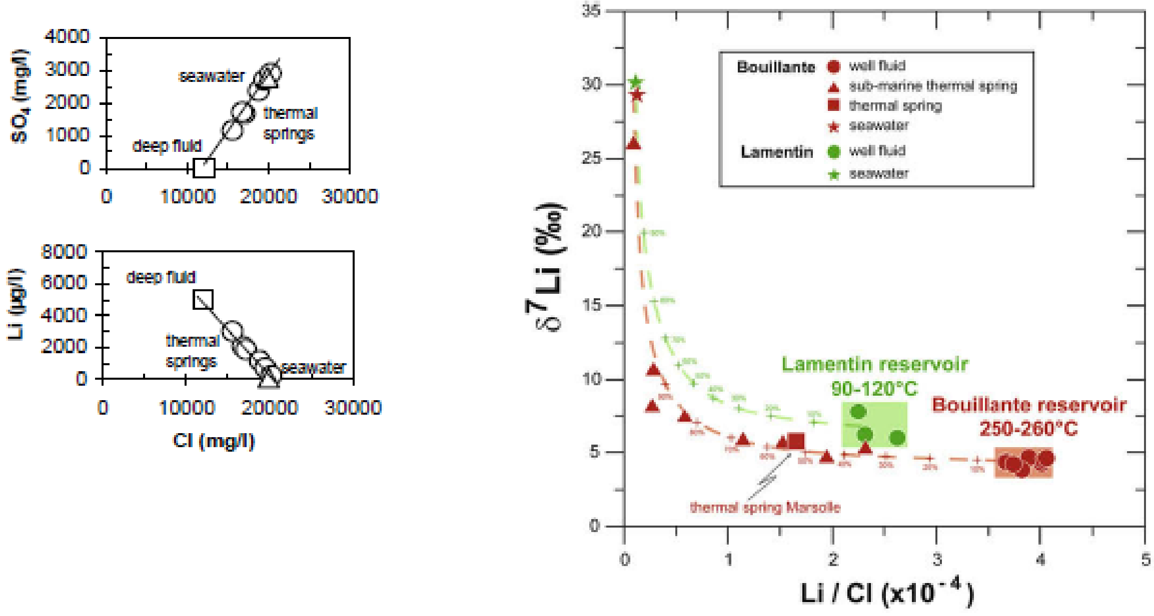

Figure 45: Cl-SO$_4$, Cl-Li and Li/Cl-δ^{7}Li diagrams for seawater, submarine thermal springs of the Bouillante Bay and the Bouillante reservoir geothermal water, indicating that all the thermal submarine waters results from a mixing between the deep reservoir water and seawater at different proportions (from Sanjuan et al., 2001, and Millot et al., 2010). These proportions can be easily calculated (see Figure 39).

In addition to the geochemical monitoring of the fluids discharged from the geothermal wells, the thermal waters, fumaroles and hot soils located near the power plant were also monitored (Sanjuan et al., 2002; 2004; 2008; 2010, 2013; Sanjuan and Brach, 2015).

3.2.2 Analytical results obtained during this study

Because of the Covid situation and travel restrictions to the Guadeloupe Island, colleagues from the University of Antilles and GB-Ormat staff carried out the sampling of Bouillante water on 19th January 2021. These water samples were directly collected from the BO-6 wellhead (Fig. 46) to have fluid samples of only this well and not after the High Pressure (HP) phase separator at 160°C, in order to avoid sampling a mixing of fluids discharged from BO-5 and BO-6.

Figure 46: Fluid sampling point (red circle) located just after the BO-6 wellhead.

The water samples were stored in 100 ml polyethylene bottles and conditioned on site, according to the specifications for chemical analysis (0.45 µm filtered for major and some trace anions, or 0.45 µm filtered and acidified for the other species). Conductivity and pH (± 0.05) were also measured on site. The corresponding water samples were sent to BRGM laboratories for chemical analyses of major, trace and infra-trace species and to GFZ for analysis of radionuclide elements.

The chemical analyses (major cations and anions, dissolved SiO_2, trace and infra-trace elements) were carried out in the BRGM laboratories, using standard water analytical techniques such as ion chromatography, inductively coupled plasma-atomic emission spectroscopy (ICP-AES), potentiometry, colorimetry, and inductively coupled plasma-mass spectrometry (ICP-MS). The precision for the major species is better than ± 5% and that for trace and infra-trace close to 10-15%. All the chemical results are reported in Table 10 and Table 11. The analytical results of radionuclide elements will be presented, discussed and interpreted by GFZ, but we can notice that the concentrations of these elements are very low, as already observed by Sanjuan et al. (2013).

When compared to analytical results previously obtained in similar conditions (fluid water directly collected after BO6-wellhead), most of the chemical composition is close to those of the previous water samples (Table 10 and Table 11; Fig. 47). The bromide concentration is surprisingly higher. For some trace (Fe) and infra-trace elements, problems of contamination or instability are probable.

Table 10 : Chemical composition (major species) of the water sample collected from the BO-6 wellhead in January 2021 compared with those previously obtained for other water samples collected at the same location (Sanjuan et al., 2008; 2013).

Fluid sample	Date	Cond. 25°C	pH	Eh$_{brut}$	Na	K	Ca	Mg	Cl	SO$_4$	Alk.	SiO$_2$	TDS	I.B.
		mS/cm		mV	mg/l	mg/l	mg/l	mg/l	mg/l	mg/l	mg/l HCO$_3$	mg/l	g/l	%
BO6-05-TPS-2-1E	23/03/2005 12:00	38.8	7.35	-152	6250	930	2180	1.4	14700	20.3	22.0	615	24.8	-2.58
BO6-05-TPS-2-2E	24/05/2005 14:30	38.8	7.20	-104	6035	939	2306	1.5	14400	21.8	23.8	600	24.4	-1.23
BO6-05-TPS-2-3E	28/09/2005 9:40	37.9	7.35	-215	6338	960	2173	1.3	14500	22.1	21.4	646	24.7	-0.17
BO6-05-TPS-2-4E	13/12/2005 10:30	33.7	6.04	-254	6352	924	2127	2.0	14400	18.7	26.8	600	24.5	-0.13
BO6-06-TPS-2-1E	22/02/2006 11:00	33.3	5.39	-184	6039	923	2195	2.3	13707	19.5	21.4	606	23.5	2.27
BO6-06-TPS-2-2E	04/04/2006 14:00	37.9	7.07	-231	6167	974	2266	1.4	14286	28.9	24.4	647	24.4	0.71
BO6-06-TPS-2-3E	24/08/2006 10:00	38.1	7.38	-247	6300	927	2312	1.5	15600	23.0	35.0	649	25.9	-6.44
BO6-06-TPS-2-4E	11/10/2006 10:45	40.4	7.25	-302	6567	968	2183	2.7	15074	22.0	22.6	696	25.6	-1.45
BO6-07-TPS-2-1E	27/02/2007 15:50	36.0	5.49	-199	5742	826	2057	1.9	13752	21.5	26.2	582	23.1	-3.87
BO6-07-TPS-2-3E	11/12/2007 10:00	37.5	5.10	-90	5880	827	2200	1.8	13891	19.8	29.9	576	22.9	-1.43
BO6-08-TPS-2-1E	12/03/2008	37.0	6.11	-139	5750	852	2032	1.7	13000	21.4	25.0	641	22.3	1.68
BO6-08-TPS-2-2E	07/07/2008 10:45	35.9	6.85	-177	6065	865	2025	1.1	14000	21.2	25.0	579	23.6	-2.13
BO6-08-TPS-2-3E	09/12/2008 14:50	35.0	5.98	-127	5877	883	2050	1.4	13819	21.1	28.1	590	22.7	-2.53
BO6-09-TPS-2-1E	01/10/2009	36.6	6.42	-140	5853	881	1993	1.0	13754	16.3	15.3	615	23.1	-3.05
BO6-10-TPS-2-1E	19/01/2010 15:00	31.9	4.76	-106	5123	788	1766	< 0.5	12300	15.2	21.4	534	20.5	-4.79
BO6-21-TPS-2-1E	1/19/2021	31.1	5.59		5515	809	2111	1.2	13599	18.5	22.0	561	22.6	-4.81

Table 11: Chemical composition (trace and infra-trace species) of the water sample collected from the BO-6 wellhead in January 2021 compared with those previously obtained for other water samples collected at the same location (Sanjuan et al., 2008; 2013).

Fluid sample	Date	PO$_4$	F	Br	B	NH$_4$	Li	Sr	Ba	Mn	Fe	Al	As	Rb	Cs	Ge	Co	Cr	Ni	Cu	Zn	Ag	Cd	Pb	W
		mg/l	mg/l	mg/l	mg/l	mg/l	mg/l	mg/l	mg/l	mg/l	mg/l	µg/l	µg/l	mg/l	µg/l	µg/l	µg/l	µg/l	µg/l	µg/l	µg/l	µg/l	µg/l	µg/l	µg/l
BO6-05-TPS-2-1E	23/03/05 12:00	< 0.1	1.6	49.5	15.00	1.1	4.69	17.65	7.61	5.32	0.120	21.0	414	2.46	300	10	< 5	4.6	11	13	4.5	< 0.5	< 0.5	< 0.5	
BO6-05-TPS-2-2E	24/05/05 14:30	< 0.1	1.4	45.4	14.59	1.1	4.61	17.44	7.43	5.23	0.220	28.0	400	2.87	347	12	< 2	< 5	< 5	3	< 5	< 5	< 20	< 20	
BO6-05-TPS-2-3E	28/09/05 09:40	< 0.1	1.6	51.0	14.78	1.3	4.88	18.39	7.22	5.12	< 0.2	31.5	397	2.38	340	< 10	5.8	< 5	21	< 2	< 5	< 5	< 5	< 5	
BO6-05-TPS-2-4E	13/12/05 10:30		1.4	48.6	15.41	1.3	4.55	18.18	7.92	5.77	0.190	49.0	426	2.70	318	13	< 2	< 5	< 5	< 2	< 5	< 5	< 2	< 20	
BO6-06-TPS-2-1E	22/02/06 11:00	< 0.1	1.0	44.3	13.85	0.6	4.53	16.50	6.55	4.98	0.180	61.0	363	2.76	325	14	< 2	< 2	< 5	< 2	5	< 5	< 2	< 2	
BO6-06-TPS-2-2E	04/04/06 14:00	< 0.1	1.0	57.2	14.46	< 0.5	4.39	17.36	7.83	5.40	0.140	18.0	437	2.59	302	14	< 2	< 5	7	5	11	< 5	< 2	< 2	
BO6-06-TPS-2-3E	24/08/06 10:00			57.2																					
BO6-06-TPS-2-4E	11/10/06 10:45	< 0.1	1.6	50.3	15.09	< 0,5	4.60	18.70	8.48	5.80	0.120	13.0	621	2.71	353	12	< 2	< 5	< 5	< 2	6	< 5	< 2	< 10	
BO6-07-TPS-2-1E	27/02/07 15:50			49.1		< 1	4.97																		
BO6-07-TPS-2-3E	11/12/07 10:00			45.4		< 1	5.10																		
BO6-08-TPS-2-1E	12/03/2008		1.6		12.80	1.5	4.90	18.94	7.19	4.90	0.120	92.0							1	0.2	2.4				
BO6-08-TPS-2-2E	07/07/08 10:45	< 0.1	1.3		14.54	1.3	4.85	18.54	7.12	4.96	0.120	25.4	453	3.02	348	8.6	0.1	0.2	3	0.2	1	< 0.1	< 0.1	0.1	
BO6-08-TPS-2-3E	09/12/08 14:50	< 0.1	1.0	46.6	12.18	1.4	4.82	17.60	7.75	5.48	0.910	22.0	395	2.79	342	10	0.2	0.4	16.4	< 0.3	2.1	< 0.1	< 0.1	< 0.1	
BO6-09-TPS-2-1E	01/10/2009	< 0.1	1.1	48.3	12.40	1.5	4.05	15.90	6.88	5.01	4.44	117	340	2.37	322	10	0.5	2.6	19	1	6	0.19	< 0.1	0.8	
BO6-10-TPS-2-1E	19/01/2010 15:00			48.0																					
BO6-21-TPS-2-1E	1/19/2021	< 0.1	1.4	63.1	15.25	1.6	4.89	20.44	7.70	5.37	1.63	72.1	406	2.49	323	10.5	0.56	3.4	129	0.94	16.1	< 0.01	< 0.01	0.43	7.97

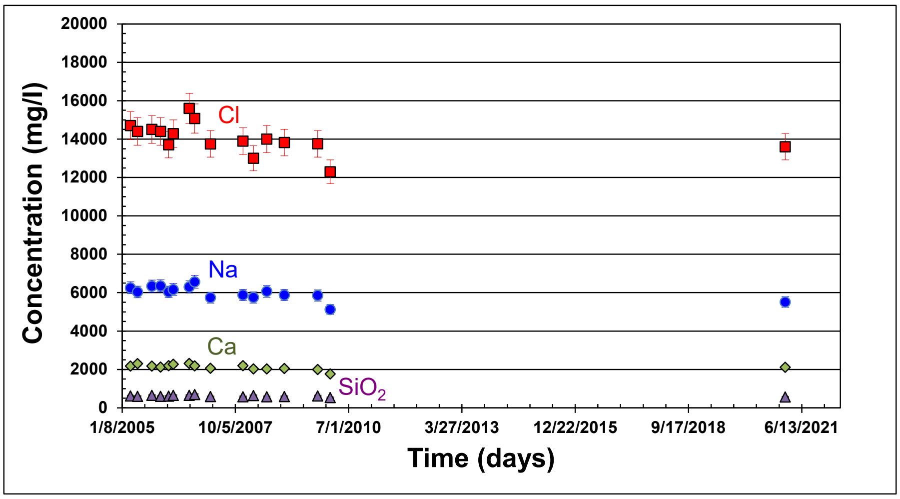

Figure 47: Concentrations of dissolved chloride, sodium, calcium and silica of the water sample collected from the BO-6 wellhead in January 2021 compared with those of other water samples previously collected at the same location.

For most of the water samples collected directly after the wellheads, the phase separation between water and steam is worse than for the water samples collected after the phase separator at 160°C. Consequently, their TDS values and elemental concentrations (Tables 12 and 13) are generally lower than those of the samples collected after the HP phase separator (Tables 14 and 15), with approximately 20% of steam and 80% of water, because the steam condensate remaining in the water of the wellhead samples has a slight dilution effect.

Table 12: Chemical composition (major species) of water samples collected after the HP phase separator at 160°C (Sanjuan et al., 2013).

Fluid sample	Date	Cond. 25°C	pH	Eh_{brut}	Na	K	Ca	Mg	Cl	SO_4	Alk.	SiO_2	TDS	I.B.
		mS/cm		mV	mg/l	mg/l	mg/l	mg/l	mg/l	mg/l	mg/l HCO_3	mg/l	g/l	%
BO56-13-MEHP-1	21/05/2013	39.0	7.35	-295	6150	930	2167	1.7	14988	21.3	18	535	24.8	-5.75
BO56-14-MEHP-1	15/10/2014 09:15	40.1	7.14	-304	6481	983	2356	< 0.5	15373	20.4	31	616	25.9	-2.24
BO5-13-MEHP-1	11/12/2013	39.7	7.00	-140	6109	920	2173	0.6	14500	20.3	26	578	24.3	-2.93
BO5-14-MEHP-1	29/04/2014				6267	935	2207	0.9	14500	22.0	19	610	24.6	-0.67
BO6-13-MEHP-1	11/12/2013	39.5	6.99	-179	5962	883	2110	< 0.5	14200	23.1	24	547	23.7	-3.51
BO6-14-MEHP-1	30/04/2014				6290	936	2256	5.5	15096	31.4	19	610	25.2	-3.75

Table 13: Chemical composition (trace and infratrace species) of water samples collected after the HP phase separator at 160°C (Sanjuan et al., 2013).

Fluid sample	Date	PO_4	F	Br	B	NH_4	Li	Sr	Ba	Mn	Fe	Al	As	Rb	Cs	Ge	Co	Cr	Ni	Cu	Zn	Ag	Cd	Pb
		mg/l	mg/l	mg/l	mg/l	mg/l	mg/l	mg/l	mg/l	mg/l	mg/l	µg/l	µg/l	mg/l	µg/l	µg/l	µg/l	µg/l	µg/l	µg/l	µg/l	µg/l	µg/l	µg/l
BO56-13-MEHP-1	21/05/2013		1.4		14.75	1.24	5.11	19.29	7.74	5.70	0.250	49.1												
BO56-14-MEHP-1	15/10/2014 09:15	< 0.05	1.6	49.2	16.19	1.19	5.18	19.88	8.47		0.020			2.68	336	11.5			0.66	< 0,1	< 0.5			< 0.05
BO5-13-MEHP-1	17/09/2013		1.4		14.64	1.24	4.75	19.40	7.84	5.35	0.106	12.7												
BO5-13-MEHP-2	11/12/2013	< 0.1	1.4	56.0	14.64	0.97	5.23	20.15	7.77	5.48	0.197	34.7	399	2.76	336	11.0	< 0.5		< 1	< 1	< 5	< 0.1	0.16	< 0.5
BO5-14-MEHP-1	29/04/2014		1.5	49.5	13.70	1.21	4.81	18.37	7.30	5.32	0.142	26.9												
BO6-13-MEHP-1	18/09/2013		1.4		14.43	1.09	4.66	19.03	7.39	4.84	0.132	21.7												
BO6-13-MEHP-2	11/12/2013	< 0.1	1.4	55.4	15.04	0.97	5.14	19.89	7.43	5.01	0.123	21.6	400	2.79	343	10.9	< 0.5		< 1	< 1	< 5	< 0.1	0.41	< 0.5
BO6-14-MEHP-1	30/04/2014		1.6	49.5	14.22	1.15	4.99	19.12	7.57	4.93	0.117	17.3												

As expected, most of the chemical geothermometers applied on the water sample collected in January 2021 give estimations of reservoir temperature close to 250-260°C (Table 16), similar to the previous estimations and to the measured well temperatures (Sanjuan et al., 1999; 2001; 2008; Millot et al., 2010).

Table 14: Reservoir temperatures estimated using the main chemical geothermometers for the water sample collected from the BO-6 wellhead in January 2021.

Fluid sample	Date	T_{Qz} °C	$T_{Na\text{-}K\,(1)}$ °C	$T_{Na\text{-}K\,(2)}$ °C	$T_{Na\text{-}K\text{-}Ca\text{-}Mg}$ °C	$T_{K\text{-}Mg}$ °C	$T_{Na\text{-}Li}$ °C	T_{KF} °C	$T_{estimated}$ °C
BO6-21-TPS-2-1E	19/01/2021	263	251	265	254	261	246	266	**260 ± 20**

T_{Qz}: Fournier (1977).
$T_{Na\text{-}K\,(1)}$: Fournier (1979);$T_{Na\text{-}K\,(2)}$: Giggenbach (1988).
$T_{Na\text{-}K\text{-}Ca\text{-}Mg}$: Fournier and Potter (1979).
$T_{K\text{-}Mg}$: Giggenbach (1988).
$T_{Na\text{-}Li}$: Sanjuan *et al.* (2014).
T_{KF}: Michard (1990).

All these results indicate that the chemical composition of the fluids discharged from the Bouillante wells is more or less unchanged after more than 15 years of production of the power plant commissioned in 2005. Consequently, for the works of geochemical modelling envisaged within the framework of the REFLECT project, relative to the scale deposits which could occur during the exploitation of the Bouillante reservoir, especially for amorphous silica precipitation, similar chemical compositions as those used in previous studies (Serra et al., 2004; Azaroual et al., 2005; Dixit, 2014; Dixit et al., 2016; 2020) can be selected.

3.3 CONCLUSION

Numerous studies of geothermal exploration and monitoring have been carried out by BRGM in the high-temperature Bouillante geothermal field between 1995 and 2016 and have contributed to better know and understand this geothermal system. Among these studies, the works of geochemical exploration and fluid geochemical monitoring have allowed acquiring the main characteristics of the fluids discharged from the geothermal wells and from the thermal springs and fumaroles located in the Bouillante geothermal field. The analytical data obtained for all the geothermal wells have been integrated within the framework of WP3 in the REFLECT database.

The water sample directly collected from the BO-6 wellhead in January 2021, which has been analysed in the BRGM laboratories during this study, indicates that the chemical composition of the fluids discharged from the Bouillante wells is unchanged after more than 15 years of production of the power plant commissioned in 2005, when compared with other water samples previously collected and analysed. Consequently, for the works of geochemical modelling foreseen within the framework of the REFLECT project, relative to the scale deposits which could occur during the exploitation of the Bouillante reservoir, especially for amorphous silica precipitation, similar chemical compositions as those used in previous studies can be selected.

3.4 REFERENCES

Azaroual M., Serra H., Sanjuan B. (2005) - Modélisation couplée chimie - transport du refroidissement du fluide géothermal de Bouillante (Guadeloupe). *BRGM/RP-53313-FR final report*, 46 p.

Bouchot V., Sanjuan B., Traineau H., Guillou-Frottier L., Thinon I ., Baltassat J.-M., Fabriol H., Bourgeois B., Lasne E. (2010) - Assessment of the Bouillante geothermal field (Guadeloupe, French West Indies): Toward a conceptual model of the high temperature geothermal system. *In Proceedings of World Geothermal Congress 2010 (WGC2010), Bali, Indonesia, 25-29 April 2010,* 7 p.

Calcagno P., Bouchot V., Thinon I., Bourgine B. (2011) - A new 3D fault model of the Bouillante geothermal province combining on-shore and off-shore structural knowledge (French West Indies). *Tectonophysics,* 526-529, 185-195.

Correia H., Sigurdsson O., Sanjuan B., Tulinius H., Lasne E. (2000) - Stimulation of a high enthalpy geothermal well by cold water injection. *In Geothermal Resources Council Transactions, Davis, California, USA,* vol. 24, 129-136.

Dixit Ch. (2014) - Etude physico-chimique des fluides produits par la centrale géothermique de Bouillante (Guadeloupe) et des dépôts susceptibles de se former pendant leur exploitation et leur réinjection dans le sous-sol. *Thèse Doctorat Université Antilles-Guyane*, 254 p.

Dixit Ch., Bernard M.-L., Sanjuan B., André L., Gaspard S. (2016) - Experimental study on the kinetics of silica precipitation during the cooling of the Bouillante geothermal fluid (Guadeloupe, French West Indies). *Chemical Geology*, 442, 97-112.

Dixit Ch., Ncibi C.-M., Bernard M.-L., Sanjuan B., Gaspard S. (2020) - The valorization of raw and chemically-modified silica residues from Bouillante geothermal fluids (Guadeloupe, FWI) for the removal of methylene blue and lead from aqueous media. *Journal of Environmental Chemical Engineering*, 8, 11 p., doi.org/10.1016/j.jece.2020. 104285.

Fabriol H., Bitri A., Bourgeois B., Debeglia N., Genter A., Guennoc P., Jousset P., Miehe J.M., Roig J.Y., Thinon I., Traineau H., Sanjuan B., Truffert C. (2005) - Geophysical methods applied to the assessment of the Bouillante geothermal field (Guadeloupe, French West Indies). *Proceedings World Geothermal Congress 2005, Antalya, Turkey, 24-29 April 2005*, 6 p.

Feuillet N., Manighetti I., Tapponnier P. (2001) - Extension active perpendiculaire à la subduction dans l’arc des petites Antilles (Guadeloupe, Antilles francaises) [Active extension perpendicular to the subduction in the lesser Antilles arc (Guadeloupe, French West Indies)]. *CR Acad Sci Paris Earth Planet. Sci.*, 333(9), 583-590.

Feuillet N., Manighetti I., Tapponnier P. (2002) - Arc parallel extension and localization of volcanic complexes in Guadeloupe, Lesser Antilles. *J. Geophys. Res.*, 107(B12)), 2331-2359.

Fournier, R.O. (1977) - Chemical geothermometers and mixing models for geothermal systems. *Geothermics*, 5, 41-50.

Fournier R.O. (1979) - A revised equation for the Na/K geothermometer. *Geoth. Res. Council Trans.*, 3, p. 221-224.

Fournier R.O. and Potter R.W. (1979) - Magnesium correction to the Na-K-Ca chemical geothermometer. *Geochim. Cosmochim. Acta*, 43, 1543-1550.

Gailler L.-S., Bouchot V., Martelet G., Thinon I., Coppo N., Baltassat J.-M., Bourgeois B. (2014) - Contribution of multi-method geophysics to the understanding of a high-temperature geothermal province: The Bouillante area (Guadeloupe, Lesser Antilles). *Journal of Volcanology and Geothermal Research*, vol. 275, 34-50.

Giggenbach W.F. (1988) - Geothermal solute equilibria. Derivation of Na-K-Mg-Ca geoindicators. *Geochim. Cosmochim. Acta* 52, p. 2749-2765.

Hamm V., Lopez S., Gille A.-L. (2016) - Projet de recherche ORBOU : 2. Travaux de modélisation associés à la réinjection partielle des fluides de production de la centrale géothermique de Bouillante en Guadeloupe (2014-2016). *BRGM/RP-65939-FR report*, 46 p.

Lachassagne P., Maréchal J.-C., Sanjuan B. (2009) - Hydrogeological model of a high-energy geothermal field (Bouillante area, Guadeloupe, French West Indies). *Hydrogeology Journal,* 17, 1589-1606.

Michard G. (1990) - Behaviour of major elements and some trace elements (Li, Rb, Cs, Sr, Fe, Mn, W, F) in deep hot waters from granitic areas. *Chem. Geol.*, 89, p. 117-134.

Millot R., Scaillet B., Sanjuan B. (2010) - Lithium isotopes in island arc geothermal systems: Guadeloupe, Martinique (French West Indies) and experimental approach. *Geochimica et Cosmochimica Acta*, 74, 1852-1871.

Sanjuan B. (2001) - Champ géothermique de Bouillante (Guadeloupe) : Synthèse des travaux réalisés en géochimie avant 1999. *BRGM/RC-51672-FR report*, 54 p.

Sanjuan B., Brach M. (2015) - Geochemical monitoring of the thermal manifestations located near the Bouillante geothermal power plant, in Guadeloupe (FWI). *11th Applied Isotope Geochemistry Conference, AIG-11, Orléans, France, 21-25 September 2015, Procedia Earth and Planetary Science*, 13, 25-29.

Sanjuan B., Lasne E., Brach M., Vaute L. (1999) - Bouillante geothermal field (Guadeloupe). Geochernical monitoring during the stimulation operation. Critical evaluation of chemical and isotope field data. *BRGM/RP-40646-FR report*, 99 p.

Sanjuan B., Brach M., Lasne E. (2001) - Bouillante geothermal fluid: mixing and water/rock interaction processes at 250°C. *Water Rock Interaction, WRI-10, International Symposium on Water Rock Interaction 10th, Villasimius (Italy), 10-15 juin 2001, Edited by R. Cidu, A.A. Balkema Publishers, vol. 2,* 911-914.

Sanjuan B., Traineau H., Lasne E., Brach M. (2002) - Travaux scientifiques menés par le BRGM et la CFG sur le champ géothermique de Bouillante, Guadeloupe (juillet 1999 - janvier 2002). *Final report n° 2002 BRGM-CFG*, 130 p.

Sanjuan B., Le Nindre Y.M., Menjoz A., Sbai A., Brach M., Lasne E. (2004) - Travaux de recherche liés au développement du champ géothermique de Bouillante (Guadeloupe). *BRGM/RP-53136-FR report*, 166 p.

Sanjuan B., Traineau H., Roig J.Y., Miehé J.M., Cotiche C., Lachassagne P., Maréchal J.-C., Fabriol H., Brach M. (2005) - Reconnaissance du potentiel géothermique du secteur nord de la baie de Bouillante, en Guadeloupe, par des méthodes d'exploration de surface. *BRGM/RC-53634-FR report*, 120 p.

Sanjuan B., Lopez S., Guillou-Frottier L., Le Nindre Y.-M., Menjoz A. (2008) - Travaux de recherche liés au projet GHEDOM-ADEME (2006-2008). *BRGM/RP-56432-FR final report*, 214 p.

Sanjuan B., Jousset Ph., Pajot G., Debeglia N., De Michele M., Brach M., Dupont F., Braibant G. Lasne E., Duré F. (2010) - Monitoring of the Bouillante geothermal exploitation (Guadeloupe, French West Indies) and the impact on its immediate environment. *In Proceedings of World Geothermal Congress 2010 (WGC2010), Bali, Indonesia, 25-29 April 2010,* 11 p.

Sanjuan B., Bouchot V., Mathieu F., Jousset Ph., Delatre M., De Michele M., Millot R., Innocent Ch. (2013) - Travaux de recherche sur le champ géothermique haute température de Bouillante, en Guadeloupe (2009-2012). *BRGM/RP-61715-FR report*, 192 p.

Sanjuan B., Millot R., Asmundsson R., Brach M., Giroud N. (2014) - Use of two new Na/Li geothermometric relationships for geothermal fluids in volcanic environments. *Chemical Geology*, 389, 60-81.

Serra H., Sanjuan B., Azaroual M. (2004) - Modélisation géochimique des risques de dépôts minéraux au cours de l'exploitation des forages géothermiques de Bouillante (Guadeloupe). *BRGM/RP-53154-FR report*, 56 p.

Thinon I., Guennoc P., Bitri A., Truffert C. (2010) - Study of the Bouillante Bay (West Basse-Terre Island shelf): contribution of geophysical surveys to the understanding of the structural context of Guadeloupe (French West Indies - Lesser Antilles). *Bull. Soc. Géol. Fr.*, 181, 51-65.

Traineau H., Sanjuan B., Beaufort D., Brach M., Castaing C., Correia H., Genter A., Herbrich B. (1997) - The Bouillante geothermal field (F.W.I.) revisited: new data on the fractured geothermal reservoir in light of a future stimulation experiment in a low productive well. In: *Proceedings, Twenty-Second Workshop on Geothermal Reservoir Engineering, Stanford University, Stanford, California, January 27-29, 1997,* SGP-TR-155, 97-104.

Truffert C., Thinon I., Bitri A., Lalanne X. (2004) - Using MAGIS for geothermal application: Guadeloupe Archipelago in French West Indies. *Hydro International, July/August 2004*, 1-3.

Verati Ch., Patrier-Mas P., Lardeaux J.-M., Bouchot V. (2014) - Timing of geothermal activity in an active island-arc volcanic setting: First ^{40}Ar-^{30}Ar dating from Bouillante geothermal field (Guadeloupe, French West Indies). *From Jourdan F., Mark D.-F. & Verati Ch. Eds, Advances in* ^{40}*Ar*^{39}*Ar Dating: from Archaeology to Planetary Sciences, Geological Society, London, Special Publications,* 378, 285-295.

4 GEOTHERMAL FLUIDS FROM ICELANDIC HIGH-TEMPERATURE FIELDS

Iceland has been a world leader in geothermal utilization, an important alternative sub-surface energy source, with 6.26 MWt per 1000 habitants (Lund and Boyd, 2016). Geothermal areas have been commercially exploited for electricity production since the 1960s, with the development of the first plant at Námafjall, located in the Northern Volcanic Zone (NVZ) (Gudmundsson, 1983). Today, Iceland has an installed electricity generation capacity of 753 MWe (Ragnarsson et al., 2020).

The country has been divided into volcanic zones based on the volcanic eruption style, the magmatic products, and the position relative to the mid-ocean ridge (MOR) and the Icelandic mantle plume. The volcanic rift zones are the Reykjanes Volcanic Zone, the Eastern and Western volcanic zones, set along the two southern branches of the North Atlantic MOR, and the Northern Volcanic Zone, on the main active MOR rift in the northern part of Iceland (Sigmundsson et al., 2018). The Northern Volcanic Zone has been the main spreading zone in the north of Iceland for the past 6-7 Ma, characterized by oblique extension creating five en echelon spreading segments in the NVZ. Each segment has a fissure swarm and an associated central volcanic that is the focus of volcanic and high-temperature geothermal activities. These volcanic centers are Kverkfjöll, Askja, Fremrinámar, Krafla, and Theistareykir (Pedersen et al., 2009), of which high-temperature fluids were sampled from geothermal fields of the latter two in the context of the REFLECT project.

4.1 KRAFLA GEOTHERMAL FIELD

The Krafla geothermal area is located within the caldera of the Krafla central volcano, which lies astride one of five en echelon fissure swarms (Stefánsson, 1981; Figure 48). The fissure swarm that intersects the Krafla caldera, which was formed about 100 thousand years ago, is 5-8 km wide and about 100 km long (Sæmundsson, 1974, 1978, 1983). Two other fracture systems have been identified in the Krafla area. Near Hvíthólar, curved caldera rim fractures are exposed, and NW-SE trending fissures are found in the Sudurhlídar wellfield that have been related to intrusive activity into the roots of the central volcano (Sæmundsson, 1983; Árnason et al., 1984). The main surface activity is near Leirhnjúkur in the center of the caldera and in its southeastern part in Hveragil and Víti (Stefánsson, 1981; Ármannsson et al., 1987). Thus, the surface activity is associated with the two main volcano-tectonic fissures within the caldera

(Gudmundsson and Arnórsson, 2002). The water discharged from wells at Krafla is very dilute with the dissolved solids content generally lying in the range of 1000 – 1500 ppm. The gas content of individual well discharges is very varaiable (Gudmundsson and Arnórsson, 2002). Based on stable water isotopes, the hydrothermal fluid is likely derived from local precpitation (Sveinbjörnsdóttir et al., 1986; Darling and Ármannsson, 1989).

A major volcanic-rifting episode started on the Krafla fissure swarm in late 1975. The first eruption started on 20 December 1975. A total of nine volcanic eruptions took place during this episode over a period of nine years, the last one in September 1984. An 80 km segment of the plate boundary was affected by ground deformation, intense earthquakes, and magmatism (Björnsson et al., 1979; Ármannsson et al., 1987).

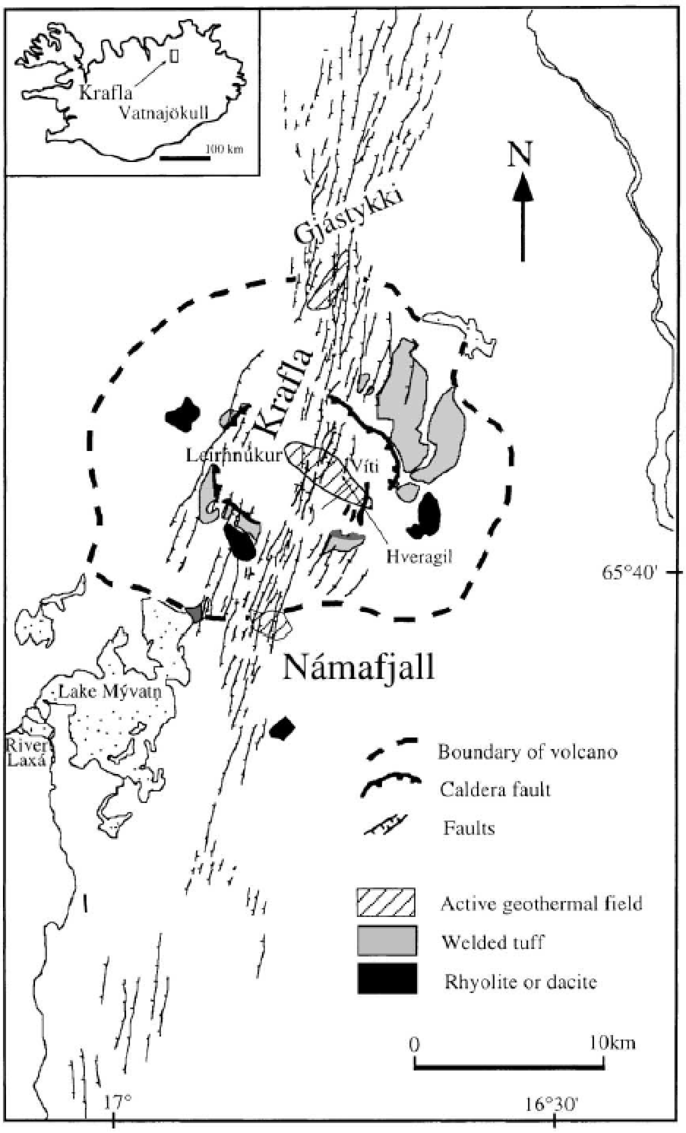

Figure 48. *The Krafla and Námafjall geothermal areas and associated central volcano and fissure swarm (Gudmundsson and Arnórsson, 2002).*

This high-temperature geothermal area has been exploited for steam production since the late 1970s. Power generation was 30 MWe until 1998, when it was increased to 60 MWe. The drilled area has been divided into three wellfields, Leirbotnar, Sudurhlídar, and Hvíthólar (Figure 49). A total of 34 wells have been drilled into the Krafla geothermal reservoir with the highest temperatures recorded downhole at 350 °C. Gudmundsson and Arnórsson (2002) observed that the decrease in geothermometry temperatures over time is largely caused by cold recharge and not so much by cooling from extensive boiling in producing aquifers. Colder water recharge was most prominent in wells in the Leirbotnar wellfield immediately west of Hveragil, as well as in well K-21 in Hvíthólar, with only well K-14 in the Sudurhlídar wellfield affected since 1995.

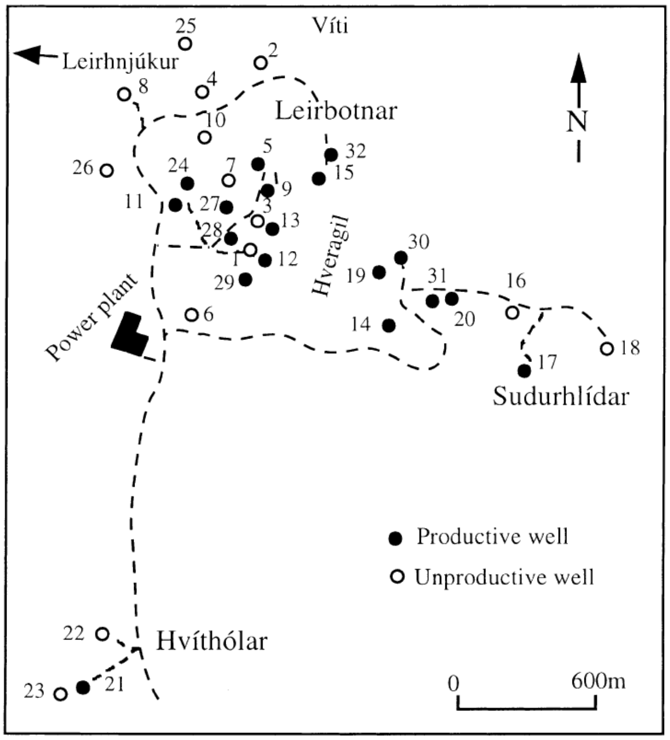

Figure 49. *The three wellfields at Krafla (Gudmundsson and Arnórsson, 2002).*

4.2 THEISTAREYKIR GEOTHERMAL FIELD

The most recent geothermal field developed for energy production is the Theistareykir geothermal field, which lies in the Theistarekyir fissure swarm in the NVZ in NE-Iceland, ca. 20 km north of the Krafla caldera. The high-temperature geothermal activity is connected to recent magma intrusions, with the most recent volcanic activity in the area occurring some 2500 years ago. Ármannsson et al. (1986) divided the Theistareykir geothermal area into five N-S oriented subareas (from east to west: A – Kertilfjall, B – Bóndhólsskard, C –

Theistareykjagrundir, D – Tjarnarás, and E – Theistareykjahraun) (Figure 50) on the basis of geology and geochemistry of fumaroles with isotopic composition of fumaroles confirming this division (Darling & Ármannsson, 1989; Sveinbjörnsdóttir et al., 2013). Based on stable water isotopes, Darling and Ármannsson (1989) suggested that Theistareykir was recharged by a combination of surface water and groundwater flowing from the south.

The development of the geothermal field began with nine wells drilled between 2002 and 2011. Based on this first set of wells, Óskarsson et al. (2013) determined a reservoir temperature range of 270–290 °C, although the bedrock temperature exceeds 300 °C. Exploitation of the field began in 2017, after a total of 18 wells had been drilled to depths ranging from 1723 m to 2799 m. The plant currently has two generating units of 45 MWe, making Theistareykir the fourth largest station in Iceland in terms of power generated (Saby et al., 2020).

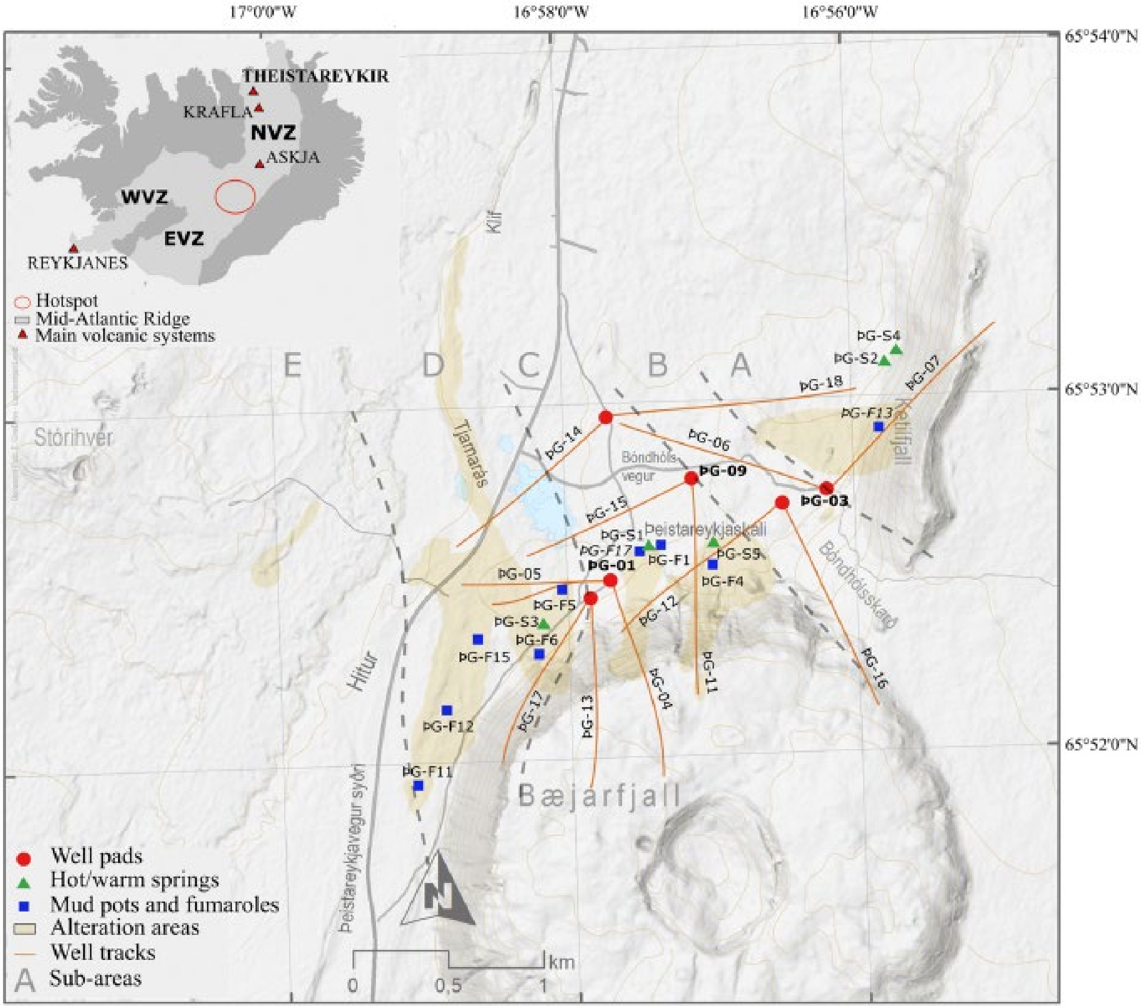

Figure 50. *Simplified map of the Theistareykir geothermal field with major alteration zones and positions of wells, mudpots, and fumaroles. Numbers on the X- and Y-axes indicate the latitudinal and longitudinal geographical coordinates. NVZ = Northern volcanic zone, WVZ = Western volcanic zone, EVZ = Eastern volcanic zone (Saby et al., 2020).*

4.3 METHODS

4.3.1 Sampling and analysis of geothermal fluids

Fluid samples were collected from the Theistareykir and Krafla geothermal fields in October 2020. Seven samples were collected from production wells, one sample from an injection well, and a sample from the cooling tower next to the power plant at Krafla (Figure 51), while seven samples were collected from production wells and two samples from injection wells at Theistarekykir (Figure 52). Sampling and preservation methods of geothermal fluids were as described by Ólafsson and Ármannsson (2006) and Arnórsson et al. (2006) and analysed at the ÍSOR laboratory unless otherwise specified. Liquid and vapor phase samples from production wells were separated by using a Webre separator.

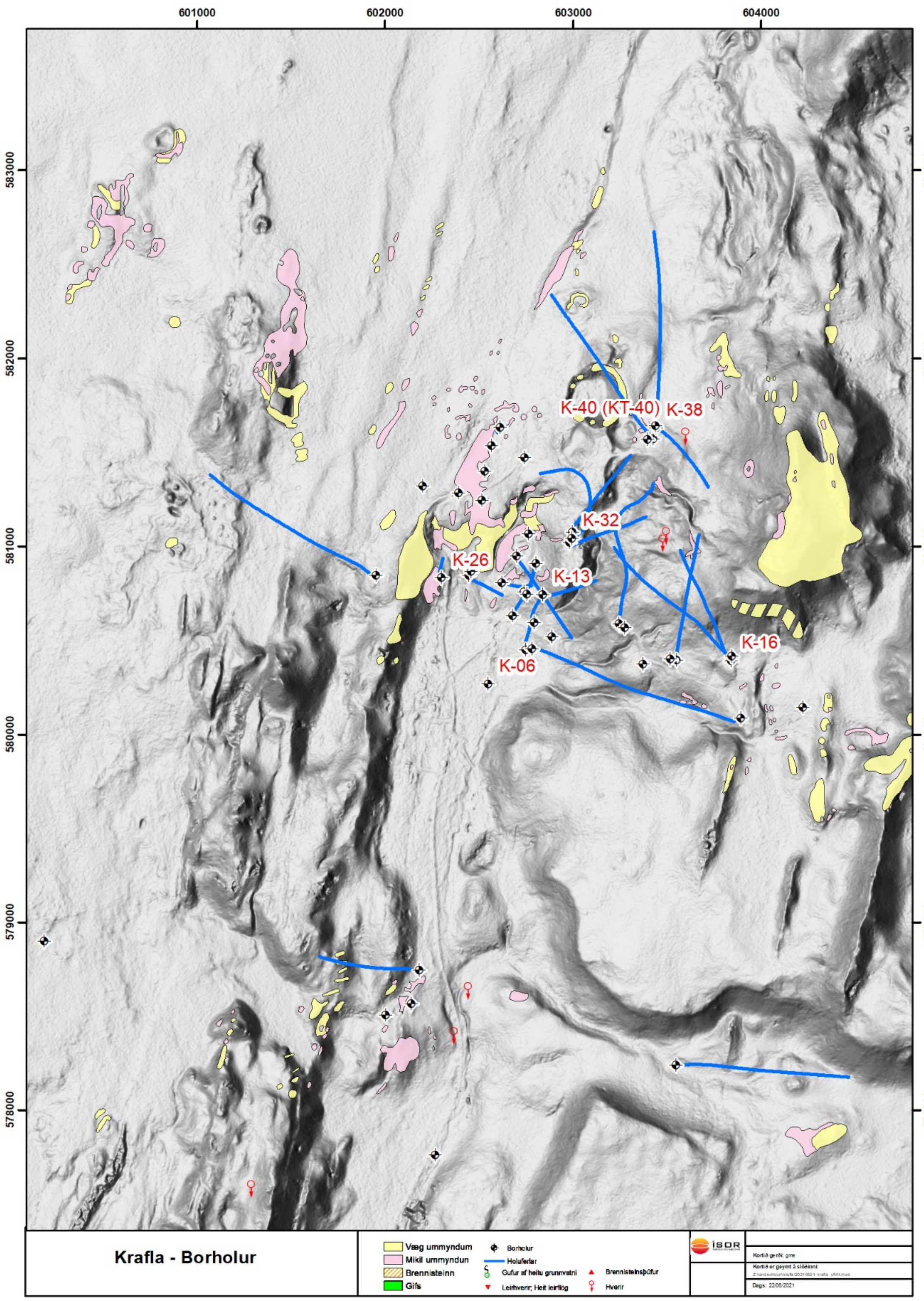

Figure 51. *Map of the Krafla geothermal field with major alteration zones and positions of wells and their well tracks, hot springs, and fumaroles. Wells sampled are labelled in red.*

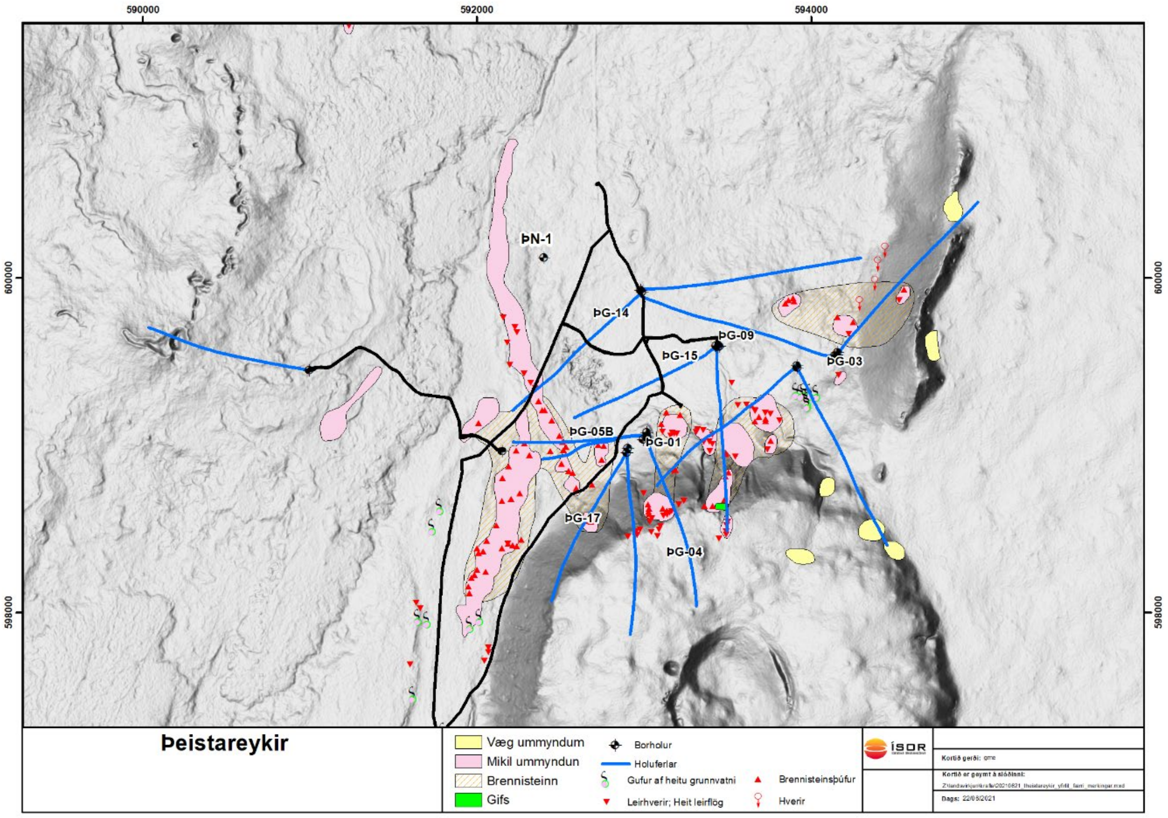

Figure 52. *Map of the Krafla geothermal field with major alteration zones and positions of wells and their well tracks, hot springs, and fumaroles. Wells sampled are labelled in black.*

Liquid phase samples from both production and injection wells were cooled down using an in-line cooling coil and filtered through a 0.2 µm filter (cellulose acetate). Major cations were measuring using ICP-OES on acidified samples (1% HNO3, Suprapur). Major anions were measured by ion chromatography. Two sets of anion samples were collected; one was left untreated and used for F and Cl determination and 1 ml of 2% Zn-acetate solution was added to the other per 100 ml sample to precipitate dissolved sulphide, which was subsequently filtered off followed by SO4 determination. Total dissolved inorganic carbon (DIC) was analysed using a modified alkalinity titration method (Stefánsson et al., 2007) by Landsvirkjun. Total dissolved sulphide was measured on-site with mercury precipitation titration and dithizone indicator (Arnórsson et al., 2006). The pH and conductivity were analysed on-site and in-line using a flow-through cell.

Vapor samples were collected into evacuated gas-bulbs containing 50% w/v KOH. The concentrations of CO2 and H2S in the vapor condensate within the gas-bulbs were determined using the modified alkalinity method and titration method previously mentioned. The non-condensable gases including H2, N2, Ar, and CH4 were analysed by gas chromatography. Vapor condensate were also collected using an in-line cooling coil, filtered, and acidified for analysis on ICP-OES.

Liquid phase samples were collected for UNINE for analysis of microorganisms. Samples were also collected for GFZ for Total Organic Carbon/Dissolved Organic Carbon as well as the determination of anions (F, Br, NO2, NO3, SO4, PO4, and formate, acetate, propionate, butyrate, valerate, oxalate/fumarate) by ion chromatography. Lastly, stable water (δ18O/δ2H), carbon (δ13C-DIC), and sulphur (δ 34S-H2S, δ18O-SO4) isotopes were collected from four production wells at the Theistareykir geothermal field for analysis by Hydrioisotop. All are partners within REFLECT.

4.3.2 Geochemical calculations

The composition of the deep liquid from the two-phase production wells was calculated using the chemical speciation program WATCH (Arnórsson et al., 1982; Bjarnason, 2010) and the results of analysis of the samples. The deep liquid composition is calculated at a certain reference temperature determined for each well. The reference temperature of production wells with a measured discharge enthalpy <1500 kJ/kg was determined by the calculated quartz temperature. For these wells, it may be assumed that the calculated concentrations of deep fluid dissolved solids will be approximately correct if the composition of the deep liquid is calculated using an enthalpy corresponding to the enthalpy of liquid water at the aquifer temperature (Friðriksson and Giroud, 2008; Arnórsson et al., 2007).

The reference temperature of wells with “excess enthalpy” (measured discharge enthalpy >1500 kJ/kg) was determined by comparing the measured temperature at the depth of producing aquifers in the well with the calculated quartz temperature of the deep liquid. In most cases, the excess enthalpy is due to segregation of the liquid and steam phases in the feeding aquifers of the well, which results in increased steam to liquid ratio. Another process is that the discharge fluid extracts heat from the reservoir rock as it undergoes depressurization boiling on its way to the surface. In this case, the above assumption for lower enthalpy wells would not be valid as the calculated concentration of dissolved gases might be overestimated.

Therefore, the deep liquid composition of “excess enthalpy” production wells is computed using a two-step procedure. It is assumed that the phase segregation occurs at a temperature where the steam fraction has reached 80% by volume. At this point, the liquid phase is practically immobile (Preuss, 2002), leading to the addition of "excess steam" to the well discharge, e.g., from a steam-rich shallow aquifer. In the first step, the composition of coexisting liquid and steam at the point of phase segregation is computed from the two-phase analysis, using a steam fraction calculated from the measured discharge enthalpy. Here, the assumption is made that the composition of the "excess steam" is the same as the composition of steam formed by boiling of fluid from the deeper aquifers, i.e. that the sample composition is representative of steam from both aquifers. In the second step, the deep liquid composition is computed using the liquid and steam composition at the phase segregation point and a steam fraction calculated assuming liquid enthalpy at the reference temperature. This yields a single liquid phase at the reference temperature. The mathematics of this approach are described in detail by Arnórsson et al. (2007).

Note that although liquid phase samples were obtained from wells K-38 and K-41, they were diluted by condensate from the vapor phase. These wells are mostly dry steam wells with some liquid in the bottom of the borehole, particularly for well K-41. Therefore, the deep fluid composition was not recalculated for these samples.

4.4 RESULTS

The measured chemical compositions of all samples collected are shown in Tables 15 and 16 from the Krafla and Theistareykir geothermal fields, respectively. The stable water, carbon, and sulphur isotope results from Hydroisotop are shown in Tables 17 to 19, respectively. The calculated chemical composition of the deep liquid from the two-phase production wells based on the methods described in Section 4.3.2 is then shown in Tables 20 and 21 for Krafla and Theistareykir, respectively. The data in Tables 15 to 19 will be entered into the REFLECT fluid database. Evaluation and interpretation of the results are ongoing.

Table 15a. *Chemical composition of geothermal fluid samples from the Krafla geothermal field. Concentrations are given in mg/L unless otherwise stated.*

Location name	K-16	Cooling Tower	K-06	K-13A	Injection Well K-26
Date	2020-10-08	2020-10-08	2020-10-08	2020-10-08	2020-10-07
Sample id	20200202	20200199	20200198	20200197	20200195
Pressure (PS) [bar-g]	12.9	-	2.2	7.7	-
Temperature (TS) [°C]	-	22.4	137.7	174.5	106.8
GT ratio @ 25 °C	1	-	0.1009	0.1669	-
Discharge [kg/s]	2.81	-	40	30.59	51.4
Enthalpy [kJ/kg]	2560	-	1184	1260	-
Water					
pH [/ °C]	-	6.96 / 22.4	9.51 / 15.3	9.39 / 16	9.32 / 27.6
Cond. [µS/cm] @ 25 °C	-	162.2	1152	1142	1116
Al	-	-	1.29	1.47	1.4
As	-	-	<0.01	<0.01	0.0147
B	-	-	0.463	0.964	1.13
Ba	-	-	0.0012	0.00136	0.0016
Br	-	-	0.06	0.11	0.09
CO_2	-	8.8	62.9	66.2	69.6
Ca	-	-	1.93	2.66	2.22
Cl	-	-	31.6	53.4	49.9
Cr	-	-	<0.005	<0.005	<0.005
Cu	-	-	<0.005	<0.005	<0.005
F	-	-	1.32	1.66	1.56
Fe	-	-	<0.002	<0.002	0.0029
H_2S	-	-	33.8	62.5	40.2
K	-	-	29.9	34.1	35.2
Li	-	-	0.15	0.2	0.185
Mg	-	-	<0.001	0.00193	0.0023
Mn	-	-	<0.0005	0.000622	0.0011
Mo	-	-	<0.005	<0.005	0.007
NH_3	-	-	0.06	0.05	0.04
Na	-	-	238	248	250
Ni	-	-	0.154	0.208	0.0892
S	-	-	88.9	-	-
SO_4	-	-	227	240	221
SiO_2	-	-	590	582	540
Sr	-	-	0.012	0.0121	0.0107
Ti	-	-	<0.005	0.00553	<0.005
TDS	-	-	1167	1388	1281
Zn	-	-	<0.0005	<0.0005	<0.0005
Gas					

Ar [%]	0.08	-	1.49	0.5	-
CH_4 [%]	0.98	-	5.65	1.5	-
H_2 [%]	95.84	-	19.58	60.95	-
N_2 [%]	3.1	-	73.27	37.05	-
O_2 [%]	<0.01	-	<0.01	<0.01	-
Steam					
CO_2	16400	-	943	1180	-
H_2S	1220	-	164	315	-
Condensate					
Cond. [µS/cm] @ 25 °C	24.6	-	16.3	25.1	-
Al	0.00288	-	0.00732	0.00726	-
As	<0.01	-	<0.01	<0.01	-
B	0.0547	-	<0.005	0.0109	-
Ba	<0.0005	-	<0.0005	0.000544	-
Ca	0.19	-	0.106	0.0943	-
Cl	0.06	-	0.16	0.12	-
Cr	<0.005	-	<0.005	<0.005	-
Cu	<0.005	-	<0.005	<0.005	-
Fe	0.026	-	0.0187	0.0826	-
K	0.371	-	0.293	0.285	-
Li	<0.01	-	<0.01	<0.01	-
Mg	0.00336	-	0.00111	0.00329	-
Mn	0.00093	-	<0.0005	0.00139	-
Mo	<0.005	-	<0.005	<0.005	-
NH_3	0.22	-	0.06	0.05	-
Na	0.76	-	0.956	0.619	-
Ni	<0.0005	-	<0.0005	<0.0005	-
SiO_2	2.94	-	2.74	2.6	-
Sr	0.00113	-	<0.001	<0.001	-
Ti	<0.005	-	<0.005	<0.005	-
Zn	<0.0005	-	<0.0005	<0.0005	-

Table 15b. *Chemical composition of geothermal fluid samples from the Krafla geothermal field. Concentrations are given in mg/L unless otherwise stated.*

Location name	K-41	K-32	K-38	K-40
Date	2020-10-07	2020-10-07	2020-10-07	2020-10-07
Sample id	20200194	20200193	20200192	20200191
Pressure (PS) [bar-g]	21.5	7.4	30.7	11.1
Temperature (TS) [°C]	218.7	174.4	236.6	-
GT ratio @ 25 °C	0.7961	0.0397	0.0884	0.4888
Discharge [kg/s]	6.53	-	9.7	19.14
Enthalpy [kJ/kg]	2774	-	1840	2755
Water				
pH [/ °C]	9.05 / 46.2	9.34 / 18	7.21 / 9	-
Cond. [µS/cm] @ 25 °C	582	1224	698	-
Al	0.719	1.47	1.38	-
As	<0.01	0.013	<0.01	-
B	2.16	0.609	0.545	-
Ba	0.00237	0.0086	0.00191	-
Br	0.05	0.06	0.08	-
CO_2	147	45.8	114	-
Ca	1.29	4.32	2.05	-
Cl	9.82	49.9	49.9	-
Cr	<0.005	<0.005	<0.005	-
Cu	<0.005	<0.005	<0.005	-
F	1.48	1.34	1.24	-
Fe	0.00598	<0.002	<0.002	-
H_2S	32.9	83.6	127	-
K	11.1	41.8	19.5	-
Li	0.0946	0.3	0.125	-
Mg	0.00454	0.00141	0.00289	-
Mn	0.0013	0.000754	0.00249	-
Mo	<0.005	<0.005	<0.005	-
NH_3	0.06	0.06	0.07	-
Na	81.9	280	150	-
Ni	<0.0005	0.189	0.128	-
S	3.96	-	25	-
SO_4	13.3	282	83.2	-
SiO_2	143	554	418	-
Sr	0.00617	0.0152	0.00975	-
Ti	0.00877	0.0177	0.00503	-
TDS	515	1445	934	-
Zn	0.000697	<0.0005	0.000561	-
Gas				

Ar [%]	0.11	1.39	0.39	0.29
CH_4 [%]	0.41	0.37	0.65	0.56
H_2 [%]	92.36	10.22	79.59	84.75
N_2 [%]	7.11	88.02	19.37	14.4
O_2 [%]	<0.01	<0.01	<0.01	<0.01
Steam				
CO_2	9460	70.1	3140	8630
H_2S	789	357	228	1680
Condensate				
Cond. [µS/cm] @ 25 °C	24.7	23.1	24.8	134.4
Al	0.00247	0.00587	0.00803	0.445
As	<0.01	<0.01	<0.01	0.0108
B	0.0621	<0.005	0.0242	1.52
Ba	0.000841	0.000862	0.00168	0.00125
Ca	0.106	0.0507	0.0671	0.279
Cl	0.03	0.04	0.05	1.34
Cr	<0.005	<0.005	<0.005	<0.005
Cu	<0.005	<0.005	<0.005	<0.005
Fe	0.0462	0.0453	0.0897	0.101
K	0.201	0.118	0.211	3.25
Li	<0.01	<0.01	<0.01	0.0196
Mg	0.00459	0.00318	0.00464	0.00964
Mn	0.000915	0.000938	0.00164	0.00356
Mo	<0.005	<0.005	<0.005	0.00759
NH_3	0.04	0.05	0.05	0.07
Na	0.386	0.281	0.33	18.1
Ni	<0.0005	<0.0005	<0.0005	<0.0005
SiO_2	0.488	0.611	0.505	133
Sr	<0.001	<0.001	<0.001	<0.001
Ti	<0.005	<0.005	<0.005	<0.005
Zn	<0.0005	<0.0005	0.00116	0.00994

Table 16a. *Chemical composition of geothermal fluid samples from the Theistareykir geothermal field. Concentrations are given in mg/L unless otherwise stated.*

Location name	ÞG-15	ÞG-09	ÞG-03	Injection Well ÞN-01	Injection Well ÞG-14
Date	2020-10-06	2020-10-06	2020-10-06	2020-10-06	2020-10-06
Sample id	20200190	20200189	20200188	20200187	20200186
Pressure (PS) [bar-g]	10.8	1.1	6.5	-	-
Temperature (TS) [°C]	187	-	-	102.9	160
GT ratio @ 25 °C	0.0302	2.3213	2.9145	-	-
Discharge [kg/s]	25	13	13	-	12.2
Enthalpy [kJ/kg]	950	2660	2577	-	-
Water					
pH [/ °C]	9.33 / 15.3	-	-	8.54 / 25.8	7.75 / 15
Cond. [µS/cm] @ 25 °C	623	-	-	333	603
Al	1.45	-	-	0.995	1.88
As	<0.01	-	-	<0.01	<0.01
B	0.749	-	-	0.602	1.1
Ba	0.00152	-	-	<0.0005	0.000587
Br	0.16	-	-	0.09	0.17
CO_2	50.2	-	-	27.2	76.2
Ca	0.622	-	-	0.142	0.237
Cl	58.8	-	-	33.1	63.1
Cr	<0.005	-	-	<0.005	<0.005
Cu	<0.005	-	-	<0.005	<0.005
F	1.24	-	-	0.63	1.24
Fe	0.00412	-	-	0.00331	0.00388
H_2S	51.9	-	-	38.0	72.7
K	18.5	-	-	12.6	21.8
Li	0.1	-	-	0.0693	0.118
Mg	0.00204	-	-	0.00133	0.00289
Mn	0.000595	-	-	<0.0005	0.00137
Mo	<0.005	-	-	<0.005	<0.005
NH_3	0.05	-	-	0.04	0.05
Na	138	-	-	64.7	112
Ni	0.137	-	-	0.0528	0.11
SO_4	26.3	-	-	10.4	18.8
SiO_2	426	-	-	352	657
Sr	0.00147	-	-	<0.001	<0.001
Ti	0.0173	-	-	<0.005	<0.005
TDS	826	-	-	549	1092
Zn	0.000695	-	-	<0.0005	0.00102
Gas					

Ar [%]	1.13	0.02	0.04	-	-
CH_4 [%]	0.22	0.03	0.12	-	-
H_2 [%]	25.08	98.67	97.89	-	-
N_2 [%]	73.58	1.29	1.95	-	-
O_2 [%]	<0.01	<0.01	<0.01	-	-
Steam					
CO_2	643	850	6890	-	-
H_2S	211	3360	2620	-	-
Condensate					
pH [/ °C]	-	-	4.2 / 17.1	-	-
Cond. [µS/cm] @ 25 °C	9.7	61.2	37.7	-	-
Al	0.00319	0.012	0.0116	-	-
As	<0.01	<0.01	<0.01	-	-
B	0.00946	<0.005	<0.005	-	-
Ba	0.00105	0.00101	0.00106	-	-
Ca	0.0251	0.0643	0.0447	-	-
Cl	0.03	0.02	0.04	-	-
Cr	<0.005	<0.005	<0.005	-	-
Cu	<0.005	<0.005	<0.005	-	-
Fe	0.0506	0.0559	0.199	-	-
K	0.0772	0.125	0.272	-	-
Li	<0.01	<0.01	<0.01	-	-
Mg	0.00115	0.00401	0.00459	-	-
Mn	0.000866	0.00176	0.00115	-	-
Mo	<0.005	<0.005	<0.005	-	-
NH_3	0.06	0.12	0.03	-	-
Na	0.0914	0.142	0.56	-	-
Ni	<0.0005	<0.0005	<0.0005	-	-
SiO_2	0.521	1.82	5.31	-	-
Sr	<0.001	<0.001	<0.001	-	-
Ti	<0.005	<0.005	<0.005	-	-
Zn	<0.0005	0.000842	0.00143	-	-

Table 16b. *Chemical composition of geothermal fluid samples from the Theistareykir geothermal field. Concentrations are given in mg/L unless otherwise stated.*

Location name	ÞG-04	ÞG-17	ÞG-01	ÞG-05B
Date	2020-10-05	2020-10-05	2020-10-05	2020-10-05
Sample id	20200185	20200184	20200183	20200182
Pressure (PS) [bar-g]	8.5	8.2	8.6	8.6
Temperature (TS) [°C]	178	176.5	178.4	178.1
GT ratio @ 25 °C	0.6318	0.216	0.1801	0.0882
Discharge [kg/s]	35.28	32.32	22.26	62.12
Enthalpy [kJ/kg]	2708	2294	1653	1181
Water				
pH [/ °C]	8.37 / 28.6	8.44 / 21.1	8.81 / 18.5	9.37 / 12.2
Cond. [µS/cm] @ 25 °C	324	500.5	567	643
Al	2.27	2.38	1.82	1.88
As	0.0616	<0.01	<0.01	<0.01
B	9.02	1.77	1.1	0.688
Ba	0.000563	0.000835	<0.0005	<0.0005
Br	0.1	0.22	0.23	0.16
CO_2	16.7	28.4	26.4	47.4
Ca	0.305	0.153	0.286	0.442
Cl	32.9	79.1	86.2	58.3
Cr	<0.005	<0.005	<0.005	<0.005
Cu	<0.005	<0.005	<0.005	<0.005
F	1.93	1.03	0.89	1.42
Fe	0.0097	0.00683	0.00331	0.00645
H_2S	39.1	32.2	27.7	36.7
K	12.5	22.4	21.7	24.2
Li	0.125	0.186	0.117	0.135
Mg	0.00622	<0.01	0.00433	0.00802
Mn	<0.0005	<0.0005	<0.0005	<0.0005
Mo	0.0115	<0.005	<0.005	<0.005
NH_3	0.03	0.05	0.06	0.06
Na	69	95.7	117	138
Ni	<0.0005	0.116	0.303	<0.0005
S	1.12	0.949	4.5	10.6
SO_4	6.3	2.51	13.1	32.4
SiO_2	664	913	729	643
Sr	0.00142	<0.001	<0.001	0.00137
Ti	0.00996	0.0109	0.00942	<0.005
TDS	907	1342	1109	1033
Zn	0.00349	0.000974	0.00231	0.00426
Gas				

Ar [%]	0.1	0.24	0.32	1.45
CH_4 [%]	0.09	0.38	0.14	0.92
H_2 [%]	94.53	84.37	80.17	19.36
N_2 [%]	5.28	15.02	19.37	78.26
O_2 [%]	<0.01	<0.01	<0.01	<0.01
Steam				
CO_2	348	1880	735	1300
H_2S	821	580	275	193
Condensate				
Cond. [µS/cm] @ 25 °C	83	61.8	61.8	59.8
Al	0.00218	0.00249	0.00739	0.00519
As	<0.01	<0.01	<0.01	<0.01
B	0.112	0.0258	0.0181	0.0155
Ba	<0.0005	0.000793	0.00166	0.00118
Ca	0.0288	0.0605	0.0562	0.0861
Cl	0.1	0.16	0.09	0.08
Cr	0.00503	0.0144	0.0326	0.143
Cu	<0.005	<0.005	<0.005	<0.005
Fe	0.261	0.636	1.76	2.91
K	0.168	0.235	0.191	0.201
Li	<0.01	<0.01	<0.01	<0.01
Mg	0.00126	0.00313	0.00173	0.0028
Mn	0.000998	0.00215	0.00334	0.0049
Mo	<0.005	<0.005	<0.005	0.00628
NH_3	0.02	0.03	0.03	0.04
Na	0.341	0.487	0.358	0.259
Ni	0.000654	0.000832	0.0019	0.0181
SiO_2	1.7	1.99	1.81	2.26
Sr	<0.001	<0.001	<0.001	<0.001
Ti	<0.005	<0.005	<0.005	<0.005
Zn	0.00106	0.0025	0.00214	0.00612

Table 17. *Stable water isotope ($\delta_{18}O-H_2O$ and δ_2H-H_2O) results from four geothermal production wells from the Theistareykir geothermal field.*

Sample	**Location**	**Liquid phase**				**Vapor phase**		
		pH / C	$\delta_{18}O-H_2O$	δ_2H-H_2O	δ_2H-Excess	$\delta_{18}O-H_2O$	δ_2H-H_2O	δ_2H-Excess
			$‰_{VSMOW}$	$‰_{VSMOW}$	‰	$‰_{VSMOW}$	$‰_{VSMOW}$	‰
20200182	ÞG-05B	9.37 / 12.2	-10.31	-100	-17.52	-13.02	-105.2	-1.04
20200183	ÞG-01	8.81 / 18.5	-9.73	-100.9	-23.06	-11.8	-104.7	-10.3
20200188	ÞG-03					-16.25	-115.7	14.3
20200190	ÞG-15	9.33 / 15.3	-9.34	-99.5	-24.78	-12.08	-104.6	-7.96

Table 18: *Carbon (δ13C-DIC) isotope results from four geothermal production wells from the Theistareykir geothermal field.*

Sample	**Location**	**Liquid phase**			**Vapor phase**	
		pH / °C	CO_2	$\delta_{13}C$-DIC	CO_2	$\delta_{13}C$-DIC
			ppm	$‰_{VPDB}$	ppm	$‰_{VPDB}$
20200182	ÞG-05B	9.37 / 12.2	47.4	-17.2	1300	-14.0
20200183	ÞG-01	8.81 / 18.5	26.4	-18.9	735	-12.4
20200188	ÞG-03				6890	-7.3
20200190	ÞG-15	9.33 / 15.3	50.2	-15.7	643	-9.8

Table 19. *Sulphur ($\delta_{34}S-H_2S$ and $\delta_{34}S-SO_4$) isotope results from four geothermal production wells from the Theistareykir geothermal field.*

Sample	**Location**	**Liquid phase**					**Vapor phase**	
		pH / °C	H_2S	SO_4	$\delta_{34}S-H_2S$	$\delta_{34}S-SO_4$	H_2S	$\delta_{34}S-H_2S$
			ppm	ppm	$‰_{VCDT}$	$‰_{VCDT}$	ppm	$‰_{VCDT}$
20200182	ÞG-05B	9.37 / 12.2	36.7	32.4	1.9	3.2	193	4.0
20200183	ÞG-01	8.81 / 18.5	27.7	13.1	1.6	1.6	275	3.9
20200188	ÞG-03	-	-	-	-	-	2620	-1.0
20200190	ÞG-15	9.33 / 15.3	51.9	26.3	0.8	4.5	211	LOD

Table 20. *Deep fluid composition of two-phase production well samples from the Krafla geothermal field. Concentrations are given in mg/L unless otherwise stated.*

Location name	K-32	K-13A	K-06
Date	2020-10-07	2020-10-08	2020-10-08
Sample id	20200193	20200197	20200198
Ref. Temp [°C]	244	250.6	245
pH	7.68	7.40	7.38
Al	1.24	1.22	0.999
B	0.512	0.800	0.359
CO_2	49.7	259	263
Ca	3.64	2.22	1.52
Cl	41.9	44.2	24.5
F	1.13	1.37	1.02
Fe	0.009	0.016	0.006
H_2S	127	106	63.4
K	35.1	28.3	23.2
Mg	0.00169	0.00217	0.00102
NH_3	0.0584	0.0500	0.0600
Na	235	205	184
SO_4	237	198	175
SiO_2	465	482	457
TDS	1213	1148	902
CH_4	0.02	0.28	0.85
H_2	0.05	1.45	0.37
N_2	6.41	12.3	19.2

Table 21. *Deep fluid composition of two-phase production well samples from the Theistareykir geothermal field. Concentrations are given in mg/L unless otherwise stated.*

Location name	ÞG-05B	ÞG-01	ÞG-17	ÞG-04	ÞG-15
Date	2020-10-05	2020-10-05	2020-10-05	2020-10-05	2020-10-06
Sample id	20200182	20200183	20200184	20200185	20200190
Ref. Temp [°C]	260.2	270 [a]	280 [a]	290 [a]	227.6
pH	7.34	7.41	7.15	7.15	7.56
Al	1.53	1.42	1.74	1.25	1.32
B	0.561	0.860	1.29	4.96	0.681
CO_2	284	88.6	203	40.3	105
Ca	0.375	0.22	0.11	0.17	0.567
Cl	47.3	67.4	57.8	18.1	53.4
F	1.15	0.696	0.752	1.06	1.13
Fe	0.554	0.0026	0.005	0.0053	0.008
H_2S	66.2	55.1	91.1	127	66.6
K	19.7	17.0	16.4	6.88	16.8
Mg	0.007	0.004	0	0.004	0.0020
NH_3	0.0562	0.02	0.01	0	0.0509
Na	112	91.5	69.9	38.0	125
SO_4	26.3	10.2	1.83	3.47	23.9
SiO_2	522	570	667	365	387
TDS	838	867	980	499	750
CH_4	0.1	0.02	0.05	0.04	0
H_2	0.27	1.22	1.46	5.2	0.06
N_2	15.2	4.08	3.58	4	2.36

[a] *Production wells with measured discharge enthalpy >1500 kJ/kg, composition calculated according to "excess enthalpy" method.*

4.5 REFERENCES

Ármannsson, H., Gíslason, G., and Torfason, H. (1986) Surface exploration of the Theistareykir high-temperature geothermal area, Iceland, with special reference to the application of geochemical methods. *Applied Geochemistry* 1, 47-64.

Ármannsson, H., Gudmundsson, Á., and Steingrímsson, B.S. (1987) Exploration and development of the Krafla geothermal area. *Jökull* 37, 13-30.

Árnason, K., Eyjólfsson, B., Gunnarsson, K., Sæmundsson, K., and Björnsson, A. (1984) Krafla-Hvíthólar. Geology and geophysical studies 1983. National Energy Authority Report OS-84033/JHD-04, 61 pp (in Icelandic).

Arnórsson, S., Bjarnason, J.Ö., Giroud, N., Gunnarsson, I., and Stefánsson, A. (2006) Sampling and analysis of geothermal fluids. *Geofluids* 6, 203-216.

Arnórsson, S., Stefánsson, A., and Bjarnason, J.Ó. (2007) Fluid-fluid interactions in geothermal systems. *Reviews in Mineralogy and Geochemistry* 65, 259-312.

Bjarnason, J.Ö. (2010) The Speciation Program WATCH, Version 2.4. National Energy Authority Report. 9 pp.

Björnsson, A., Johnsen, G., Sigurdsson, S., Thorbergsson, G, and Tryggvason, E. (1979) Rifting of the plate boundary in North Iceland 1975-1978. *Journal of Geophysical Research* 84, 3029-3038.

Darling, G. and Ármannsson, H. (1989) Stable isotope aspects of fluid flow in the Krafla, Námafjall and Theistareykir geothermal systems of northeast Iceland. *Chemical Geology* 76, 197-213.

Friðriksson, Þ. and Giroud, N. (2008) Jarðefnafræðilegt vinnslueftirlit á Reykjanesi 2006 og 2007. Iceland GeoSurvey, ÍSOR-2008/021.

Gudmundsson, J.S. (1983) Geothermal electric power in Iceland: development in perspective. *Energy* 8, 491-513.

Gudmundsson, B.Th. and Arnórsson, S. (2002) Geochemical monitoring of the Krafla and Námafjall geothermal areas, N-Iceland. *Geothermics* 31, 195-243.

Lund, J.W. and Boyd, T.L. (2016) Direct utilization of geothermal energy 2015 worldwide review. *Geothermics* 60, 66-93.

Óskarsson, F., Ármannsson, H., Ólafsson, M., Sveinbjörnsdóttir, A., and Markússon, S.H. (2013) The Theistareykir geothermal field, NE Iceland: fluid chemistry and production properties. *Procedia Earth and Planetary Science* 7, 644 - 647.

Preuss, K. (2002) Mathematical modelling of fluid flow and heat transfer in geothermal systems. United Nations University Geothermal Training Programme, Reykjavik, Iceland.

Report to the Earth Science Division, Lawrence Berkeley National Laboratory, University of California.

Ragnarsson, Á., Steingrímsson, B., and Thorhallsson, S. (2020) Geothermal development in Iceland, 2015-2019. Proceedings World Geothermal Congress 2020 (paper 01063).

Saby, M., Piniti, D.L., van Hinsberg, V., Gautason, B., Sigurðardóttir, Á., Castro, C., Hall, C., Óskarsson, F., Rocher, O., Hélie, J., and Méjean, P. (2020) Sources and transport of fluid and heat at the newly-developed Theistareykir Geothermal Field, Iceland. *Journal of Volcanology and Geothermal Research* 405, 107062.

Sæmundsson, K. (1974) Evolution of the axial rifting zone in northern Iceland the Tjörnes fracture zone. *Geological Society of America Bulletin* 85, 495-504.

Sæmundsson, K. (1978) Fissure swarms and central volcanoes of the neovolcanic zones of *Iceland. Geol. Journal*, special issue, 415-432.

Sæmundsson, K. (1983) Fractures in the Krafla area. On the status of the Krafla geothermal power station. Proceedings of meeting held in Akureyri, Iceland 2-3 March 1983, pp. 4-8 (in Icelandic).

Sæmundsson, K. (2007) The geology of Theistareykir (in Iceland). Reykjavik; Iceland GeoSurvey report 2007; ÍSOR-07270.

Stefánsson, V. (1981) The Krafla geothermal field, Northeast Iceland. In: Rybach, L., Muffler, L.J.P. (Eds.), Geothermal Systems and Case Histories. John Wiley, New York, pp. 273-294.

Stefánsson, A., Gunnarsson, I., and Giroud, N. (2007) New methods for the direction determination of dissolved inorganic, organic and total carbon in natural waters by reagent-free (TM) ion chromatography and inductively coupled plasma atomic emission spectrometry. *Analytica Chimica Acta* 582, 69-74.

Sveinbjörnsdóttir, A.E., Ármannsson, H., Ólafsson, M., Óskarsson, F., Markússon, S.H., & Magnúsdóttir, S. (2013) the Theistareykir geothermal field, NE Iceland. Isotopic characteristics and origin of circulating fluids. *Procedia Earth and Planetary Science* 7, 822 - 825.

Thórarinsson, F. (1980) Krafla. Quadripole-quadripole resistivity survey carried out in 1979. National Energy Authority Report OS80013/JHD-07, 52 pp (in Icelandic with an English summary).

5 APPENDICES

5.1 **APPENDIX I**: SILICA GEOTHERMOMETER EQUATIONS

No	**Geothermometer**	**Geothermometer Equations**	**Temperature**	**Reference**
1	Quartz	$t°C=-42.2+0.28832S-3.6686\times10^{-4}S^2+3.1665\times10^{-7}S^3+77.034\log S$	25-900	Fournier and Potter, 1982
2	Quartz (no steam loss)	$t°C=(1309/(5.19-\log S))-273.15$	25-250	Fournier, 1977
3	Quartz (at 100°C max steam loss)	$t°C=(1522/(5.75-\log S))-273.15$	25-250	Fournier, 1977
4	Quartz	$t°C=-55.3+0.36559S-5.3954\times10^{-4}S^2+5.5132\times10^{-7}S^3+74.360\log S$	0-350	Arnórsson, 2000
5	Chalcedony (no steam loss)	$t°C=(1032/(4.69-\log S))-273.15$	0-250	Fournier, 1977
6	Chalcedony (no steam loss)	$t°C=(1112/(4.91-\log S))-273.15$	25-180	Arnórsson et al., 1983
7	α- cristobalite	$t°C=(1000/(4.78-\log S))-273.15$		Fournier, 1977
8	β- cristobalite	$t°C=(781/(4.51-\log S))-273.15$	25-250	Fournier, 1977
9	Amorph silica	$t°C=(731/(4.52-\log S))-273.15$	25-250	Fournier, 1977
10	Amorph silica	$t°C=-121.6+0.2694S-1.8101\times10^{-4}S^2+7.5221\times10^{-8}S^3+55.114\log S$	0-350	Arnórsson, 2000

5.2 APPENDIX II: CATION GEOTHERMOMETER EQUATIONS

No	Geothermometer	Geothermometer Equations (t= °C)	Temperature (°C)	Reference
1	Na-K	$t^\circ C = (856/(0.857+\log(Na/K)))-273.15$	100-275	Truesdell, 1976
2	Na-K	$t^\circ C = (833/(0.780+\log(Na/K)))-273.15$		Tonani, 1980
3	Na-K	$t^\circ C = (933/(0.993+\log(Na/K)))-273.15$	25 -250	Arnorsson et al., 1983
4	Na-K	$t^\circ C = (1319/(1.699+\log(Na/K)))-273.15$	250-350	Arnorsson et al., 1983
5	Na-K	$t^\circ C = (1217/(1.483+\log(Na/K)))-273.15$		Fournier, 1979
6	Na-K	$t^\circ C = (1178/(1.470+\log(Na/K)))-273.15$		Nieva and Nieva, 1987
7	Na-K	$t^\circ C = (1390/(1.750+\log(Na/K)))-273.15$		Giggenbach, 1988
8	Na-K	$t^\circ C = 733.6-770.551Y+378.189Y^2 -95.753Y^3 + 9.544Y^4$	0-350	Arnórsson, 2000
9	K-Mg[b]	$t^\circ C = (2330/(7.35-\log(K^2/Mg)))-273.15$		Fournier, 1992
10	K-Mg[c]	$t^\circ C = (1077/(4.033+\log(K^2/Mg)))-273.15$		Fournier, 1992
11	K-Mg	$t^\circ C = (4410/(14-\log(K^2/Mg)))-273.15$		Giggenbach, 1988
12	Li-Mg	$t^\circ C = (2200/(5.47-\log(Li/Mg^{0.5})))-273.15$		Kharaka and Mariner, 1989
13	Na-K-Ca[d]	$t^\circ C = (1647/(\log(Na/K)+\beta[\log(\sqrt{Ca}/Na)+2.06]+2.47))-273.15$		Fournier and Truesdell, 1973
14	K-Ca	$t^\circ C = (1930/(3.861-\log(K/\sqrt{Ca})))-273.15$		Tonani, 1980
15	Na-Li	$t^\circ C = (1590/(0.779+\log(Na/Li)))-273.15$		Kharaka et al., 1982